LBNL-42750
Preprint

ERNEST ORLANDO LAWRENCE
BERKELEY NATIONAL LABORATORY

The Growth of Iron Oxide Films on Pt(111): A Combined XPD, STM, and LEED Study

Y.J. Kim, C. Westphal, R.X. Ynzunza,
Z. Wang, H.C. Galloway, M. Salmeron,
M.A. Van Hove, and C.S. Fadley

Materials Sciences Division

June 1998

Submitted to
Surface Science

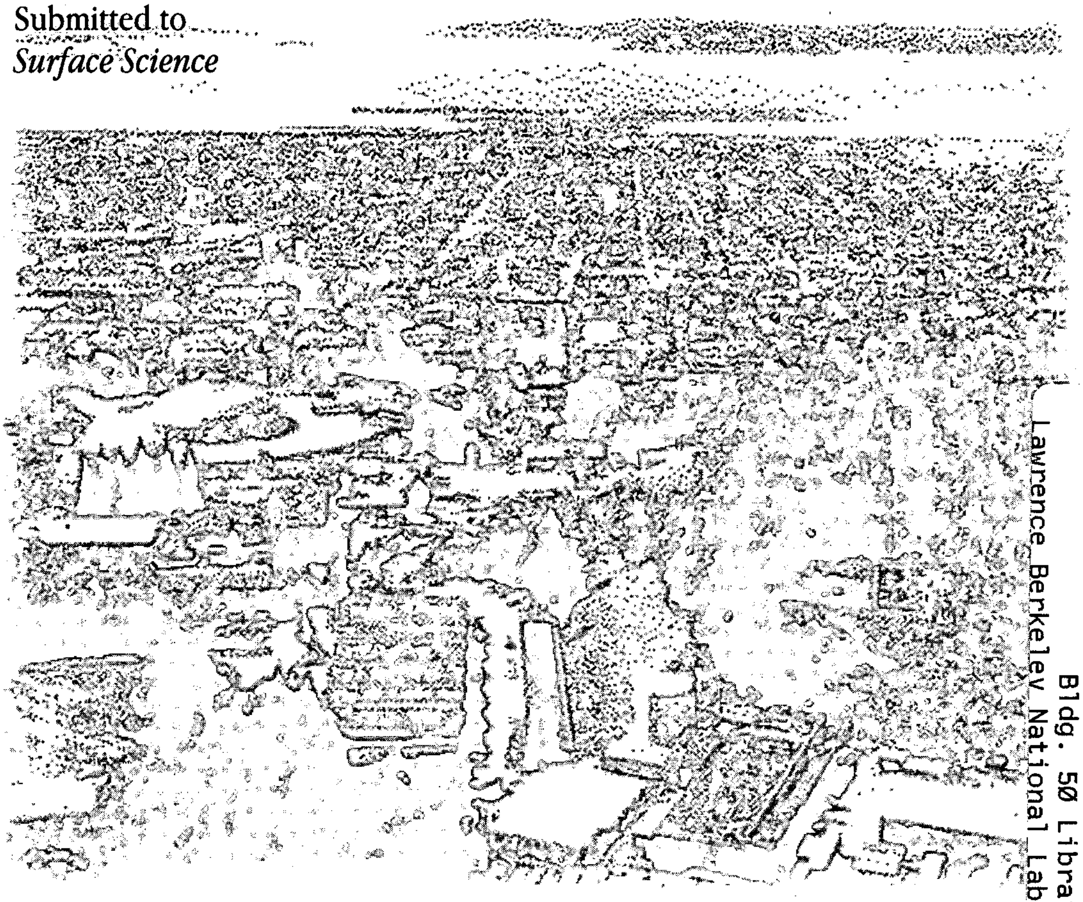

LBNL-42750

The Growth of Iron Oxide Films on Pt(111): A Combined XPD, STM, and LEED Study

Y.J. Kim, C. Westphal, R.X. Ynzunza, Z. Wang, H.C. Galloway,
M. Salmeron, M.A. Van Hove, and C.S. Fadley

Materials Sciences Division
Ernest Orlando Lawrence Berkeley National Laboratory
University of California
Berkeley, California 94720

June 1998

This work was supported by the Director, Office of Energy Research, Office of Basic Energy Sciences, Materials Sciences Division, of the U.S. Department of Energy under Contract No. DE-AC03-76SF00098, and the Office of Naval Research under Contract No. N00014-94-0162.

LBNL-42750

To appear in Surface Science

The Growth of Iron Oxide Films on Pt(111):
A Combined XPD, STM, and LEED Study

Y.J. Kim[a,b,*], C.Westphal[a,c,†], R.X.Ynzunza[a,d], Z.Wang[a,d,‡],
H.C.Galloway[a,e,#], M. Salmeron[a], M.A. Van Hove[a], and C.S. Fadley[a,d]

[a]Materials Sciences Division, Lawrence Berkeley National Laboratory,
Berkeley, CA 94720
[b]Dept. of Chemistry, University of Hawaii, Honolulu, HI 96822
[c]Dept. of Physics, University-GHS-Essen, Essen, Germany
[d]Dept. of Physics, Univ. of California-Davis, Davis, CA 95616
[e]Dept. of Physics, University of California-Berkeley, Berkeley, CA 94720
[*]Present address: EMSL, Pacific Northwest National Laboratory, Richland, WA 99352
[†]Present address: Institute of Physics, University of Muenster, Muenster, Germany
[‡]Present address: Prolinx Incorporated, San Jose, CA 95119
[#]Present address: Dept. of Physics, Southwest Texas State University, San Marcos, TX 78666

ABSTRACT

The three complementary surface structure probes of x-ray photoelectron diffraction (XPD), scanning tunneling microscopy (STM), and low-energy electron diffraction (LEED) have been combined in a single instrument. This experimental system has been utilized to study the growth of iron oxide films on Pt(111) over the thickness range from 0.75 to 3.00 monolayers (ML). Each film was formed by first depositing an overlayer of pure Fe with a certain coverage in ML (ranging from 0.75 ML to 3.00 ML) and then thermally oxidizing the Fe at a temperature of 980K and in an oxygen pressure of $4x10^{-6}$ Torr. For films up to ~1 ML in thickness, a bilayer of Fe and O similar to those in bulk FeO parallel to a (111) plane is found to form. In agreement with a prior STM and LEED study by Galloway et al., we find this bilayer to be an incommensurate oxide film forming a lateral superlattice or Moiré structure with short- and long-range periodicities of ~3.1 Å and ~26.0 Å. The XPD data in addition permits concluding that the topmost oxygen layer is highly relaxed inward by ~0.6 Å as compared to the bulk FeO (111) interplanar spacing, and that the stacking of the topmost O atoms with respect to the underlying Pt is dominated by one of two structurally very similar possibilities. It is furthermore necessary to consider interactions over at least four atomic layers (O, Fe, and the first two Pt layers) to explain this dominance of one stacking type. For thicker iron oxide films from 1.25 ML to 3.0 ML, the growth mode is essentially Stranski-Krastanov: iron oxide islands form on top of the FeO(111) bilayer mentioned above. For iron oxide films of 3.0 ML thickness, x-ray photoelectron spectroscopy (XPS) yields an Fe $2p_{3/2}$ binding energy and an Fe:O stoichiometry consistent with the presence of Fe_3O_4. XPD data further prove this overlayer to be $Fe_3O_4(111)$-magnetite in two almost equally populated domains with a 180° rotation between them. The structural parameters for this Fe_3O_4 overlayer generally agree with those of a previous LEED study, except that we do not find a terminating partial monolayer of Fe and arrive at a significant difference in the first Fe-O interplanar spacing. Overall, this work demonstrates the considerable benefits to be derived by using this particular set of complementary surface structure probes in such epitaxial growth studies.

1. INTRODUCTION

It is by now clear that no single surface structure probe directly and unambiguously provides all of the desired information for a given problem, and that it is highly advantageous to use complementary information from several methods [1]. In this paper, three such complementary surface structure probes, x-ray photoelectron diffraction (XPD) [2], scanning tunneling microscopy (STM) [3], and low-energy electron diffraction (LEED) [4] have for the first time been combined in a single ultrahigh vacuum (UHV) system [5b]. XPD is a near-surface probe of the short- range order in the first 3-5 shells of neighbors around each emitter [2]. STM probes both short- and long- range order, as well as disorder, in the top-most surface layer(s), and is primarily sensitive to the outermost surface topography via the surface density of electronic states [3]. In the simplest and most often used form of LEED that will be used in this study, diffraction patterns at a few energies are interpreted in a kinematical way, without measuring current versus voltage (I-V) curves. Thus for our purposes, LEED is primarily sensitive to long-range two-dimensional order, with a probing depth that is comparable to or somewhat shorter than that of XPD [4]. XPD has a special advantage of being element-specific, as each core level studied is characteristic of a given atomic number, while STM and LEED are not. Thus, XPD patterns can be obtained for each of the atoms present near the surface of the sample. In this paper, these three techniques have been utilized to study the growth of iron oxide films on Pt(111) for Fe coverages of 0.75 monolayer (ML) to 1.75 ML (in steps of 0.25 ML), as well as of 3.0 ML. A preliminary account of this work for coverages up to 1.0 ML has appeared elsewhere [5a], and more extensive experimental and theoretical details are also available [5b].

The surface structure of metal oxides has not been studied as extensively as that of metal and semiconductor single crystals, but it is of high interest in a number of technological and environmental applications [6]. Some reasons for this lack of data are that the surfaces of metal-oxide single crystals are often difficult to prepare without alterations from the bulk stoichiometry and their insulating properties often make surface characterization difficult using techniques such as the various electron-based techniques or STM. However, in some cases, including the iron-oxide/Pt system [7-15], the oxide overlayer has been found to grow in an ordered and stoichiometric manner on a metal substrate. Provided that the oxide is not too thick and the overall surface conductivity is thus not too low, these systems thus permit studying epitaxial growth using the full array of surface structure probes. The novel interface created between the metal substrate and the oxide overlayer is also a very important aspect of these systems, with applications to oxide-supported metal catalysts where strong metal support interactions are found [16-19], as well as to metal-ceramic bonding for corrosion resistance in high-temperature materials [20]. Finally, the different oxides of iron are important in high-density magnetic recording media [21], and the transition-metal oxides are key ingredients in the high-T_C materials and other highly correlated systems, which are often grown as thin films [22].

The iron oxides vary in stoichiometry from FeO = $Fe_{1.0}O_{1.0}$ to Fe_3O_4 = $Fe_{1.0}O_{1.33}$ to Fe_2O_3 = $Fe_{1.0}O_{1.5}$. Bulk FeO (wustite) forms in the NaCl structure with Fe^{2+} cations octahedrally coordinated to oxygen anions. However, it is always found to be deficient in iron due to defect formation which is in turn believed to be related to the easy oxidation of Fe^{2+} ions; thus, the actual bulk stoichiometry is closer to $Fe_{1.0}O_{1.05}$ [23]. In addition, FeO is not in fact an equilibrium phase at room temperature in the Fe-O bulk phase diagram [23,24]. The stable room-temperature phase of Fe_2O_3 is α-Fe_2O_3, which forms in the corundum structure with Fe^{3+} cations located in distorted oxygen octahedra of a rhombohedral lattice [23]. While FeO and Fe_2O_3 are anti-ferromagnetic, bulk Fe_3O_4, or magnetite, is ferrimagnetic and has the cubic inverse spinel structure. In magnetite, the oxygen anions approximately form an fcc lattice and the iron cations occupy tetrahedrally-coordinated interstices (A-sites) and octahedrally-coordinated interstices (B-sites) within this fcc lattice. The valence structure is $[Fe^{3+}]_{tet}[Fe^{3+}Fe^{2+}]_{oct}(O^{2-})_4$, where half of the Fe^{3+} ions are located on A-sites and the other half together with the Fe^{2+} ions are on B-sites. The electron spins of the A- and B-sublattices couple anti-ferromagnetically, leading to a net magnetization because of the different total magnetic moments of the two sublattices. A rapid exchange of valence electrons between localized states of octahedrally-coordinated Fe^{2+} and Fe^{3+} cations is believed to be responsible for the relatively high bulk electrical conductivity in the metallic state at room temperature [25a], and Fe_3O_4 has a well-defined Verwey transition from the semiconducting to the metallic state at 122 K [25b].

In spite of the very different crystal structures of the three iron oxides, they all can be viewed to a very good approximation as a stacking of hexagonal-close-packed oxygen layers, with Fe occupying interstitial sites along [111] directions for both FeO and Fe_3O_4, and interstitial sites along [0001] directions for α-Fe_2O_3. The oxygen stacking is thus cubic ABCABC in the cases of FeO and Fe_3O_4, and hexagonal ABAB in the case of α-Fe_2O_3. The atomic geometries of these three oxides are shown in Fig. 1, in which a close-packed oxygen layer (open circles) and the iron cations on either side of it (shaded circles) are indicated. The exposed surfaces are here the simplest terminations of (111) type for both FeO and Fe_3O_4 and of (0001) type for α-Fe_2O_3, with terminations through other planes and with additional surface atoms also being possible, as discussed below. The average bulk O-O distance is only slightly different for the three crystals: 3.04 Å for FeO, 2.97 Å for Fe_3O_4, and 2.90 Å for α-

Fe_2O_3. The bulk Fe-O distances are 2.15 Å in FeO, 1.88 Å for A-sites and 2.07 Å for B-sites in Fe_3O_4, and 1.68 - 1.99 Å for α-Fe_2O_3. For the unreconstructed surfaces shown in Fig. 1, three different two-dimensional unit cells as measured against the oxygen layer are found: (1x1) for FeO, (2x2) for Fe_3O_4, and $(\sqrt{3}x\sqrt{3})R30°$ for α-Fe_2O_3; these are indicated in Fig. 1. Even though these three different unit cells would give rise to different LEED patterns if the surfaces were terminated in the ways shown in the figure, they all have overall threefold symmetry, like the underlying Pt(111) surface. For reference, the Pt-Pt distance in the (111) substrate surface is 2.77 Å, or about 10%, 7%, and 5% smaller than the O-O distances in the three oxides, respectively. Thus, strain is expected in oxide growth with the orientations of Fig. 1, but diminishing from FeO to Fe_3O_4 to α-Fe_2O_3.

Several prior studies of bulk iron oxides have shown that they can be converted from one to another by heating in different partial pressures of oxygen, especially in the near-surface layers [15,26,27]. Studies on bulk single crystals of α-Fe_2O_3(0001) indicate that this surface forms different structures depending on the annealing temperature [28-30], and in fact may consist of coexistent Fe_2O_3(0001) and FeO(111) phases [30]. In addition, prolonged annealing of α-Fe_2O_3(0001) produces a surface structure thought to be Fe_3O_4(111) [14,31a], and a recent STM investigation of Fe_3O_4(111) with ion bombardment and annealing in O_2 reports two coexistent types of surface termination of more complex type than those shown in Fig. 1 [31b]. Studies of bulk Fe_3O_4(001) do not report surface phases of different stoichiometry, but still show three different surface reconstructions [32]. Thus, the thin layers of epitaxial oxides under consideration here might be expected to show facile interconversion of structure type.

In characterizing such epitaxial oxide growth, the three classic growth modes can be considered as a starting point: Frank-van der Merwe (FvM) = smooth layer-by-layer, Stranski-Krastanov (SK) = smooth first layer followed by three-dimensional clusters or islands, and Vollmer-Weber (VW) = only three-dimensional clusters or islands [33]. By now, these categories have often been shown to be oversimplified descriptions of the actual growth modes when compared to the varieties of structures that are actually seen (e.g., in STM). Although there are a wide variety of techniques that can give information about the surface structure of epitaxial films, STM and XPD are particularly well suited because of the complementary local real space information that they provide: STM yields the growth topography and island size, while XPD yields the internal atomic structure (i.e., the relative atomic positions) of the overlayer, as measured locally around each atomic type.

We begin the present study by considering the growth of up to one monolayer of iron oxide on Pt(111). This system has been studied previously with a combination of LEED and ion scattering spectroscopy (ISS) [9,10], STM [11], and near-edge x-ray absorption fine structure (NEXAFS) [15]. Simultaneously applying LEED and ISS to this monolayer growth led to the proposal of a (111)-type FeO bilayer forming a (10x10) coincidence lattice or lateral superlattice on the Pt(111) substrate. However, these results did not permit concluding whether Fe or O atoms, or both, occupied surface positions, since the ISS data showed both Fe and O peaks. A subsequent STM study by Galloway et al. [11] concluded that an incommensurate overlayer lattice forms for which a short overlayer periodicity of 3.1 Å is modulated by a large periodicity of ~26 Å, producing a Moiré-pattern superlattice that is in fact closer to (9x9) than (10x10). This was again suggested to involve an Fe-O bilayer similar to those in bulk FeO with (111) orientation. In addition, a rotational mismatch between the bilayer and the substrate of about ±0.6°, resulting in a ±5.2° rotational mismatch of the larger Moiré periodicity, was proposed based on the existence of two equivalent domains of the large periodicity in adjacent terraces. This rotational mismatch is illustrated in the proposed structural model by Galloway et al. shown in Fig. 2. In this model, two equivalent domains can be obtained by plus and minus rotations by 0.6° of the Fe-O bilayer from the $[1\bar{1}0]$ direction of Pt(111), leading to plus and minus rotations by 5.2° of the large periodicity of the overlayer. But no definite conclusion was possible from this STM work concerning which of the two species is on the surface. A more recent study of this system by NEXAFS [15] concluded that the first monolayer of oxide forms an Fe-O bilayer that is very nearly the same in structure as bulk FeO(111), with an Fe-O interlayer spacing of 1.25 Å that is essentially identical to that in the bulk. But these prior studies left several open questions concerning this interesting monolayer of FeO, such as the detailed atomic geometry within the iron oxide (whether Fe or O occupies surface positions and what the bond lengths and directions are between Fe and O), and the orientation of the topmost layer in the bilayer with respect to the underlying Pt lattice. To address these questions, we have studied two coverages of iron oxide films, 0.75 and 1.0 ML, with the simultaneous study of this system by XPD, STM, and LEED ultimately providing more quantitative answers to all of these questions [5a].

For thicker iron oxide layers grown on Pt(111), LEED [13,14], STM [12], and NEXAFS [15] studies report that Fe_3O_4 with (111) orientation is grown by repeating the process of 1 ML iron oxide growth at an oxygen pressure of ~4x10^{-6} Torr several times (up to about 5 ML for the STM study and about 10 ML for the LEED and NEXAFS studies). A LEED I-V analysis also suggested that the outermost layer is terminated with 1/4 ML of Fe, and that fairly large changes in the vertical interlayer spacings of these films compared to bulk Fe_3O_4(111) are present. STM also indicated an SK growth mode. However, it has also been suggested from STM results that α-Fe_2O_3(0001) can be grown if the oxygen pressure is raised to ~5x10^{-4} Torr, illustrating the high sensitivity of the system to oxygen pressure and preparation conditions [12]. We have thus extended the present study to thicker layers of iron oxide grown in the same manner on Pt(111). FeO_x film thicknesses from ~0.75 ML to ~1.75 ML in steps of ~0.25 ML, as well as ~3.0 ML were investigated using XPD, STM, and LEED in order to better understand the growth mechanism of these iron oxides, as well as their internal crystal structures.

Section 2 describes the unique instrumentation that was designed and constructed, as well as certain experimental procedures, including the oxide growth method. Section 3 considers coverages, chemical states, and stoichiometries of iron oxide films through the entire coverage range, as derived from conventional <u>and</u> more accurate direction-averaged XPS analysis. The atomic structure results are divided into two sections: Section 4 considers oxide coverages up to 1.0 ML, and Section 5 thicker oxide coverages from 1.25 ML to 3.0 ML. Finally, Section 6 presents our overall conclusions, including comments on the complementary information provided by these three structure probes.

2. EXPERIMENTAL

The special instrumentation developed as part of this study is shown in Fig. 3(a), and it permits combining XPS, XPD, LEED, and STM in the same UHV system. A custom-built UHV specimen preparation and characterization chamber equipped with four-grid LEED optics (Princeton Research, Model 118) and an STM (McAllister Associates, with Nanoscope II control system) was added to an existing Vacuum Generators ESCALAB5 photoelectron spectrometer. This chamber could be isolated from the spectrometer with a viton-gasketed gate valve. The spectrometer had also in prior work been equipped with externally-selectable tube arrays for high-accuracy angle definition [34] and with a multichannel detector [35], as described in detail elsewhere. The LEED/STM chamber also provides for deposition of Fe by means of a Knudsen cell, and monitoring of deposition thickness by means of a quartz-crystal microbalance (QCM--Inficon Model 751-001-G1). The custom-built, long-travel, two-axis sample goniometer shown at the left of Fig. 3(a) permits moving specimens from the XPS/XPD position in the spectrometer to the LEED/STM/preparation chamber. The two-axis goniometer with the Pt(111) sample in place is shown in Fig. 3(b): spring clips bring in the current and high voltage necessary for electron bombardment heating of the sample. In addition, two socket-head screws at the extreme right of Fig. 3(b) can be loosened in vacuum with a specially-modified commercial wobble stick, permitting removal of the sample from the goniometer and placement of it (via an interim stage) onto the STM. The sample is shown in mid-transfer in Fig. 3(c). The coarse-approach STM rails of tungsten carbide were equipped with a low-friction "sled" made of the alloy Ampco 18 to facilitate smooth approach using the standard inertial jerking mechanism. A set of reference samples, as well as other rotatable single-crystal samples (not shown here), could be loaded onto the goniometer in this position. The basic operation of the sample rotation mechanism has been discussed previously [34,35], and more details concerning the sample transfer mechanism and other features of this new instrument appear elsewhere [5b].

All XPD, XPS, LEED, and STM data reported in this paper were obtained in this single UHV system with base pressures less than 8×10^{-11} Torr in the XPS/XPD chamber and less than 1×10^{-10} Torr in the STM/LEED chamber. The Pt(111) sample cleaning and Fe oxidation were done in the XPS/XPD chamber and Fe deposition was done in the STM/LEED chamber. Wherever results from these different techniques are compared, they are from the same preparation of a given surface.

The platinum single crystal was cut and oriented within less than ± 0.2° of the (111) plane, polished by the usual metallurgical procedures, and then mounted onto the goniometer of Fig. 3(b). The misorientation of the Pt(111) was judged by both Laue back diffraction and the step density as seen in typical wide-scan STM images on clean Pt(111). For example, terrace widths of ≥ 400 nm were typical from several STM images taken on the clean Pt surface [5b]. This Pt(111) crystal was mounted on a ceramic goniometer barrel, and could be heated by electron bombardment from the back. The temperature was measured with an infrared pyrometer that was initially calibrated by a chromel-alumel thermocouple mounted directly on the top of the Pt crystal. The clean Pt surface was prepared by repeated cycles of sputtering with 1 keV Ar ions and subsequent annealing to T = 1500 K in 4×10^{-6} Torr oxygen. A final heating to 1500 K for about 30 sec without oxygen resulted in a clean surface. This cleaning procedure has been used in previous studies of FeO_x/Pt(111) [9-15]. The cleanliness of the surface was checked by XPS core-level peaks and no detectable contaminant peaks were found. A very well ordered surface was also verified by a sharp (1x1) LEED pattern.

The iron oxide thin film growth was done in two steps. First, iron was evaporated onto the clean Pt(111) surface using 99.999% pure iron wire wrapped around a resistively heated tungsten wire. The QCM was used to adjust the deposition rate to ~1 Å/5 min., for which the maximum pressure during the evaporation was about 4×10^{-10} Torr. After depositing the desired amount of iron onto the clean surface, the sample was heated to T = 980 K for about 1 minute in 4×10^{-6} Torr oxygen and cooled rapidly down to room temperature afterwards. This growth method was thus identical to that used in prior LEED, STM, and NEXAFS studies [12-15] for ≤ 1 ML of oxide, but different for thicker layers in that our oxidation was done in a single-step for the full thickness of Fe, rather than being repeated for each successive single monolayer of Fe to build up the full thickness as in this prior work.

All photoelectron spectra for XPS and XPD were obtained with Al Kα excitation (1486.7 eV). The experimental geometry for the XPS/XPD measurements is described in detail elsewhere [5,34,35], but Fig. 4 defines important angular variables. All XPD data were obtained with precisely-determined angular acceptances of ± 3.0° using a tube array before the analyzer entry [34], and with a new custom-developed software system which permitted automated rotation of both the polar (θ) and the azimuthal (ϕ) angles of photoelectron emission during XPD data collection [36]. This software also contained the capability that up to 10 different photoelectron peaks could be measured at each emission direction: thus, XPD data from each element were obtained for exactly the same sample positions and surface conditions. For each direction of emission in an angle scan, three core photoelectron peak intensities were measured: Pt 4f at ~1414 eV kinetic energy, Fe $2p_{3/2}$ at ~777 eV, and O 1s at ~956 eV. These kinetic energies are high enough to exhibit strong forward scattering effects in photoelectron diffraction [2, 37-40]. Taking all three spectra simultaneously permitted very accurately registering diffraction features from one element to another, and in particular to low-index directions in the Pt substrate, and determining both azimuthal and polar alignments more precisely than is possible from an analysis of LEED spot patterns alone. LEED was used as a cross-check on these alignments, however. Intensities were measured over essentially the full 2π steradians above the sample surface, from 6° above the surface plane ($\theta = 6°$) to the surface normal ($\theta = 90°$). To reduce data collection times, each large-scale XPD intensity set or diffraction pattern was measured over only a 120° sector in azimuth above the sample and a 2π intensity map then completed by exploiting the threefold symmetry of all of the surfaces studied. However, the accuracy of this threefold data folding was justified for each case by comparing the individual 120° intensity scans in the large data set to selected full 360° azimuthal XPD scans. The polar emission angle from the surface was first set to $\theta = 6°$ and then increased to 90° in steps of $\Delta\theta = 2°$ after each 120° azimuthal rotation. The azimuthal step size was $\Delta\phi = 2°$ for $\theta = 6°$, and was increased with increasing polar angle θ so as to give an almost uniform sampling density in solid angle over the hemisphere, thus reducing data acquisition time, a procedure first introduced by Osterwalder et al. [41]. The true θ and ϕ varied only slightly from the expected values after completing a full 2π intensity map; the total accumulation of minute errors in setting angles is estimated to be $\leq \pm 1.5°$ for ϕ and $\leq \pm 0.2°$ for θ.

Two different types of STM tips were used in this study: diagonally-cut Pt/Ir alloy wires and electrochemically-etched W wires, both of 0.25 mm overall diameter. Both types of tips gave good atomic images, with no systematic differences in behavior between them. The STM images consist of

400x400 data points, and were obtained in either constant-current or constant-height mode, with bias voltages of sample relative to tip and tunneling currents as given below for each case considered. All the dimensions reported here were obtained after accurate calibration of the x, y, and z piezo scales (with x and y being in the surface plane, and z being perpendicular to it). The x and y piezoes were calibrated by measuring the atomic spacings on a reference highly-oriented pyrolytic graphite (HOPG) sample, while the z piezo was calibrated from multiple measurements of the monatomic step heights of the clean Pt(111) surface.

LEED patterns were recorded with a Polaroid camera, and obtained at a few energies to verify the types of diffraction patterns seen. No current-versus-voltage curves were measured. The stability of the long range order of clean Pt(111) and of iron oxide films grown on Pt(111) was checked via LEED patterns and no detectable changes were found before and after a complete set of XPD data collection and STM imaging.

3. Fe COVERAGE, Fe-O STOICHIOMETRY, AND CHEMICAL STATE

The coverages of Fe as initially deposited and before oxidation were determined using the QCM, and then cross-checked using a standard XPS quantitative analysis method for the case of a semi-infinite substrate with an overlayer of uniform thickness [42-44]. The QCM values are measured via an average density of bulk Fe which in turn corresponds to an average areal density of 1.93×10^{15} atoms/cm^2. The XPS values are referenced to the Pt(111) surface, with a smaller areal density of 1.51×10^{10} atoms/cm^2; thus the XPS values might be expected to be about 28% higher. The QCM coverage before oxidation is used to denote the overlayers in all of the following discussion; thus, 1.00 ML Fe corresponds to 1.93×10^{15} atoms/cm^2 initially deposited. . The details of the quantitative XPS analyses for this case, as well as the Fe:O stoichiometry analysis after oxidation are discussed elsewhere [5b] and these results are summarized in Table 1. The Fe coverages as determined by QCM and XPS before oxidation are in good agreement, showing differences of generally less than ± 10 %, as shown in the table. Only for the case of 3.00 ML as measured with QCM is the difference about 21%, but it is in a direction so as to be explainable via the areal density ratio mentioned above. In addition, relatively wide scan STM images after oxidation also provided an independent coverage determination for this system, since regions of the surface with the monolayer structure of FeO are clearly distinguishable from regions with coverages less than or more than 1 ML, as will be discussed later for each case considered. The results of three independent methods (QCM, XPS, and STM) for determining the coverages of these iron oxide films are thus overall found to be in excellent agreement with one another.

The Fe:O stoichiometry of the final films after oxidation was determined using a standard XPS quantitative analysis method for the case of a semi-infinite substrate with a thin, weakly-attenuating overlayer [43,44], but with full allowance for angle averaging. Fe $2p_{3/2}$ and O 1s peak intensities for each film were obtained by analyzing the full 2π intensity maps in order to avoid previously discussed scattering and diffraction effects [45,46]: azimuthally-averaged data for both peaks were fit with a smooth spline curve in θ so as to derive a θ-dependent peak ratio. The peak intensities over the most reliable range of the 2π intensity maps near the surface normal of $60° \leq \theta \leq 90°$ that are known to minimize spurious effects due to surface refraction and surface roughness [44] were then used for the Fe:O stoichiometry analysis. The 2π intensity maps and the method for averaging intensities at each θ will be discussed later as we consider the XPD data in more detail. With these averaged intensities for both O and Fe, the final Fe:O stoichiometry of the oxide films shown in Table 1 range from $Fe_{1.0}O_{1.07-1.08}$ at ~ 1 ML to $Fe_{1.0}O_{1.4} = Fe_3O_{4.1}$ at 3.0 ML, with the former suggesting FeO and the latter Fe_3O_4. These changes in Fe:O stoichiometry as coverage increases will also prove to be consistent with our STM and LEED data for these surfaces.

In order to further confirm our results for the XPS quantitative analysis of the Fe:O stoichiometry, Fe $2p_{3/2}$ and O 1s peak intensities were also measured for pressed pellets of various freshly-crushed high-purity iron oxide powders: FeO, Fe_3O_4, and Fe_2O_3. Even though the absolute core level binding energies (BE's) of these powder samples cannot be used in a quantitative way due to possible surface charging, the XPS peak intensities were measured in exactly the same way as for the epitaxial iron oxides on Pt(111), including the use of the same average polar angle of emission. The resulting experimental O 1s:Fe $2p_{3/2}$ intensity ratios for these oxides were 0.79, 0.85, and 1.03 respectively. If we choose Fe_2O_3, the most stable form of oxide in air, as a reference, the bulk stoichiometry dictates that these ratios should be 0.68, 0.91, and 1.03, respectively. The experimental ratios for FeO and Fe_3O_4 thus track reasonably well with bulk stoichiometry: only 16% off for FeO and 7% off for Fe_3O_4. Such small deviations are not suprising, since the surfaces of these powders might well have had altered compositions relative to the bulk. Especially for the case of FeO, it is well known that FeO is easily oxidized in air, possibly resulting in the slightly higher O:Fe peak ratio seen in our data. We now consider the same XPS intensity ratios for the epitaxial oxides, concentrating on the most reliable range near the surface normal of $60° \leq \theta \leq 90°$: 0.64 for both 0.75 ML and 1.0 ML, 0.67 for 1.25 ML, 0.69 for 1.50 ML, 0.74 for 1.75 ML, and 0.82 from 3.0 ML. The O:Fe peak intensity ratio for both 0.75 ML and 1.0 ML(0.64) is slightly lower than that of powder FeO, but within 6% of it. The O:Fe peak intensity ratio for 3.0 ML (0.82) is very close to that of powder Fe_3O_4 (0.85) and much below that of powder Fe_2O_3 (1.03). These slightly higher O:Fe peak ratios for the powder FeO and Fe_3O_4 samples can thus easily be explained by the presence of adsorbed H_2O or CO from exposure to air and/or the residual gas in our vacuum system. Overall these results for XPS relative peak intensities on different iron oxide powder samples thus support the results of our prior XPS quantitative analysis, and lead to the conclusion that the average Fe:O stoichiometry is 1:1 for ~1.0 ML and 3:4 for 3.0 ML.

The chemical state of the Fe in the various oxide films can finally be estimated from relative Fe $2p_{3/2}$ binding energies. Fig. 5 shows Fe $2p_{3/2}$ XPS spectra taken from iron oxide films with total Fe coverages of 1.0 ML to 3.0 ML. Binding energies are expressed relative to the Fermi energy, and Pt 4f spectra were also recorded for each coverage to avoid spurious shifts in the Fe $2p_{3/2}$ peak positions. Both the inherently broad Fe $2p_{3/2}$ peak and our lack of high instrumental resolution (full width half maxima on Pt $4f_{7/2}$ = 1.7 eV with an analyzer pass energy of 100 eV) prevents us from resolving the Fe^{2+} and Fe^{3+} species present clearly. However, the Fe $2p_{3/2}$ peak maximum for 1 ML oxide is positioned at a binding energy (BE) of 709.6 eV, that is in agreement with that for an Fe^{2+} species reported earlier [47]. Furthermore, the Fe $2p_{3/2}$ peaks move toward higher BE as coverage increases. This shift is about 1.1 eV from 1.0 ML to 3.0 ML of iron oxide, and is somewhat less than, but comparable to, the 1.5 eV which is reported between Fe^{2+} in FeO and Fe^{3+} in α-Fe_2O_3 by

Brundle et al [47]. Our BE results for Fe are thus consistent with the expected coexistence of Fe^{2+} and Fe^{3+} in thicker iron oxide films on Pt(111), with Fe^{3+} increasing in relative amount, but probably not reaching the 100% level of α-Fe_2O_3. These results thus further support the stoichiometries given in Table 1, with additional confirmation coming from an analysis of our STM images and the results of theoretical simulations of XPD results for 3.0 ML films that will be discussed below. The corresponding BE's in O 1s XPS spectra over the same oxide coverage range (not shown here) exhibit only very small and non-systematic shifts of $\leq \pm 0.1$ eV, consistent with prior observations on oxides of several transition metals including Fe that O 1s BE's are not particularly sensitive to the oxidation state of the cations present [47-50].

4. THE FIRST MONOLAYER OF IRON OXIDE ON Pt(111)

Here we will present and discuss our results for an oxide layer grown from ≤1.0 ML of Fe, in the sequence LEED, STM, and finally XPD. This also was the temporal sequence in which the methods were applied after the preparation of a given iron oxide film, to be certain that only fully characterized overlayers were finally studied by XPD.

LEED:

The LEED patterns shown in Figs. 6(a) and 6(b) , taken with a beam energy of 54 eV for 0.75 ML and 1.0 ML iron oxide films, respectively, are essentially identical, implying that the long-range atomic order in the films is basically the same. These patterns exhibit a nearly hexagonal pattern that is in fact three-fold symmetric if intensities are measured more quantitatively at several voltages. In addition, each of the six main spots is surrounded by a rosette of six satellite spots which are also unequal in intensity and shape, again consistent with overall threefold symmetry. The outermost six satellite spots as viewed from the (0,0) spot,which coincide with the (1x1) or (01), (01), etc. spots from the underlying Pt, show differences in intensities, with three of them being brighter than the other three. This LEED pattern has been observed and discussed in previous studies on this system [9-11,14].

However, our results show in addition that the inner three satellite spots among each set of six (that is, those that are closest to the (0,0) beam) are more diffuse and streaked than the other three. However, these streaked spots, and in fact the entire rosette pattern, we observe to become sharper and more nearly sixfold symmetric about its central spot as the initial Fe coverage is increased somewhat above 1.0 ML, as will be discussed in Section 5. The inner six main spots reveal a lateral lattice constant of ~3.1 Å, which is ~12 % larger than the lateral periodicity of Pt(111) of 2.77 Å, and would lead to an areal atomic density $1/(1.12)^2$ smaller than that of Pt(111) or 1.20 x 10^{15} atoms/cm^2 (a value about 20% less than that appropriate to the XPS measurements of coverage (cf. Table 1)). Due to this lattice mismatch, an incommensurate structure and lateral superlattice like that in Fig. 2 and first proposed by Galloway et al. [11] is thought to be formed. Here, approximately 8 interatomic spacings of the overlayer fit into about 9 interatomic spacings of the Pt(111) surface, thus generating a Moiré superlattice. In this structure, the two overlapping atomic lattices (the small periodicity) are rotated with respect to one another by 0.6°, and the resulting Moiré pattern shows atomic coincidence points (the large periodicity) that are rotated by ~5°. Fig. 2 shows both the short and long periodicities which are responsible for the main spots and the satellite spots in the LEED pattern, respectively. The atomic structure proposed also involves only a slight expansion of ~2% in the FeO(111) lateral lattice constant (3.10 Å) relative to that in the bulk, with the lattice constant of bulk FeO(111) in the cubic wustite phase with the NaCl structure being 3.04 Å. In fact, we will show below that the vertical Fe-O interplanar distance is significantly contracted in this overlayer, an effect that is at least qualitatively consistent with an expansion of the lateral lattice constant.

STM:

We will first present STM images of fairly large scanning ranges in order to discuss overall growth morphology and the influence of coverage on morphology, and then consider smaller-range atomically resolved images.

STM images for 0.75 ML and 1.0 ML iron oxide coverages with fairly large scanning ranges (~300-800 nm) are shown in Figs. 7(a) and 7(b), respectively. These are constant-current images with sample biases and tunneling currents given in the figure captions. In Fig. 7(a), the oxide has grown across two steps of monatomic height in the upper left of the image; and in Fig. 7(b), across two monatomic steps in the middle of the image, and one at the far right of the image. These images also provide information on the oxide coverage, since they are fairly large scale and were found to be typical over several scans in different regions. As might be expected for a submonolayer coverage, the image for 0.75 ML in Fig. 7(a) shows some darker = lower, and presumably empty, regions, and these are found to occupy about 25% of the terraces, in good agreement with our QCM and XPS coverage measurements [5b]. More interesting in Fig. 7(a) is the observation that this submonolayer oxide appears to grow as elongated islands or lateral columns. As measured relative to the dark areas, these elongated oxide islands furthermore have typical widths of 30-40 Å and a height of about 2 Å. This height is about the same as the ~2.6 Å estimated thickness of a (111) bilayer of Fe and O arrived at by considering the ionic radii of Fe^{2+} and O^{2-} and the vertical interlayer distance of 1.25 Å between them to be determined in a later section. The 1.0 ML image in Fig. 7(b) generally shows atomically-smooth terraces, with some small islands here and there indicative of second-layer growth, and there is no more evidence of elongated islands growth. For this surface, the islands and a few small empty "defect" regions occupied less than 10 % of the total area, suggesting a nearly perfect bilayer of Fe and O. It is thus noteworthy that two surfaces with such different morphology in STM can at the same time yield LEED patterns that are nearly identical. However, the widths of these elongated oxide islands, which are equivalent to about 1-2 unit cells of the superlattice in Fig. 2(b), are found in a kinematical simulation of the LEED patterns to yield results that are in reasonable agreement with experiment, even as to the streaking of the inner rosette spots, provided that we assume that there are three symmetry-equivalent domains of such islands separated by 120° to yield the overall threefold symmetry [5b]. These simulations are shown in Figs. 6(c)-(e) for different sizes of the ordered overlayer considered, but we defer a detailed discussion of them until after the detailed atomic structure has been determined.

Fig. 8(a) now shows a 5.8 nm x 5.8 nm constant-height image of 1.0 ML of FeO on Pt(111). The low-index direction shown here was determined from full 2π Pt 4f XPD data on clean Pt(111). In agreement with prior STM work on this system by Galloway et al. [11], it is clear that 1 ML of FeO on Pt(111) can be imaged by STM, even though bulk FeO is an insulator with a 2.4 eV band gap [51]; in fact, the prior study made use of even lower bias voltages that are typical for tunneling on metal surfaces. The image in Fig. 8(a) clearly shows the existence of two periodicities with small and large unit cells, as indicated by the outlines. The large unit cell is drawn at the approximate center of a region that is brighter on the average. The small unit cell is of atomic dimensions, 3.1 Å ± 0.1 Å on each side, as derived most quantitatively from a Fourier transform analysis of the STM image (maximum amplitude at 3.1 Å), while the larger unit cell measures 26 Å ± 2 Å on each side, as more clearly shown in the much larger scale image of Fig. 8(b). Fig. 8(b) is a 79.2 nm x 79.2 nm constant height image. Only the large unit cell periodicity is visible in this image, although it is defected, thus creating different domains of sixfold symmetry that are difficult to distinguish. These larger unit cells are thus responsible for the satellite spots shown in the LEED pattern in Fig. 6(b), as discussed previously by Galloway et al [11]. This prior STM study also reported that there is about a ± 5° rotational mismatch between two domains of the long-range periodicity on adjacent terraces. We have also observed this rotational mismatch of two domains separated by defected islands on a single terrace, as shown by the two dark lines in the lower image of Fig. 8(b). This difference in results might be because our Pt(111) surface had a lower step density than in this prior study (about a 0.4° miscut from (111) here, compared to the 1.0° miscut used previously [11]).

XPD-Experimental Results:

We now consider XPD data obtained simultneously from Pt, Fe, and O for these iron oxide overlayers, with the goal of determining their internal atomic structure. The raw $I(\theta,\phi)$ data for the Pt, Fe and O 2π intensity maps have no correction for instrumental response, which in general makes intensity fall off to zero as θ goes to zero (i.e., for emission parallel to the surface) [43,44]. These $I(\theta, \phi)$ results were corrected for instrumental effects in two steps. First, in order to smooth out the diffraction features, azimuthally-averaged intensities at each θ were fit with smooth spline functions [52]. This spline function provides an estimate of the intensity in the absence of photoelectron scattering at each θ that we shall denote by $I_0(\theta)$. Then the normalized XPD intensity modulation function $\chi(\theta,\phi) = [I(\theta,\phi) - I_0(\theta)]/I_0(\theta)$ is calculated for display and analysis. These χ functions put equal fractional anisotropies on the same footing regardless of polar angle, and automatically incorporate corrections for instrumental response. Fig. 9 shows stereographic projections of such experimental 2π χ maps for Pt 4f, Fe $2p_{3/2}$, and O 1s, with oxide coverages of 0.75 ML (left panels in (a)) and 1.0 ML (right panels in (b)). Intensities are given in a linear gray scale representation, with brighter meaning higher intensity. The total collection time for a set of data for Pt, O, and Fe was about 4-1/2 days for each coverage, with this time being significantly lengthened relative to standard operation of the spectrometer due to using a ±3.0° tube array so as to better define angles and effective sample area [34]. All three intensities were measured in sequence at each direction so that the final intensity maps are in exactly the same crystallographic orientation. The threefold data folding was justified for each case by comparing selected 360° azimuthal scans in the 2π intensity maps to full 360° experimental azimuthal scans at the same polar angles [5b]; also of course, the LEED patterns showed threefold symmetry. These selected full-azimuthal-scan data and LEED patterns taken before and after XPD data collection also permitted us to verify that there were no noticeable changes in either the short-range or long-range order of the films, respectively, during the XPD data collection. Relative XPS peak intensities for each element taken before and after XPD measurements also did not show any noticeable change. Thus, both the composition and the structure of these oxide films were stable over the rather long times needed for the XPD data collection, even though bulk FeO is relatively easily oxidized in air.

Even though XPD is a short-range atomic order probe, the pairs of Pt, O, and Fe XPD patterns are essentially identical for these two coverages, in qualitative similarity with the LEED results which selectively probe a different property: longer-range order. For XPD, this identity includes the actual degree of azimuthal anisotropy in the pattern, as measured in a standard way by $\Delta I/I_{max}(\theta) \equiv (I_{max}(\theta,\phi) - I_{min}(\theta,\phi))/I_{max}(\theta,\phi)$ in %, which is found to be essentially the same for all patterns for 0.75 ML and 1.0 ML. For example, these values for the polar takeoff angle of 20° passing through the three strongest peaks for Fe $2p_{3/2}$ are ~50 % for both coverages. Thus, XPD implies that the internal short-range structure in these two overlayers is the same, even though STM shows a quite different long-range structure. In the following discussion, we will focus on the XPD data for 1.0 ML coverage, as it represents a more ordered structure, although any conclusions concerning short-range structure will also apply to the 0.75 ML case.

In some of our subsequent discussion, we will state specific anisotropies in %, usually for the azimuthal scan exhibiting the highest value for a given pattern. Such numbers are useful, e.g. in comparing different surface preparations or experiment with theory. However, theory in general is found to overestimate anisotropies for several previously-discussed reasons [2].

The Pt 4f XPD patterns in Figs. 9(a) and 9(b) are dominated by the strong forward-scattering and interference effects that are well-known in single-crystal substrates [2, 38-40]. These patterns are rich in structure, with for example, maxima along <110> near-neighbor directions at a polar angle of 55°. Also, strong forward scattering peaks are clearly shown at a polar angle of 35° and azimuthal angles rotated by 60° from the $<11\bar{2}>$ directions and corresponding to the $<\bar{1}2\bar{1}>$ directions. Additional lines of intensity and fine structure are also seen, and these also are familiar in high-energy emission from single crystals [53]. The relatively narrow bands of higher intensity across the Pt diffraction patterns are again due to forward-scattering along planes of atoms, and have been shown to be related to Kikuchi bands at energies above about 1 keV [54,55]. The Pt 4f XPD patterns of ~ 1 ML iron oxides on Pt(111) in Fig. 9 also do not show any noticeable changes compared to the pattern for clean Pt(111) (not shown here, but presented in ref. 5) because the intensity modulation is dominated by scattering and diffraction in the bulk platinum.

The Fe $2p_{3/2}$ XPD results in Fig. 9 show a much simpler diffraction pattern, with three dominant peaks oriented along the $<11\bar{2}>$ azimuths in the Pt(111) surface and at a polar angle of 20° with respect to the surface and weaker fine structure around these peaks. These three strong peaks (which we will later find to be due to forward scattering) are found within experimental error exactly along the $<11\bar{2}>$ azimuths; however, they are not expected to show the 0.6° rotational mismatch with the substrate suggested in the model of Fig. 2 [11], because the angular resolution of our XPD data is only

~± 3.0°, and because there are in any case two domains rotated by ±0.6° whose effects on peak rotation should cancel out if they are equally present on the surface. The azimuthal anisotropy of these peaks at $\theta = 20°$ furthermore has a large value of $\Delta I/I_{max} \approx 50$ % that is indicative of a highly ordered surface with a very high percentage of Fe atoms in the same bonding geometry producing this forward scattering. These XPD data for Fe thus directly imply that there are atoms sitting above the Fe atoms along Pt $<11\bar{2}>$ azimuths and with a bond angle of 20° from the surface. It is thus also suggested that the O layer terminates the surface and is responsible for this forward scattering.

Finally, the O 1s XPD patterns in Fig. 9 are relatively featureless and do not show any strong forward-scattering peaks. There are very weak and broad features, with the overall shape of a hexagonal ring at polar angles between 16° and 24°, but these show anisotropies of only ~12% or less. The O 1s data thus permit the final definite conclusion that the O atoms comprise the outermost layer of the oxide bilayer, with no scatterers between them and the detector.

XPD-Theoretical Simulations:

To test more quantitatively the validity of these qualitative conclusions based on the XPD data, we have carried out theoretical simulations within the single scattering cluster (SSC) model [2,56] of the Fe and O diffraction patterns. These calculations were carried out for the structural model of one ML of FeO(111) shown in Figs. 2(a) and 10. Here, we assume that the bilayer of Fe and O with (111) orientation consists of an outermost layer of O atoms and a second layer of Fe atoms, and that this is placed on top of the Pt(111) surface in a registry so that three strong forward scattering peaks in Fe emission data lie along Pt $<11\bar{2}>$ azimuths, as required by the Fe data in Fig 9. The additional structural parameters of this model can be easily deduced from a combination of the STM and/or LEED results and the Fe and O XPD data. For example, the atomically-resolved STM image in Fig. 8(a) shows that the topmost atoms have a nearest-neighbor distance of ~3.1 Å. On the other hand, the XPD data for Fe and O indicate that there are scatterers above the Fe atoms with bond angles of 20° from the surface. Simple trigonometry then leads to an estimated vertical distance between the Fe and O layers in the oxide of 0.65 Å, which is significantly relaxed from the 1.25Å in bulk FeO(111). In the

SSC calculations, the Pt atoms were not included due to the weakness of backscattering at such high kinetic energies [2,40,57], and planar Fe and O layers were assumed for simplicity (i.e., we neglect any rumpling that might be expected over the superlattice). The cluster diameter was about 20 Å and thermal effects were included via correlated lattice vibrations with a Debye temperature of 420 K. A single scattering approximation (as compared to the more accurate multiple scattering) should be fully adequate for these XPD simulations, since there are only two effective layers of atoms involved, and thus no significant multiple forward scattering pathways over the range of emission angles studied here. The experimental and calculated Fe $2p_{3/2}$ patterns are shown in Figs. 11(a) and 11(b). The calculated χ patterns have been normalized in the same way as the experimental ones to permit a one-to-one comparison. The agreement between experimental and theoretical XPD patterns is remarkably good, and extends even to the weaker dark bands around each stronger peak in intensity, and other aspects of the diffraction fine structure. The calculation thus reproduces both the dominant forward-scattering peaks, as well as various higher-order diffraction features. A separate R-factor analysis has also been performed in which the full-hemisphere XPD data of Fig. 11(a) was compared to SSC calculations for various interplanar distances. The five R-factors used are based on a prior set proposed for LEED analysis [58], but then modified for use in XPD [59]. These R-factors compare experiment and theory via differences of intensities and slopes (R1 and R4, respectively), squares of differences of intensities and slopes (R2 and R5, respectively), and the fraction of the total data range over which experiment and theory have different slopes (R3). Each one of these thus tests the agreement in a slightly different way, and concurrence among all five for a given structure has been found in our group to represent a highly reliable criterion for XPD structure analysis [59]. For the present case, a summary of such results appears in Fig. 11(d), and it leads to clear minima for all five R-factors at an average interlayer distance of 0.68 Å that is in excellent agreement with the 0.65 Å derived from the forward scattering peaks. Our estimated accuracy is ±0.05 Å, as judged by the points at which each R-factor has increased by about 10% from its minimum value.

For comparison, we also show in Fig. 11(c) a calculated diffraction pattern for Fe $2p_{3/2}$ in which the separation between the O and Fe layers has been kept at the unrelaxed distance between adjacent (111) planes in bulk FeO of 1.25 Å, as also proposed on the basis of recent NEXAFS data [15]. The agreement with experiment is very much reduced (as confirmed by the R-factors), with the forward scattering peaks being shifted much too far off the surface (θ ≈ 35°), and an additional triplet of strong features that is not present in experiment also being introduced. This result also confirms the strong contraction of the Fe-O interplanar distance in this bilayer. It has been pointed out previously that the use of forward scattering peaks in this way is expected to be at least twice as accurate for determining bond directions as polarization-dependent NEXAFS [2], and this may explain the discrepancy with one prior study of this system [15]. Finally, additional data supporting this strong interlayercontraction comes from a very recent study involving the theoretical modeling of STM images by Galloway et al. [60], in which it is not possible to get agreement between experiment and theory unless a distance very close to 0.65-0.68 Å is used.

In Fig. 12, we also show experimental and theoretical diffraction patterns for O 1s emission from the relaxed geometry of Fig. 10, and there is again excellent agreement, with theory reproducing the overall diffuse hexagonal pattern seen in experiment at polar angles between 16° and 24°, and neither pattern showing any significant forward scattering features. The shorter-wavelength fringes in the theoretical diffraction pattern of Fig. 12(b) are expected to be smeared out in experiment due to a combination of additional quasi-elastic thermal broadening due to atomic s and the likely presence of some rumpling in the overlayer. Such vibrational effects are commonly included via simple Debye-Waller factors, as we have done, but this approach is not expected to allow fully for the smearing of forward scattering and higher-order diffraction features.

Our data have thus permitted clearly resolving the short-range-order structure of 1.0 ML of iron oxide on Pt(111) as follows: The nearest-neighbor distances of ~3.1 Å are the same for both Fe-Fe and O-O, and these are responsible for the six main spots in the LEED pattern. Oxygen occupies the topmost layer of the bilayer, but it is relaxed vertically inward by 0.60±0.05 Å compared to the (111) planes of bulk FeO.

Overlayer domain orientation and growth mechanism:

Although these combined LEED, STM, and XPD results have served to further quantify the structure of this monolayer of FeO, there is still one question to be answered regarding the binding sites of O with respect to the underlying Fe and Pt. Even though Fe does not have preferred binding sites with respect to Pt because of the incommensurate overlayer formed on Pt(111) (i.e. within the large unit cell, Fe sits approximately on threefold hollow sites in some areas, on bridge sites in other areas, and is close to on-top sites in yet other areas), O can have two different binding sites with respect to Fe while having the same atomic geometry as FeO(111). These two possible structures are shown in Figs. 13(a) and 13(b). In both figures, a bilayer of Fe and O sits on top of Pt(111) with a + 0.6° rotational mismatch so as to produce the previously discussed Moiré pattern and superlattice [11]. However, as viewed from each Fe atom, trimers of O sit along Pt $<11\bar{2}>$ azimuths in Fig. 13(a) (see lower left corner of unit cell, also enlarged at bottom of figure), while these trimers of O sit along azimuthal angles rotated by 60° from the Pt $<11\bar{2}>$ directions in Fig. 13(b) (again see lower left corner of unit cell, also enlarged at bottom of figure). Fig. 13(a) is in fact the structure first proposed by Galloway et al. [11], but these two different structures cannot be differentiated directly from STM, since both would lead to the same kind of superlattice images.

From the excellent agreement between our experimental and theoretical XPD data discussed earlier, we can conclude with certainty that the structure of Fig. 13(a) is completely dominant, with negligible admixture of the structure of Fig. 13(b). In fact, if the two structures were present with equal weight, then the Fe XPD pattern would have to be sixfold symmetric instead of threefold symmetric. The large unit cell and many different types of O-Fe-Pt geometries involved make it difficult to say definitively why the structure of Fig. 13(a) is so strongly favored. But the most reasonable explanation is that the Fe and O atoms are in a different set of atomic environments with respect to the second-layer Pt atoms. That is, if the second-layer Pt atoms are removed from the clusters of Figs. 13(a) and 13(b), then all of the bonding sites in the unit cell of the first figure are exactly duplicated in the second if the latter is simply rotated by 180°. Thus, first-layer Pt interactions with the Fe and O overlayers alone would not lead to any difference between these two structures. To consider this more precisely, if we denote the fcc stacking of Pt in standard notation as A(Pt)B(Pt)C(Pt), then the last two Pt layers can be designated in complete generality as B(Pt)C(Pt). The enlarged region at the corner of the unit cell in Fig. 13(a) with Fe above first-layer C(Pt) atoms and O in interstitial "A" positions can thus be represented as B(Pt)C(Pt)/C(Fe)A(O), and that in Fig. 13(b) by B(Pt)C(Pt)/C(Fe)B(O). This notation clearly indicates the different stacking of the oxygen. The stacking in the geometrically least confused region "1" of the cell in the middle of its lower left half now corresponds to Fe atoms sitting directly above second-layer B(Pt) atoms and O atoms sitting directly above first-layer C(Pt) atoms, so the stacking in this local region can be expressed similarly as B(Pt)C(Pt)/B(Fe)C(O). Now considering the region "2" in Fig. 13(b) that is symmetry-equivalent to "1" via 180° rotation without the second-layer Pt atoms present shows this to represent stacking of the type B(Pt)C(Pt)/A(Fe)C(O), leading to a different local bonding geometry for the Fe atoms that are sandwiched in between the Pt and the O overlayer. Therefore, we conclude that a detailed consideration of all four of the layers discussed above is necessary to explain this dominance of the domain type in Fig. 13(a). It thus appears that the difference in the total surface energy between the two structures must be large enough to strongly favor one of them near the 1 ML coverage regime. We prefer this explanation to a difference in the kinetics of the initial formation of the two domain types, although it is impossible to completely rule out the latter. This difference in energy (or kinetics) could in turn be small enough to permit favoring the other structure in Fig. 13(b) at higher coverages involving some oxide islands in subsequent layer(s), and we will see evidence for this for the case of a 1.50 ML oxide to be discussed in the next section.

We finally discuss the possible growth mechanism of these thin oxide layers on Pt(111) in terms of the elongated island or columnar structures seen in the STM image for the 0.75 ML oxide in Fig. 7(a) . We propose that the oxide growth nucleates where the Fe sits in the lowest energy sites, probably threefold-hollow sites on first-layer Pt with maximum coordination numbers that occur midway between the corners of the large unit cell in Fig. 2(b) or in region "1" of Fig. 13(a). The oxide then continues to grow to the higher energy sites such as the bridge sites just adjacent to the threefold-hollow sites, and can grow as an elongated island in a zigzag fashion that oscillates between threefold and bridge. The highest-energy sites would probably be the on-top sites at the corners of the unit cell, with these perhaps being occupied last along the edges of an elongated island or column. It is also interesting to note that these oxide islands in Fig. 7(a) have widths of approximately 35 Å, which is about 1.5 unit cells in width, making it appear that this unit cell is also the basic growth unit. In this model, the oxides could grow in such elongated islands or columns with three different orientations of equal probability 120° degrees apart, perhaps explaining the streaked satellite spots in the LEED patterns of Figs. 6(a) and (b). One of the three possible orientations is shown in the STM image of Fig. 7(a). However, a more detailed investigation of submonolayer growth would be needed to verify this possible growth mechanism, including its influence on the streaked LEED satellite spots.

The growth mechanism we have proposed for these elongated islands is also qualitatively supported by a simple kinematical LEED analysis shown in Figs. 6(c)-(e). For simplicity, only the first-layer Pt atoms and Fe atoms were considered, as they are expected to be the strongest scatterers in the problem. In addition, although multiple scattering between the overlayer and the substrate would be needed to adequately model the satellite spots [4], we have simulated this in an approximate and phenomenological way in single scattering by modulating the amplitudes of the Fe scattering factors in the overlayer with a two-dimensional sinusoid of the same periodicity as the Moiré pattern. This procedure artificially introduces the periodicity of the superlattice without requiring prohibitively time-consuming multiple scattering calculations on a very large cluster. This model should be adequate for modeling the spot locations and perhaps the streaking, but is not expected to reproduce details such as relative intensities of the different features. Figs. 6(c)-(e) show calculated LEED spot patterns for this Fe/Pt(111) superlattice with the structure of Fig. 2 and for different lateral cluster sizes, as finally threefold symmetrized via a sum over three orientations 120° apart. In Fig. 6(c), a circular cluster of 200 Å diameter including about 8 superlattice repeat units in both of the lateral directions x and y was used. In Fig. 6(d), a rectangular cluster 200 Å long in x and 52 Å wide in y was used to simulate the elongated islands or columns of oxide growth seen in the STM image of Fig. 7(a); this corresponds to ~ 8 and ~2 superlattice repeating units in x and y, respectively. And finally, in Fig. 6(e), a cluster with a diameter of 60 Å and only about 2 superlattice cells in both directions is used to represent a minimal island size. Only a band of intensity spanning the most intense spots and their satellites was calculated due to the computationally-intensive nature of these calculations. The calculated LEED pattern for Fig. 6(c), a simulation for the case of long-range order over a fairly large area, well reproduces the six main spots as well as the six satellite spots. Furthermore, the distances between the main spots and the satellite spots well reproduce the experimental ones, and are thus fully consistent with the large periodicity of ~ 26 Å seen by LEED and STM. A minor point of disagreement is that the outermost six spots associated also with Pt(111) are brightest, whereas in experiment, the six spots in the center of the satellite ring and associated with FeO(111) are the brightest. However, for a calculation at this simple and phenomenological level, such minor disagreements are not surprising. For the simulation of elongated islands shown in Fig. 6(d), the six satellite spots are still apparent, although a little weaker compared to the case of Fig. 6(c) and with streaking between them that is qualitatively like that in the experimental data of Fig. 6(a). However, the streaking is not as pronounced in theory as in experiment. For the least ordered case shown in Fig. 6(e), the satellite spots are still visible, but much broader and streaked compared to the other cases; in fact, the satellites here begin to look more like those in experiment for ≤ 1.0 ML. Interpreting these LEED simulations qualitatively, we can thus say that the streaked satellite spots seen in the experimental data are probably due to diminished long range order in the oxide overlayer. Although multiple scattering calculations for similar clusters including also a topmost O layer and possible surface rumpling would be necessary to analyze these LEED results more quantitatively, the present simple simulations serve to further support the structural model discussed above.

Our structural model for 1 ML of FeO on Pt(111) thus fundamentally agrees with the FeO bilayer superlattice proposed by Galloway et al. [11], but adds to this picture that oxygen forms the outermost layer, that the Fe-O interlayer distance is significantly contracted to about 1/2 of that in bulk FeO(111), and that the oxygen atoms preferentially sit along Pt $<11\bar{2}>$ directions as viewed from their nearest-neighbor Fe atoms (requiring a consideration of interactions among four atomic layers for its explanation). In fact, several previous studies [61] have reported the existence of a monolayer of FeO either at a surface or at an interface between a metal and an oxide before growing Fe_3O_4 or Fe_2O_3, even though bulk FeO is not an equilibrium phase at room temperature [24]. In the present case, it seems quite reasonable that one ML of FeO/Pt(111) can be stabilized by reducing its polar surface instability due to the net electric dipole moment perpendicular to the surface, through both a slight lateral expansion of ~0.06 Å in its unit cell dimensions and a rather large inward relaxation by about

0.6 Å. These observed relaxations also result in an Fe-O bond length of ~1.90 Å that is ~0.25 Å shorter than that of bulk FeO (2.15 Å), but very close to that of the tetrahedrally-coordinated atoms in bulk Fe_3O_4 (1.88 Å). Thus, from the point of view of both FeO(111) polarity and Fe-O bond length, the structure we have found for this FeO monolayer is reasonable.

5. THICKER LAYERS OF IRON OXIDE ON Pt(111)

LEED:

Fig. 14 shows LEED patterns of FeO_x films grown on Pt(111) for iron oxide coverages from ~1.25 ML to ~3.0 ML. Up to 1.75 ML, these patterns are very similar to those shown previously in Figs. 6(a)-(b) for ≤ 1.00 ML of FeO, with the exception that the rosettes representing the superlattice satellite spots actually get sharper and more uniform in shape for coverages above 1 ML. These LEED patterns thus imply that the dominant long-range structure of the iron oxide films is almost the same up to about 1.75 ML coverage as that of 1 ML FeO/Pt(111). In fact, the sharpening of the rosettes further suggests that the FeO superlattice structure is actually more ideal when the coverage is increased somewhat above 1.0 ML. For the thickest iron oxide film we studied (3.0 ML), the superlattice satellite spots disappear, and a fuzzy (1x1) LEED pattern suggestive of moderate order is seen. This LEED pattern for 3.0 ML thus indicates that the incommensurate 1 ML FeO superlattice is no longer present, and that there is diminished long-range order compared to lower coverages. In addition, we also observed very faint and streaked (2x2) LEED spots at this maximum coverage, even though they do not show in the photograph reported here. Such (2x2) LEED spots are consistent with previous LEED and STM studies [12-14] of what has been suggested to be an Fe_3O_4(111) overlayer; Fig. 1 in fact shows one termination of this surface that would lead to (2x2) features. The LEED patterns obtained previously for a total 8 ML coverage by Barbieri et al. [14] and with a multiple deposition and oxidation procedure starting with 1 ML of Fe each time in fact gives sharper principal spots, and a better defined (2x2) pattern.

STM:

Large-scan STM images of $FeO_X/Pt(111)$ for each of the coverages studied are shown in Fig. 15. Although the LEED patterns from 0.75 ML to 1.75 ML are almost identical, the STM images show marked new features as the coverage is increased even slightly above 1 ML. For example, the STM image in Fig. 15(a) of a 1.25 ML oxide film shows small islands growing on a generally atomically-flat base layer; these small oxide islands have grown preferentially near a step that is monatomic in height and oriented along the diagonal in the image; another such step is in the upper left portion of the figure. This image also shows small darker regions, perhaps indicating that the Pt surface is not completely covered by the base FeO oxide layer for a 1.25 ML film.

On the other hand, STM images for the higher coverages of 1.50 ML and 1.75 ML shown in Figs. 15(b) and 15(c), respectively, develop larger islands on the flat base layer, and these begin to coalesce for 1.75 ML. For 1.5 ML, the oxide has grown across one monatomic step in the middle of the image and no more empty regions are observed, indicating a complete covering of the Pt surface by the base layer of oxide. The image for 1.75 ML also clearly shows multilayer growth, with islands of at least two levels being visible; by contrast, mostly one level of islands is observed for 1.50 ML. For 1.50 ML, the heights of the islands as measured by the STM are about 4.6 Å and the area occupied by them is found to be about 26 % of the total area as computed from several large-area images. For 1.75 ML, the oxide has grown with what are imaged in the STM as two different heights of the islands: a topmost set about 5.0 Å in height as measured from the islands just below and occupying about 5 % of the total area, and a lower set about 9.7 Å in height as measured from the flat base layer and occupying about 58 % of the total area. The vertical line along the right quarter of the 1.75 ML image appears to be a set of four bunched monatomic steps, probably linked to the initial substrate topology. Step bunching in fact was found to increase on the clean Pt(111) surface as the number of oxidation and cleaning cycles was increased during the course of this study, even though only monatomic steps separating large terraces were seen for a fresh sample at the beginning of the experiments. Such step bunching could be due to surface roughening induced by the repeated cycles of oxidation and annealing of the Pt crystal and/or residual impurities present on the surface below the limit of about 1 % ML for the case of C or O that can be detected in our XPS analysis [44,62].

Thus, we see islands of about 4.6-5.0 Å and 9.7 Å height for these two cases, as measured with respect to the layer just below. These heights can be compared to the bulk repeat distances between equivalent (111) oxygen planes in bulk FeO of 2.5 Å, and in bulk Fe_3O_4 of 4.85 Å. The 4.6-5.0 Å islands thus have an apparent height that is about two FeO repeat distances or one Fe_3O_4 repeat distance, and the "double-height" 9.7 Å islands below have an apparent height of four FeO repeat distances or two Fe_3O_4 repeat distances. Changes in surface electronic densities of states and effective conductivities with lateral island size (the average diameters of the islands are ~25 nm and ~70 nm approximately for 1.50 ML and 1.75 ML, respectively) and/or internal crystal structure (e.g. FeO versus Fe_3O_4) from one region of the surface to the other could easily cause these STM heights to differ from actual surface heights. Tip geometry effects could also lead to such differences. These effects prevent making a fully quantitative connection between the STM results and the overall oxide coverages involved, but some approximate numbers follow.

As one method of checking the meaning of these STM-derived island heights and coverages, we have calculated the total Fe coverage on the surface from the above fractional areas covered by each type of island, assuming for simplicity an FeO stoichiometry in the base layer, and an Fe_3O_4 stoichiometry with 3/4 the areal Fe density in the islands lying on top of it. In this coverage calculation, the flat base layer seen by STM is assumed to be the FeO(111) oxide superlattice discussed in the last section, as will be verified by STM and XPD below. If we first consider an island height of ~4.6-5.0 Å to be 1 bilayer of Fe and O and a height of ~9.7 Å to be 1 bilayer also, the 1.50 ML film is found in STM to correspond to a 1.20 ML coverage, and the 1.75 ML film to a 1.47 ML coverage, numbers which are both close to, but somewhat lower than, the coverages derived from QCM and XPS. If by contrast we assume that both the 4.6 Å and 9.7 Å layers consist of 2 bilayers of Fe and O or one Fe_3O_4 repeat distance, the corresponding STM coverage for 1.50 ML is 1.39 ML and that for 1.75 ML is 1.94 ML, values which are overall closer to the QCM and XPS coverages. Going further to assume that the 4.6 Å islands consist of 2 bilayers and the 9.7 Å islands of 4 bilayers gives coverages of 1.39 ML and 2.81 ML, with the latter being much too large compared to QCM and XPS. We thus conclude that both types of islands are probably 2 bilayers or one Fe_3O_4 repeat unit in height, and that the anomalously high 9.7 Å value for 1.75 ML may be due to changes in the surface density of states and/or local conductivity on this type of island, as well as to possible effects of the tip shape or the surface atomic composition. Corroborating evidence for this conclusion comes from the fact that multiples of 4.8 Å step heights have been reported in a prior STM study of α-Fe_2O_3(0001) in which repeated cycles of Ar^+ bombardment and subsequent high temperature annealing were carried out [31a]. In this study, these step heights were assigned to 2 bilayers of Fe and O in Fe_3O_4(111), with the conclusion that α-Fe_2O_3(0001) has been reduced to Fe_3O_4(111) in the selvedge region by repeated cycles of ion bombardment and annealing. A more recent STM study of Fe_3O_4(111) with ion bombardment and annealing in O_2 [31b] suggests that two types of surface termination are possible, with the greatest step height between them being 3.6 Å, or close to one repeat distance. In summary, with the assumption that both island heights correspond to one repeat distance of Fe_3O_4, the total Fe coverages we estimate from STM are found to be in good agreement with those expected from QCM and XPS, but a more quantitative comparison is not possible from our data.

Finally, we consider the STM image for a 3.0 ML film shown in Fig. 15(d). This image is different from the others in showing even more marked multilayer growth and many smaller islands in the topmost layers. There are several heights of islands spanning at least four levels, with the topmost islands being about 26 Å from the lowest layer as measured in line-cut profiles using the STM software [5b]. The lowest (dark area) layer consists of small patches with sizes of about 10 nm in diameter, and we suggest that this still represents the first base layer of FeO(111), as seen above for the 1.50 ML and 1.75 ML coverages. Measuring island heights is even more difficult for this multilayered structure. However, the islands just on top of the lowest layer (darkest in the image), which have the largest total area, are found to have heights of about 5 Å as measured at several places in the image: this we again suppose be 2 bilayers of Fe and O (that is, one repeat unit of Fe_3O_4). No patches with the base FeO-type bilayer were resolvable in this image, consistent with the absence of any superlattice spots in the LEED pattern. Thus, thicker oxides layers of 1.75 ML and 3.0 ML grown in our one-step recipe do so via multilayer stacks of oxide islands instead of layer-by-layer.

The fact that the LEED patterns for 1.75 ML are almost the same as those for 1 ML of FeO(111), but with even sharper superlattice spots, also indicates that the flat base layer seen by STM for higher coverages is still the incommensurate oxide overlayer, and not the underlying Pt surface. This coexistence of the base FeO(111)-type bilayer and the overlying oxide islands is also confirmed by STM, as illustrated in the image obtained for a 1.75 ML oxide film and shown in Fig. 16. Although slightly noisy in the upper half, the lower half of this image shows the larger unit cell about 26 Å on an edge that is characteristic of the superlattice (cf. the image for 1 ML coverage in Fig. 8(b)), just adjacent to bright areas that are due to oxide islands formed above 1.0 ML coverage.

The wide-scan and narrow-scan STM images we have presented also permit better understanding the continuous increase in the O:Fe ratio and the shift of the Fe binding energy as the Fe coverage increases (as seen in XPS), as well as the streaked satellite spots at 1 ML coverage or less (as seen in LEED). First, STM shows island growth on top of a 1 ML FeO base layer and these islands occupy more and more of the surface as coverage increases. These islands are expected to have a different atomic structure from the base layer, since the stoichiometry changes and there is also evidence of an increase in the fraction of Fe^{3+} species present. The final stoichiometry at 3.0 ML is also consistent with Fe_3O_4. Thus, we can postulate a change in the overall composition and structure of the oxide film from FeO to a mixture of FeO and Fe_3O_4 as thickness increases, with Fe_2O_3 being less likely on the basis of both stoichiometry and binding energy. We will later discuss the internal atomic structure of the islands in detail when XPD results are considered for each case. Second, we can qualitatively comment on the streaking of the LEED satellite spots shown in the 0.75 - 1.25 ML regime as follows. Fairly large STM images show some empty regions on the surface up to about 1.25 ML coverage that should result in less long-range order compared to the higher coverages. Such incompletely covered iron oxide overlayers for $\leq$1.25 ML also may cause the streakier satellite spots shown in Figs. 6 and 14. Going to higher coverages of 1.50 ML and 1.75 ML thus fully fills and orders the first-layer FeO superlattice and sharpens the LEED satellite spots, even though at the same time, significant oxide island growth on top of this base layer superlattice has occurred.

Overall, we thus find from STM that the growth mechanism of iron oxide on Pt(111) for Fe coverages from 0.75 ML to 3.0 ML is Stranski-Krastanov in nature: iron oxide islands form on top of a 1 ML FeO base bilayer of Fe and O that forms a lateral superlattice. The same sort of growth mode for iron oxide grown on Pt(111) was also reported in prior STM studies in which the preparation procedure was different in being successive one-ML oxidations on top of one another [12] instead of the one-shot procedure used here. Although our STM data cannot be used to determine whether the superlattice persists underneath the islands, the internal structure of these islands will be determined next using XPD.

XPD-Experimental Results:

Fig. 17 shows stereographic projections of full-2π experimental XPD data: Pt 4f in (a), Fe $2p_{3/2}$ in (b), and O 1s in (c) for the same four Fe coverages from 1.25 ML to 3.0 ML. The data collection mode, threefold data folding, and method of calculating normalized χ functions from measured intensities are the same as described in Section 4.

As might be expected, the Pt 4f emission patterns up to 1.75 ML are almost identical and do not show any noticeable changes, since the intensity modulation due to bulk platinum diffraction is dominant. The six strongest peaks are due to two sets of three low-index forward scattering directions: three due to nearest-neighbor scattering along [110] at a polar takeoff angle of 55° and in $<11\bar{2}>$ azimuths, and three due to next-nearest neighbor scattering along [010] at a polar angle of 35° and in azimuths rotated by 60° from $<11\bar{2}>$. For a 3.0 ML oxide coverage, the basic Pt 4f pattern is the same as those of lower coverages, showing the strong nearest- and next-nearest- neighbor scattering features. However, all features are reduced in relative amplitude due to scattering in the overlying oxide, and for $\theta \leq 20°$ this is particularly pronounced, due to the longer path length for escape and the resulting enhanced inelastic attenuation and surface sensitivity.

By contrast, the Fe and O XPD data in Figs. 17(b) and 17(c) show pronounced changes as coverage is increased, going from relatively simple diffraction patterns at lower coverages to more complex ones at higher coverages. The diffraction patterns for 1.25 ML are essentially identical to those of 0.75 ML and 1.0 ML FeO in Fig. 9, showing for Fe three strong forward-scattering peaks along the same emission directions at a polar angle of 20° and the same dark bands and fine structure around these peaks, and for O, the same weak and diffuse hexagonal ring at polar angles between 16° and 24° (cf. Fig. 9). The diffraction anisotropy for Fe at 1.25 ML, as measured at $\theta = 20°$ for the three strongest peaks, is $\Delta I/I_{max} \approx 48$ %, and agrees very well with the 50 % found at ~ 1.0 ML; this implies that the relatively small islands developed at 1.25 ML in the STM images have the same internal structure and/or are not numerous enough or well-ordered enough to contribute significantly to the overall XPD patterns. The Fe diffraction pattern for 1.50 ML coverage still shows the three strongest forward scattering peaks at the same polar angles of 20°, but the strongest of these peaks are rotated from the former Pt $<11\bar{2}>$ azimuths by 60° and the diffraction pattern also starts to show additional features at higher polar angles (e.g., a sixfold set of peaks at the polar angle of ~ 58° with a lower anisotropy of ~ 12 % which were not present at 1.25 ML). For 1.75 ML, the strongest peaks in the Fe data rotate back to their original positions in azimuth but remain at the same polar angle originally associated with the FeO bilayer superlattice, and the additional fine structure at higher polar angles continues to intensify. The rotated positions of the strongest peaks for 1.50 ML cannot be due to any mistake in plotting or data analysis, since the Pt, O, and Fe XPD data were simultaneously obtained along the same emission direction, with the essentially unchanging Pt diffraction pattern thus providing an unambiguous internal reference for azimuth. These rotated peaks furthermore appear to originate from the same FeO base layer seen by STM, because their polar angle is exactly the same as in the 1 ML case, corresponding to the O layer relaxing inward by 0.6 Å. One possible explanation for these results is that the increase in coverage from 1.25 ML to 1.50 ML causes, through the interaction of the islands with the base layer, a shift in the type of base layer formed from that favored at 1 ML (Fig. 13(a)) to that unfavored at 1 ML (Fig. 13(b)). This shift would not change the LEED pattern provided that the two types of base layer were formed in sufficiently large domains. As noted previously, the favored and unfavored structures at 1 ML are almost identical structurally, with the only difference being the stacking of the O atoms with respect to second-layer Pt atoms: thus, the perturbation of the base layer by the islands could lead to a stronger presence of the unfavored structure for 1.50 ML, with an apparent reversal of this effect on going to 1.75 ML. That the 1.50 ML structure is more of a mixture of base layer structures, and thus also local Fe bonding and forward scattering geometries, is also suggested by the variation in anisotropy at $\theta = 20°$, from ~48 % for 1.25 ML down to ~32 % for 1.50 ML, and then back up again to ~38 % for 1.75 ML [5b]. Even though we do not have any quantitative estimates for the surface free energies of these two base-layer structures, the differences between them could be large enough to favor one structure near 1 ML, but small enough to favor the other at higher coverages in the 1.5 ML regime. This point needs further investigation, including a consideration of the interactions between the base layer and the islands formed on top of the base layer, in order to determine whether there is such a driving force to the initially unfavored FeO structure. In any case, the strongest peaks in all of the Fe XPD patterns for coverages from 0.75 to 1.75 ML are well explained as being due to O atoms sitting above Fe atoms in an FeO-type bilayer, with two different domain types probably being present near 1.50 ML.

The O XPD patterns also start to show new features as coverage increases from 1.25 ML, beginning at 1.50 ML with two sets of six weak peaks along what is the diffuse hexagonal ring at lower coverage and with a set of six weaker peaks at higher polar angles around 53° (anisotropy ~ 12 %), plus one peak directly along the surface normal. For 1.75 ML coverage, Fe emission still shows the strongest three peaks along the Pt $<11\bar{2}>$ directions (anisotropy of ~ 38 %), as well as new peaks at the polar angles around 36° (~ 16 %) and 60° (~17 %). O emission at 1.75 ML coverage also shows new features at polar angles around 34° (anisotropy ~ 13 %) and 54° (~14 %). Finally, for 3.0 ML coverage, both the Fe and O diffraction patterns are even more complex, but the basic features seen are already suggested at 1.75 ML. For Fe emission, the peaks at polar angles around 36°-38° and 62° have anisotropies of ~22 % and ~ 20 %, respectively, and for O emission, the peaks at polar angles around 34° and 54° have anisotropies of ~ 18 % and ~ 26 %, respectively. These peaks are all present at the lower coverages, but they produce lower anisotropies as described above. This is consistent with a different internal structure in the oxide islands that are increasing in relative volume.

The generally lower anisotropies for Fe emission data in this coverage range as compared to data for the one ML regime is no doubt due to the presence of more than one type of emitter in the thicker overlayers. Each structurally-inequivalent emitter contributes a different modulation to the overall XPD pattern; this summing over inequivalent emitters will be included in the theoretical modeling or our results to be done in the next section.

We will first discuss our overall XPD data for thicker oxide layers from a qualitative point of view, before going on to compare experiment with theoretical simulations. First, the Fe diffraction patterns for coverages up to at least 1.75 ML exhibit the strongest peaks along Pt $<11\bar{2}>$ azimuths and at a polar angle of 20°. These are clearly assignable to simple forward scattering in an FeO-type bilayer, as shown in our prior comparisons of experiment and theory for XPD patterns from ~ 1.0 ML FeO/Pt(111). The presence of a second type of oxygen orientation in the bilayer causes additional peaks to form along Pt $<\bar{1}2\bar{1}>$ azimuths at 60° away from those of the favored structure for 1.50 ML, but peaks associated with the initially favored structure are nonetheless present over the full range up to at least 1.75 ML. The base layer of FeO and its superlattice are evident in LEED, STM, and XPD up to 1.75 ML coverage, but they are not visible when the coverage reaches 3.0 ML. Second, both the Fe and O XPD patterns develop additional features at higher photoelectron takeoff angles on going to higher coverages, unlike the corresponding LEED patterns, which remain relatively constant up to 1.75 ML. These new features in the XPD patterns can be easily explained as being due to the multilayer stacks of oxide islands that are seen in STM to be forming on top of the flat base layer of FeO. Thus, both Fe and O can now have additional forward scatterers between them and the detector, producing more strong peaks in the XPD patterns at higher takeoff angles. Third, the overall XPD patterns change from being threefold symmetric in the 1 ML regime to being very nearly sixfold symmetric as the coverages increase. This suggests the equal presence of two domains of threefold oxide islands rotated by 180° with respect to one another. Interestingly, the O diffraction patterns for all higher coverages, including even 3.0 ML, are still at least slightly threefold in character, with a difference in anisotropy of the two sets of three peaks at a polar angle of around 54° of ~ 3 %; this was verified by doing full 360° azimuthal scans of both Fe and O intensities [5b]. This further suggests that the two threefold domains are not quite equally present. We will return to the question of azimuthal symmetries for both Fe and O later in comparing experiment with theoretical simulations. However, this symmetry change from threefold to sixfold indicates that the structure(s) of the multilayer stacks of oxides is(are) different from the simple one favored in the one ML oxides, involving both another crystal structure and stoichiometry (as already indicated by our XPS analyses), and threefold-symmetric oxide structures present in two domains with unequal coverage on the surface. Finally, as coverage increases, Fig. 17 clearly shows that both the Fe and O XPD data develop in a continuous way toward the pattern seen for 3.0 ML, even though more radical changes in long-range order (LEED) and topography (STM) are seen in passing from 1.75 ML to 3.0 ML. For example, there are six Fe XPD peaks at polar angles of about 56°-64° that are clearly present over the full coverage range from 1.50 ML to 3.0 ML, with only the polar angles changing slightly with coverage: these peaks are centered at ~58-60° at 1.50 ML, ~62° at 1.75 ML, and ~62° at 3.0 ML. These six peaks are also already present weakly at even 1.25 ML, at a polar angle of 58°. This aspect of the XPD patterns reveals that the short-range structure of the oxide islands for coverages above about 1 ML is already developing toward that of 3.0 ML. Because XPD inherently averages over all possible bonding sites, we will thus in the next section focus on analyzing the 3.0 ML XPD data as a limiting model for the internal structure of the islands seen by STM, and then comment qualitatively on the implications of this for the thinner oxide layers.

XPD-Theoretical Simulations:

We have carried out theoretical simulations of photoelectron diffraction patterns within a single scattering cluster (SSC) model [56] and also for one test case in a multiple scattering cluster (MSC) model [63]. For such thin layers and the high kinetic energies involved, we do not expect multiple scattering effects to be strong, as there are no long chains of scatterers for multiple forward scattering [63]. We comment at the end of this section on the MSC results. Both the Fe $2p_{3/2}$ and O 1s diffraction patterns have been considered for different possible structural models of a 3.0 ML iron oxide film on Pt(111), although any conclusions concerning short-range structure will also be expected to apply to the internal structure of the oxide islands above about 1.50 ML coverage. Due to computational time limitations, we have only in a few cases considered thicker or thinner oxide layers, even though STM indicates that a range of island heights are present. The 3.0 ML calculations on which we finally focus for Fe_3O_4 thus are intended to represent the average seen in XPD. Due to the weakness of backscattering at such high kinetic energies [40,57], as discussed in Section 4, Pt atoms have not been included as scatterers in our calculations. All of the input parameters for the calculations are the same as discussed in Section 4. But unlike the case of an FeO(111) bilayer, where there are only one Fe and one O atom in a (1x1) unit cell, treating thicker oxides of different stoichiometries and structures requires that all Fe and O atoms within the two-dimensional unit cell and in different layers inward from the surface which have different near-neighbor geometries be considered as emitters. For example, $Fe_3O_4(111)$ and α-$Fe_2O_3(0001)$ have (2x2) and ($\sqrt{3}$x$\sqrt{3}$) bulk unit cells, respectively, as shown in Fig. 1. In the unit cells of these three iron oxides, if only the outermost Fe and O bilayer is considered, there are one Fe emitter and one O emitter for FeO(111), three Fe emitters and four O emitters for $Fe_3O_4(111)$, and two Fe emitters and three O emitters for α-$Fe_2O_3(0001)$. In general, each distinct emitter has a different local scattering geometry, as can be seen for the different emitters in Fe_3O_4 in Fig. 1. To reduce computation times, both Fe and O intensities were calculated over only 120° in azimuth, and then the full 2π intensity map was completed by exploiting the threefold symmetry of the structure in the same way as the experimental data. Additional details concerning the calculations, including the actual clusters used, appear elsewhere [5b].

We tested three different types of multilayer iron oxide structures: FeO(111), α-$Fe_2O_3(0001)$, and $Fe_3O_4(111)$. All the structures tested are assumed to have a bottom Fe layer next to Pt (although the Pt atoms were not present in the cluster) as in the case of one ML FeO/Pt(111). A first test group among the possible structures was different numbers of bilayers of FeO(111), up to a maximum of five; this is a reasonable possibility, since we have conclusively shown in Section 4 that the first monolayer grows as an inwardly relaxed FeO(111) bilayer. Among the structural models tested in this group are: (1) two bilayers of FeO with the bulk interlayer distances between all layers, (2) two bilayers of Fe and O with the bottom bilayer relaxed inward as for 1 ML FeO/Pt, (3) the same as structure (2) but with the topmost O rotated 60° from Pt $<11\bar{2}>$ as in the case of the unfavored structure in Fig. 13(b), and (4) five bilayers of FeO with bulk interlayer distances. The structures from (1) to (3) were tested in order to see if they fit experiment for coverages less than 3.0 ML, while (4) was tested for the thick-island limit of a 3.0 ML oxide. The second group tested represented α-Fe_2O_3(0001) with 2 bilayers of Fe and O (AB stacking of O layers) and 3 bilayers of Fe and O (ABA stacking of O layers). The final group among the tested structures consists of several different structures for Fe_3O_4(111), including a detailed structure reported recently on the basis of a LEED IV analysis using multiple scattering theory [13,14].

The structures tested for Fe_3O_4(111) were the most complex, and we review their geometries here briefly. Fig. 18 shows the general type of structure that finally best fit our data for 3.0 ML oxide on Pt(111): it consists of three bilayers of Fe and O (with ABC stacking of the O layers). In this figure, the surface is shown to be terminated with 1/4 ML of Fe (as measured with respect to O), as suggested by a recent LEED structural analysis [13,14], but we will discuss later on whether adding this terminating layer is necessary to best fit our XPD data. The bottom bilayer is almost the same as the bilayer of FeO(111) discussed in the prior section, but it differs in having 1/4 ML of Fe missing and a shorter vertical interlayer distance z_3 compared to bulk FeO(111). And the middle bilayer is quite different from those of FeO and α-Fe_2O_3(0001) in showing tetrahedral, octahedral, and tetrahedral sites of Fe as we go from the bulk towards the surface. The third bilayer (top bilayer) from the bottom is just a repeat of the bottom bilayer but with a horizontally-translated stacking sequence, with a more pronounced periodic rumpling of oxygen along the rows perpendicular to the plane of the figure, and with vertical spacings z_1 and z_2 that were varied in our analysis to yield best agreement with experiment.

The main features of the prior LEED structure for Fe_3O_4(111) on Pt(111) are [13,14]: one O surface atom in the unit cell (which is not bonded to the topmost Fe atoms) that is moved upward by ~0.4 Å with respect to the remaining three O atoms (which are in turn bonded to the topmost Fe atoms) and O-Fe-O interlayer spacings that are significantly different from bulk Fe_3O_4(111): $z_1 =$ 0.83 Å (1.19 Å for bulk) and $z_2 = 1.42$ Å (1.19 Å for bulk). Other relative Fe and O positions and lateral relaxations present in this structure are discussed in detail in this LEED study [13,14]. Among the $Fe_3O_4(111)$ structural models tested here are two sets of three different structures of $Fe_3O_4(111)$ with and without the topmost 1/4 ML of Fe. The major difference among the three structures in each set is different interlayer spacings in the O-Fe-O layers as indicated below. The three structures with topmost 1/4 ML Fe are characterized by: (1) bulk vertical spacings (z_1 = 1.19 Å, z_2 = 1.19 Å), (3) the full reconstructed structure of the LEED study (z_1 = 0.83 Å, z_2 = 1.42 Å), and (5) a structure modified for better fit to the XPD data (z_1 = 0.83 Å, z_2 = 1.07 Å), with all other surface relaxation parameters as given in the LEED analysis. The remaining structures (2), (4), and (6) tested for $Fe_3O_4(111)$ are the same as (1), (3), and (5) above, respectively, but without the topmost 1/4 ML (i.e., they are O terminated). These latter three structures also do not include the surface O relaxation discussed earlier, since the presence of the topmost 1/4 Fe is thought to be the driving force for such relaxation.

The three different oxide structural models tested all have threefold symmetry and thus lead to threefold-symmetric XPD patterns. Since our experimental XPD data for 3.0 ML show sixfold symmetry for Fe and nearly sixfold symmetry for O, we must assume the existence of two almost equally present domains with a 180° rotation between them, and in comparing with experiment, have thus summed equal populations of these two domains. In fact, these two domains can be thought of as growing from the base monolayer of FeO discussed in the Section 4 as grown in either the favored or unfavored geometry for 1.0 ML.

In deciding which model best fits our data, all the experimental and theoretical XPD patterns are plotted and compared as normalized χ intensities rather than straight intensities, as discussed in Section 4. We have also used several criteria for deciding on the goodness of fit between theory and experiment: visual comparison of diffraction patterns, comparison of directions and anisotropy for various strong forward scattering features, and R-factor calculations over the full hemisphere of experiment and theory [58,59].

We first summarize our experiment/theory comparisons for different structures of FeO(111) and $Fe_2O_3(0001)$. All theoretical XPD patterns appear elsewhere [5b], but those for a few illustrative cases are shown in Fig. 19. In the first group two and five bilayers of FeO(111) with different interlayer spacings and O stacking as described above, do not give good agreement with the experimental patterns. In particular, the theoretical simulations for two bilayers of FeO, which might have been a reasonable description of oxide structures from 1.25 to 1.75 ML, do not explain the additional features in the experimental XPD patterns for these coverages (Fig. 19(a)). Neither does a calculation for five bilayers agree well with the 3.0 ML data (Fig. 19(b)). Thus, we conclude that the internal structure of the islands formed on top of the base layer is different from that of FeO. Poor agreement between experiment and theory was also found in simulations for: two bilayers (AB O stacking) and three bilayers (ABA O stacking) of $Fe_2O_3(0001)$, as shown in Figs. 19(c)-(d).

For the case of Fe_3O_4, the overall fit between experiment and theory is much improved compared to the other two cases of FeO and Fe_2O_3, suggesting that the internal structure of the islands is close to that of Fe_3O_4. Figs. 20 and 21 show two-domain averaged Fe and O XPD data for four Fe_3O_4 structural models tested: the full surface relaxed structure from LEED including a topmost 1/4 ML of Fe in (a), the same structure without the 1/4 ML of Fe in (b), our improved structural model yielding a better fit to the XPD experimental data and including the 1/4 ML of Fe in (c), and the same improved model without the 1/4 ML of Fe in (d) (which yields the overall best fit to experiment). The O XPD patterns are found to be slightly more sensitive to subtle structural changes than those of Fe as far as the peak positions of the strong forward scattering peaks are concerned. For example, the major difference between the LEED structures shown in Figs. 21(a) and 21(b) and the structures derived in this study shown in Figs. 21(c) and 21(d) is the polar angle positions of the six strongest forward scattering peaks: these peaks, which are found at a polar angle of 34° in the experimental O XPD patterns, are shifted by a large amount of about 6° to a polar angle of 40° with the LEED structural parameters. However, R-factor analysis was necessary to finally choose among the rather similar patterns in Figs. 20 or 21, and we show some of these results below.

In order to determine the best structural model for the case of 3.0 ML of iron oxide on Pt(111), we have carried out an R-factor analysis, again summed over the full-hemispherical XPD data for various structural models and using the same five R-factors discussed previously [59]. The results of this analysis are summarized in Figs. 22(a) (for Fe emission) and 22(b) (for O emission), with the cases being listed from left to right in general order of decreasing R-factors. First, we note that all five R-factors generally show the same trends as structures are varied. The Fe R-factors are slightly more sensitive to changes in structure, with somewhat greater negative slopes in going from left to right. Taking these results for Fe and O in their totality, we can first rule out the two Fe_2O_3 (0001) structural models a and b, as these show a much worse fit to the data than the various structures of Fe_3O_4. Among the Fe_3O_4 structures, those with bulk Fe-O-Fe interlayer spacings (1 and 2) also show significantly reduced agreement with experiment, especially for Fe. Now comparing the structural model of a prior LEED I-V study [13,14] and our proposed model, the structures with a topmost 1/4 ML of Fe (3 and 5) have larger values for all five R-factors than the ones without this 1/4 ML of Fe (4 and 6) for both structural models, suggesting an O-terminated structure. Between the structural models of 4 and 6, three out of five R-factors for the case of O emission favor our proposed structure (6), while there is no noticeable difference in the R-factors for Fe emission.

In deciding which structural model best fits our experimental data for a 3.0 ML film of iron oxide on Pt(111), we have also assessed the possible effects of multiple scattering in our theoretical analysis by carrying out simulations of photoelectron diffraction patterns for a test case within both a single scattering cluster (SSC) [56] model and a multiple scattering cluster (MSC) [63] model. The test case considered was the fully relaxed structure for Fe_3O_4 determined by LEED ([13,14] - structure model (3)). Because of the very time consuming nature of the MSC calculations, particularly in view of the many types of emitters involved, only two azimuthal scans instead of full 2π XPD patterns were calculated in multiple scattering, one for Fe emission at a polar angle of 38° and one for O emission at a polar angle of 34°. These are polar angles for which strong forward scattering and other peaks are present, and one might thus expect more pronounced multiple-scattering effects to arise for them. The MSC calculations were done over only one third of the full azimuthal angles to reduce the cluster size, and the final full azimuthal data were obtained by exploiting threefold data folding and then averaging over two domain structures with a 180° rotation between them, as described earlier. These results appear elsewhere [5b]. For both Fe and O, both the SSC and MSC curves well reproduce the positions of the main peaks in the experimental data. However, the MSC results actually give a somewhat worse fit to the experimental data as far as predicting relative peak intensities. It is not clear why MSC does not provide a better description of our data than the less accurate SSC, but it could be due to the presence of structural or vibrational disorder in these thicker iron oxide films (as suggested by the fuzzy LEED spots) and/or the multilayered structure of the oxide film (as seen in the STM image), that tends to reduce or distort any chains of forward scattering atoms and thus also reduce the effects of multiple scattering. It also may be due to vibrational effects beyond those included via Debye-Waller factors, which would tend to wash out the additional fine structure that is typically introduced in MSC predictions [2], but which may not be experimentally observable. In any case, the generally small differences between the two sets of calculations fully justify our analysis in terms of single scattering.

Figs. 23 and 24 now directly compare our experimental data for Fe and O emission from 3.0 ML of oxide with our final best-fit theoretical results (model 6 in Figs. 20 and 21). In these figs., the measured XPD patterns are shown in (a), the theoretical calculations for one of the two threefold domains are shown in (b), the final theoretical calculations based on adding two possible equally-populated domains with 180° rotation between them are shown in (c), and the simple forward scattering directions for the cluster used to calculate the single-domain XPD pattern of (b) are shown in (d) [64]. In Figs. 23(d) and 24(d), each circle represents a possible forward scattering direction in the cluster, with the diameter of each circle being proportional to 1/(distance from a given emitter). The threefold symmetry of the crystal structures implicit in these clusters is evident in Figs. 23(b), 23(d), 24(b), and 24(d), and even before summing over two domains, we see that these calculations well reproduce all of the main peaks (often half of the peaks) as to positions and relative intensities. The positions of these strongest peaks also agree with directions along which several strong forward scattering events are expected, as illustrated in Figs. 23(d) and 24(d). For example, the peaks at the polar angles around 36° (34°) and 62° (56°) are well reproduced for Fe (O) emission. This agreement is better illustrated in Figs. 23(c) and 24(c) with sixfold symmetry, where theory reproduces all of the strong peaks seen in the experimental data, as well as most of the fine structure for both Fe and O emission, including the dark bands in between various peaks. The experimental patterns do not exhibit as much fine structure, and are somewhat smeared out compared to theory, but the STM image in Fig.

15(d) makes it clear that the actual surface consists of many different kinds of emitters in the several layers of islands formed, and it is thus not at all surprising for experiment to show less dramatic XPD structure. In fact, it is remarkable that the agreement between experiment and theory is this good, suggesting that the average oxide surface is well described by our structural model. An at-first-sight negative aspect of the fit between experiment and theory in the Fe data can be seen in certain features at polar angles less than about 16°, for which the 2-domain calculation shows six double bands of intensity and 6 sharp peaks that are not obvious in the experimental data. However, the double bands are in fact suggested in the actual azimuthal scans for these polar angles, but with smaller relative intensities and thus anisotropies than in theory, making them difficult to see in Fig. 23 [5b]. Anisotropies at such low takeoff angles are also expected to be reduced in the experiment due to the multilayered structure of the thick iron oxide films, which will result in effectively smaller grain sizes for these grazing takeoff angles. The six sharp peaks at the edge of the theoretical diffraction pattern we would not expect to see clearly in the experiment for the same reason, and they could also be obscured by surface refraction effects not properly included in the theory. With regard to threefold versus sixfold symmetry, we also note that full 360° azimuthal scans of O and Fe intensities show that O is overall in a threefold symmetric environment (albeit weakly): the anisotropies of the two sets of six peaks in O 1s emission at polar angles of 34 - 38° and 54 - 58° indicate that one set of three in each case has higher peak-minus-background intensities than the other three by about 3 %. By contrast, the data for Fe emission are sixfold symmetric within our experimental error of about 1%. This small deviation from sixfold symmetry we explain as being due to having two domains of oxide structures that are not quite equally populated, with the O forward scattering peaks being somehow more sensitive to this non-equality than those of Fe.

Our final structural model for the predominant species present in a 3.0 ML iron oxide film grown in sequential 1 ML steps on Pt(111) is thus $Fe_3O_4(111)$, as shown in Fig. 18, but without a topmost 1/4 ML of Fe. Although our model in general agrees with that of a prior LEED study of this system [13,14] (e.g. the Fe-O interlayer spacing of $z_1 = 0.83$ Å), it differs in not having the topmost 1/4 ML of Fe, and in yielding an O-Fe interlayer spacing z_2 of 1.07 Å (an inward relaxation compared to the bulk by 0.12 Å or 10 %, compared to the LEED result of an outward relaxation by 0.24 Å or 20 %).

The relaxation that we find is also qualitatively similar to the case of 1 ML FeO/Pt , where an inward relaxation of 0.6 Å or 48 % was found. Although our differences with the LEED structure as to surface termination and Fe-O interlayer separation could be due to the different one-step preparation procedure used for the oxide in our study, it seems reasonable that the local structure near the surface of the oxide film should not be that sensitive to the method of preparation. The thicker oxide layers formed in this LEED study did seem to have better long-range order however, leading to sharper diffraction spots than those seen in Fig. 14. It would thus certainly be of interest to carry out XPD measurements on films prepared by this other procedure.

Finally, we discuss the influence of multilayer oxide growth on the structure of the base layer on which the oxide islands form. Although the base layer of 1 ML of FeO(111) with its superlattice is clearly present in between the oxide islands for coverages between 1.25 and 1.75 ML, where it is seen in all of LEED, STM, and XPD, we cannot unambiguously tell whether the oxide islands form over this base layer without disturbing it, or simply incorporate it into the oxide structure and in the process change its structure and its periodicity. Our results are most consistent with the latter conclusion, however, since the strong diffraction features at polar angles higher than 20° in both Fe and O emission from a 3.0 ML coverage are also found in the XPD data for 1.75 ML, as well as to a large degree also for 1.50 ML. This can be seen by subtracting out the influence of the forward scattering peaks at $\theta = 20^\circ$. These peaks are well explained as being due to the persistence of the base layer without islands on top, and they are not seen for the case of 3.0 ML. If these peaks are subtracted out of the diffraction pattern, we find that both the Fe and O XPD data are almost identical to the corresponding results for 3.0 ML., leading to the final conclusion that the internal atomic structure of the islands is $Fe_3O_4(111)$ with structural parameters very close to those indicated earlier.

6. CONCLUSIONS

The three complementary surface structure probes of LEED, STM, and XPD, have been combined in a single instrument. This system has been utilized to study the structure of thin iron oxide films grown on Pt(111). For coverages from 0.75 ML to 1.0 ML, we conclude that the oxide films show essentially identical short-range atomic structure, even though the long-range order as judged by STM is different for the two, with elongated islands and some empty regions for 0.75 ML, and large atomically-flat regions for 1.0 ML. XPS quantitative analysis, as well as comparisons to standard XPS spectra, show that the Fe:O stoichiometry of these thin oxides is 1:1, and that the Fe $2p_{3/2}$ binding energy also is consistent with FeO. For both 0.75 ML and 1.0 ML coverages, XPD also shows a topmost oxygen layer relaxed significantly inward by 0.6 Å compared to bulk FeO(111) with an interplanar spacing of 1.25 Å. At 1.0 ML coverage, STM and LEED show an oxide superlattice or Moiré pattern with short-range and long-range periodicities of 3.1 Å and 26 Å (in agreement with prior work). We have also shown that the oxygen stacking in the FeO(111) bilayer is dominated by one of two possible orientations with a 180° rotation between them, with this being the first time that this particular feature of the structure has been discussed. It is also necessary to consider interactions with the second-layer Pt atoms to explain the dominance of the favored stacking scheme.

For the growth of thicker layers of iron oxide in coverages from 1.25 ML to 3.0 ML, we have shown that the growth mode is essentially Stranski-Krastanov: iron oxide islands form on top of a 1 ML FeO(111) superlattice whose presence is clearly seen by all three techniques. For iron oxide films of 3.0 ML thickness, the XPS-derived stoichiometry and Fe $2p_{3/2}$ binding energy are found to indicate the presence of Fe_3O_4, and a detailed analysis of the XPD results proves it to be Fe_3O_4(111)-magnetite in two almost equally populated domains with a 180° rotation between them. The optimized structural parameters for this overlayer are similar to those of a previous LEED study [13,14], but differ in the first Fe-O interplanar spacing as well as in not requiring a topmost 1/4 ML of Fe to terminate the surface. Our XPD data for the lower coverages of 1.25-1.75 ML, taken together with the results for ≤ 1 ML, also suggest that oxide islands consisting largely of Fe_3O_4 are present over the full coverage range from 1.25 to 3.0 ML.

These combined LEED, STM, and XPD results thus illustrate the highly complementary nature of these three techniques, and further show that using any one of them by itself can lead to erroneous or partial conclusions. For example, using LEED alone to determine coverages via that for which the

FeO superlattice is most ideal could lead to an error of 25-50%, since the pattern is sharpest for 1.25-1.50 ML. On the other hand, most of the details of the structure of $Fe_3O_4(111)$ in thicker films has been correctly determined by a prior LEED analysis on this system. With STM, it was possible in prior work to propose a fundamentally correct model for the FeO superlattice, but not to determine the nature of its surface termination, interlayer spacing, or oxygen domain orientations. STM is also of course unique in directly sensing changes in surface topography, short-range order, and long-range order. XPS and XPD as element-specific probes of composition, chemical state, and short-range-order structure thus complement these two techniques beautifully. Future epitaxial and nanostructure growth studies should thus benefit by the *in situ* combination of these three techniques.

ACKNOWLEDGEMENTS

We are indebted to A.P Kaduwela for assistance with many aspects of the theoretical analysis of this data, and to H. Xiao for the writing of a computer program that controlled the photoelectron spectrometer used in this study. We are also grateful to B. Petersen for the loan of the Pt(111) crystal used in this work. The financial support of the Director, Office of Energy Research, Office of Basic Energy Sciences, Materials Sciences Division of the U.S. Department of Energy under Contract No. DE-AC03-76SF00098 and of the Office of Naval Research under Contract N00014-94-0162 is also gratefully acknowledged.

Table 1. Fe coverages before oxidation as determined by both QCM and XPS, and Fe-O stoichiometries after oxidation as determined by XPS.

Fe (ML) by QCM Before Oxidation	Fe(ML) by XPS Before Oxidation	Fe:O Stoichiometry by XPS After Oxidation
0.75	0.67	1 : 1.07
1.00	0.93	1 : 1.08
1.25	1.25	1 : 1.12
1.50	1.62	1 : 1.16
1.75	1.82	1 : 1.25
3.00	3.64	1 : 1.39

REFERENCES

[1] Excellent summaries of the current status of most of these techniques can be found in the proceedings of three previous International Conferences on Structure of Surfaces: (a) The Structure of Surfaces I, Eds. M.A. Van Hove and S.Y. Tong (Springer Verlag, Berlin, 1985); (b) The Structure of Surfaces II, Eds. J.F. van der Veen and M.A. Van Hove (Springer Verlag, Berlin, 1988); (c) The Structure of Surfaces III, Eds. S.Y. Tong, M.A. Van Hove, K. Takayanagi, and X.D. Xie (Springer-Verlag, Berlin, 1991); (d) The Structure of Surfaces IV, Eds. X.D. Xie, K. Takayanagi, S.Y. Tong, and M.A. Van Hove (World Sci., Singapore, 1994).

[2] C.S. Fadley in Synchrotron Radiation Research: Advances in Surface Science, Ed. R.Z. Bachrach (Plenum, New York, 1992); C.S. Fadley, Surf. Sci. Repts.19 (1993) 231; C.S. Fadley, S. Thevuthasan, A.P. Kaduwela, C. Westphal, Y.J. Kim, R. Ynzunza, P. Len, E. Tober, F. Zheng, Z. Wang, S. Ruebush, A. Budge, and M.A. Van Hove, J. Electron Spectrosc. and Relat. Phenom. 68 (1994) 19.

[3] G. Binnig and H. Rohrer, Rev. Mod. Phys. 59 (1987) 615; F. Ogletree and M. Salmeron, Prog. Solid St. Chem. 20 (1990) 235.

[4] (a) J.B. Pendry, Low Energy Electron Diffraction (Academic Press, New York, 1974); (b) M.A. Van Hove, W.H. Weinberg and, C.-M. Chan, Low Energy Electron Diffraction (Springer-Verlag, Heidelberg, 1986).

[5] (a) Y.J. Kim, C. Westphal, R.X. Ynzunza, H.C. Galloway, M.B. Salmeron, M.A. Van Hove, and C.S. Fadley, Phys. Rev. B, 55, R13448 (1997); (b) Y.J. Kim, Ph. D. Dissertation, Department of Chemistry, University of Hawaii, 1995

[6] V.E. Henrich and P.A. Cox, The Surface Science of Metal Oxides (Cambridge University Press, Cambridge, 1994); C. Noguera, Physics and Chemistry of Oxide Surfaces (Cambridge University Press, New York, 1996).

[7] V. Maurice, M. Salmeron, and G.A. Somorjai, Surf. Sci. 237 (1990) 116.

[8] M.C. Wu, J.S. Corneille, C.A. Estrada, J.W. He, and D.W. Goodman, Chem. Phys. Lett. 182 (1991) 472.

[9] G.H. Vurens, M. Salmeron, and G.A. Somorjai, Surf. Sci. 201 (1988) 129.

[10] G.H. Vurens, V. Maurice, M. Salmeron, and G.A. Somorjai, Surf. Sci. 268 (1992) 170.

[11] H.C. Galloway, J.J. Benitez, and M. Salmeron, Surf. Sci. 198 (1993) 127.

[12] H.C. Galloway, J.J. Benitez, and M. Salmeron, J. Vac. Sci. Technol. A12 (1994) 2302.

[13] W. Weiss, A. Barbieri, M.A. Van Hove, and G.A. Somorjai, Phys. Rev. Lett. 71 (1993) 1884.

[14] A. Barbieri, W. Weiss, M.A. Van Hove, and G.A. Somorjai, Surf. Sci. 302 (1994) 259.

[15] T. Schedel-Niedrig, W.Weiss, and R. Schlögl, Phys. Rev. B 52 (1995) 17449

[16] S.J. Tauster, Acc. Chem. Res. 20 (1987) 389.

[17] G.L. Haller and D.E. Resasco, Adv. Catal. 36 (1989) 173.

[18] K.J. Williams, A.B. Boffa, J. Lahtinen, M. Salmeron, A.T. Bell, and G.A. Somorjai, Catal. Lett. 5 (1990) 385.

[19] H.C. Wang, D.F. Ogletree, and M. Salmeron, J. Vac. Sci. Technol. 9 (1991) 853.

[20] M.J. Bennett, in High Temperature Corrosion, Ed. R.A. Rapp (NACE, Houston, TX, 1983) p.145.

[21] (a) S. Yoshii, O. Ishii, S. Hittori, T. Nakagawa, and G. Ishida, J. Appl. Phys. 53 (1982) 2556; (b) E. Kay, R.A. Sigsbee, G.L. Bona, M. Taborelli, and H.C. Siegmann, Appl. Phys. Lett. 47 (1985) 533; (c) S.S.P. Parkin, R. Sigsbee, R. Felici, and G.P. Felcher, Appl. Phys. Lett. 48 (1986) 604; (d) A. Aeschlimann, G.L. Bona, F. Meier, M. Stampanoni, G. Zampieri, and H.C. Siegmann, Appl. Phys. Lett. 49 (1986) 824.

[22] J.C. Phillips, Physics of High-T_C Superconductors (Academic Press, New York, 1989).

[23] R.G. Wyckoff, Crystal Structures (Interscience, New York, 1963).

[24] A. Muan, Am. J. Sci. 256 (1958) 171; T.B. Massalski, J.L. Murray, L.H. Bennet, and H. Baker, Binary Alloy Phase Diagrams (American Society for Metals, Metals Park, OH, 1986) p. 1807.

[25] D. Alder, in Solid State Physics, Eds. H. Ehrenreich, F. Seitz, and D. Turnbull, Vol. 21 (Academic, New York, 1968); A. Chainani, T. Yokoya, T. Morimoto, T. Takahashi, and S. Todo, Phys. Rev. B 51, 17976 (1995), and papers therein.

[26] C.R. Brundle, T.J. Chuang, and K. Wandelt, Surf. Sci. 68 (1977) 459.

[27] M. Muhler, R. Schlogl, and G. Ertl, J. Catal. 126 (1990) 339.

[28] R.J. Lad and V.E. Henrich, Surf. Sci. 193 (1988) 81.

[29] R.L. Kurtz and V.E. Henrich, Surf. Sci. 129 (1983) 345.

[30] N.G. Condon, F.M. Leibsle, A.R. Lennie, P.W. Murray, D.J. Vaughan, and G. Thornton, Phys. Rev. Lett. 75 (1995) 1961

[31] N.G. Condon, P.W. Murray, F.M. Leibsle, G. Thornton, A.R. Lennie, and D.J. Vaughan, (a) Surf. Sci. 310 (1994) L609; and (b) private communication, to appear.

[32] G. Tarrach, D. Bürgler, T. Schaub, R. Wiesendanger, and H.-J. Güntherodt, Surf. Sci. 285 (1993) 1.

[33] A. Zangwill, Physics at Surfaces (Cambridge University Press, Cambridge, 1988).

[34] R.C. White, C.S. Fadley, R. Trehan, J. Electron Spectrosc. Relat. Phenom. 41 (1986) 95

[35] J. Osterwalder, M. Sagurton, P.J. Orders, C.S. Fadley, B.D. Hermsmeier, and D.J. Friedman, J. Electron Spectrosc. Relat. Phenom. 48 (1989) 55.

[36] H. Xiao, unpublished software for accumulating XPD data.

[37] L.G. Petersson, S. Kono, N.F.T. Hall, C.S. Fadley, and J.B. Pendry, Phys. Rev. Lett. 42 (1979) 1545.

[38] H.C. Poon and S.Y. Tong, Phys. Rev. B30 (1984) 6621; S.Y. Tong, H.C. Poon, and D.R. Snider, Phys. Rev. B32 (1985) 2096.

[39] W.F. Egelhoff, Phys. Rev. B30 (1984) 1052; E.L. Bullock and C.S. Fadley, Phys. Rev. B31 (1985) 1212; W.F. Egelhoff, Phys. Rev. Lett. 59 (1987) 559.

[40] Sagurton, E.L. Bullock, and C.S. Fadley, Phys. Rev. B30 (1984) 7332.

[41] J. Osterwalder, T. Greber, A. Stuck, and L. Schlapbach, Phys. Rev. B44 (1991) 13764.

[42] W.A. Fraser, J.V. Florio, W.N. Delgass, and W.D. Robertson, Surf. Sci. 36 (1973) 661.

[43] C.S. Fadley, Prog. Surf. Sci. 16 (1984) 275.

[44] C.S. Fadley in Electron Spectroscopy: Theory, Techniques, and Applications, Eds. C.R. Brundle and A.D. Baker, Vol. II, Chap.1 (Academic Press, London, 1978).

[45] R.E. Connelly, C.S. Fadley, and J. Orders, J. Vac. Sci. Technol. A2 (1984) 1333.

[46] P. Alnot, J. Olivier, and C.S. Fadley, J. Electron Spectrosc. Relat. Phenom. 49 (1989) 159.

[47] C.R. Brundle, T.J. Chuang, and K. Wandelt, Surf. Sci. 68 (1977) 459.

[48] T.J. Chuang, C.R. Brundle, and D.W. Rice, Surf. Sci. 59 (1976) 413.

[49] K. Asami, K. Hashimoto, and S. Shimodaira, Corrosion Sci. 16 (1976) 35.

[50] C.R. Brundle and A.F. Carley, Chem. Phys. Lett. 31 (1975) 423.

[51] H.K. Bowen, D. Adler, and B.H. Auker, J. Solid State Chem. 12 (1975) 355.

[52] P. Dierckx, J. Comput. Appl. Math. 1 (1975) 165, and program written by S. Ruebush to apply this method to spline fitting XPD data.

[53] R.J. Baird, C.S. Fadley, and L.F. Wagner, Phys. Rev. B15 (1977) 666; J. Osterwalder, T. Greber, A. Stuck, and L. Schlapbach, Phys. Rev. B44 (1991) 13764.

[54] S.M. Goldberg, R.J. Baird, S. Kono, N.F.T. Hall, and C.S. Fadley, J. Electron Spectrosc. 21 (1980) 1; R. Trehan, J. Osterwalder, and C.S. Fadley, J. Electron Spectrosc. Relat. Phenom. 42 (1987) 187.

[55] N. Naumovic, A. Stuck, T. Greber, J. Osterwalder, and L. Schlapbach, Phys. Rev. B47 (1993) 7462.

[56] D.J. Friedman and C.S. Fadley, J. Electron Spectrosc. Relat. Phenom. 51 (1990) 689.

[57] M. Sagurton, E.L. Bullock, C.S. Fadley, Surf. Sci. 182 (1987) 287.

[58] M.A. Van Hove, S.Y. Tong, and M.H. Elconin, Surf. Sci. 64 (1977) 85.

[59] R.S. Saiki, A.P. Kaduwela, M. Sagurton, J. Osterwalder, D.J. Friedman, C.S. Fadley, and C.R. Brundle, Surf. Sci. 282 (1993) 33; S.D. Ruebush, R.E. Couch, S. Thevuthasan, C.S. Fadley, Surface Science, manuscript no. 98056, to appear; R.X Ynzunza et al., unpublished results.

[60] H.C. Galloway, P. Sautet, and M. Salmeron, Phys. Rev. B54 (1996) 11145.

[61] V.S. Smentkowski and J.T. Yates, Jr., Surf. Sci. 232 (1990) 113; and references therein.

[62] D.P. Woodruff and T.A. Delchar, Modern Techniques of Surface Science (Cambridge University Press, Cambridge, 1986).

[63] A.P. Kaduwela, D.J. Friedman, and C.S. Fadley, J. Electron Spectrosc. and Relat. Phenom. 57 (1991) 223.

[64] R.X. Ynzunza, program for calculating forward scattering patterns described in Ph.D. Dissertation, Department of Physics, University of California, Davis, 1998.

feoxpap6.rev

FIGURE CAPTIONS

Figure 1. Atomic structures of three different iron oxide surfaces, with (111) termination for FeO and Fe_3O_4 and (1000) termination for α-Fe_2O_3. One oxygen layer (large open circles) and iron layers on both sides of it (light grey above, and dark grey below) are shown for each surface. The lateral periodicities are indicated by the different two-dimensional unit cells.

Figure 2. (a) Structural model for the bilayer of FeO(111) on Pt(111) first proposed in ref. [11]. Only a portion of the oxygen atoms in the top layer are shown for clarity. The oxygen termination of the surface was suggested in this prior study, but could not be experimentally verified. The 0.6° rotational mismatch between the overlayer and the Pt substrate in turn leads to a 5.2° mismatch between the lateral superlattice and the substrate; these rotations can occur in both a clockwise and an counterclockwise sense. (b) Expanded view of the lateral superlattice formed by the structure in (a), with only the Fe and Pt atoms being shown. The resulting Moiré pattern is responsible for the satellite spots in the LEED patterns from this structure.

Figure 3. The experimental system combining XPS, XPD, LEED, and STM that was constructed as part of this study [5]. (a) Overall view showing the principal elements. At left are stepping motors providing computer control of both azimuthal (ϕ) and polar (θ) angles. A VG ESCALAB5 spectrometer with various special modifications [34,35] is in the center, and a LEED/STM/preparation chamber with metal deposition facilities is at right. (b) Closeup of the two-axis variable-temperature specimen goniometer. The sample with its heater, drive gear, and base can be removed *in situ* by loosening the two cap screws at far right. (c) The specimen transfer area in the LEED/STM chamber, with the STM at top, the wobble stick in the process of moving the sample, and an optional set of reference samples at bottom.

Figure 4. The basic experimental geometry in the XPD experiment. The polar takeoff angle θ is measured from the surface. The angle α between the incoming radiation and the outgoing wave vector was fixed at 48°.

Figure 5. Fe $2p_{3/2}$ XPS spectra obtained for iron oxide coverages from 1.0 ML to 3.0 ML. Al Kα (1486.7 eV) was used for excitation. Note the movement of the binding energy toward higher values as coverage increases.

Figure 6. (a),(b) : LEED patterns taken at 54 eV incident energy for (a) 0.75 ML and (b) 1.0 ML of FeO on Pt(111). These patterns are almost identical for both coverages, implying almost the same long-range atomic geometries for both films. Each one shows a three-fold symmetric pattern where each of the six principal "hexagonal" spots is surrounded by a rosette of six satellite spots. Note the blurring of the inner spots of each rosette. (c)-(e): Model single scattering calculations of the LEED patterns expected from different domain sizes of the structure in Fig. 2. (c) A large domain of 200 Å diameter, (d) a rectangular domain of 200 Å by 52 Å to simulate elongated island (columnar) growth, (e) a small domain of 60 Å diameter as a limiting case of short-range order.

Figure 7. Large-area STM images taken in constant current mode for both 0.75 ML and 1.0 ML FeO/Pt(111): (a) A 320 nm x 320 nm image taken for 0.75 ML FeO shows empty regions comprising about 25 % of the total area, and elongated islands or columns of oxide growing outward from two diagonally-oriented monatomic steps. The current is 2.0 nA and the sample bias voltage is 200 mV. (b) An 800 nm x 800 nm image taken for 1.0 ML FeO shows atomically-smooth terraces across two vertically-oriented monatomic steps with no more evidence of the elongated islands. The current is 2.46 nA and the sample bias voltage is 460 mV.

Figure 8. STM images for 1.0 ML FeO/Pt(111): (a) A 5.8 nm x 5.8 nm image taken in constant height mode and showing a hexagonal atomic periodicity of 0.31 nm = 3.1 Å that is further modulated with the larger periodicity of 2.6 nm = 26 Å. The average current is 1.36 nA and the sample bias voltage is 453 mV. (b) A 79.2 nm x 79.2 nm image taken in constant height mode and showing the

extended (and faulted) periodicity of the large unit cell (~26 Å). The lines separate domains of two possible rotational orientations (cf. Fig. 2). The average current is 2.5 nA and the sample bias voltage is 436 mV.

Figure 9. Stereographic projections of full 2π XPD χ patterns for Pt 4f, Fe $2p_{3/2}$, and O 1s emission from (a) 0.75 ML and (b) 1.0 ML of FeO on Pt(111). The nearly identical XPD patterns for both coverages imply that both oxides have the same short-range atomic geometries. Al Kα radiation (1486.7 eV) was used for excitation.

Figure 10. Two views of the atomic cluster used to theoretically model XPD data for 1.0 ML FeO/Pt(111). The topmost O layer is finally found to be relaxed inward by 0.57 Å compared to bulk FeO(111) to yield the forward scattering peak positions found for Fe in Fig. 9, and the FeO(111) bilayer to have a lateral hexagonal periodicity of 3.1 Å. The Pt atoms were not considered as scatterers in the XPD calculations due to the dominance of forward scattering.

Figure 11. Experimental and theoretical 2π XPD χ patterns for Fe $2p_{3/2}$ emission from 1.0 ML FeO/Pt(111), again in stereographic projection: (a) experimental data, (b) theoretical calculation using the cluster of Fig. 10 with an Fe-O bilayer spacing of 0.68 Å, (c) theoretical calculation using the cluster of Fig. 10 with a bilayer spacing of 1.25 Å such as that in bulk FeO. In (d), the results of an R-factor comparison of experiment with theory for different Fe-O bilayer spacings is shown. The definitions of R1, R2, R3, R4, and R5 appear in ref. 59, and the % changes in them over this spacing range are given in parentheses.

Figure 12. Experimental and theoretical 2π XPD χ patterns for O 1s emission from 1.0 ML FeO/Pt(111), again in stereographic projection: (a) experimental data, (b) theoretical calculation using the cluster of Fig. 10 with an Fe-O bilayer spacing of 0.68 Å.

Figure 13. Two different FeO(111) bilayer structural models linked to the two different possibilities for stacking O with respect to Fe and Pt(111). As viewed from a typical Fe atom, the nearest-

neighbor O trimers sit along Pt $<11\bar{2}>$ directions in (a), and are rotated by 180° in (b). Near the lower left corners of the large unit cells shown (see enlargements), the Fe atoms are directly above first-layer Pt atoms, but in (a) the O atoms do not sit above first- or second-layer Pt atoms, whereas in (b), they sit above second-layer Pt atoms. In the absence of second-layer Pt atoms, region "1" is equivalent to region "2" if the structure in (b) is rotated by 180°.

Figure 14. LEED patterns at a 53.5 eV incident energy for different iron oxide coverages from 1.25 ML to 3.0 ML. The fine structure due to the 1 ML FeO Moiré superlattice (cf. Fig. 6) persists and in fact sharpens through 1.75 ML, but has disappeared by 3.0 ML.

Figure 15. STM images taken in constant-current mode for the same surfaces and iron oxide coverages considered in Fig. 14: (a) 1.25 ML-- This 264 nm x 264 nm image shows preferential growth of small islands (~5 nm diameter) near a step edge. The current was 2.9 nA and the sample bias voltage was 460 mV. (b) 1.50 ML-- This 400 nm x 400 nm image shows a mix of small and large islands (up to ~25 nm diameter) growing on top of a flat base layer. The current was 2.2 nA and the sample bias voltage was 460 mV. (c) 1.75 ML-- This 800 x 800 nm image shows a higher coverage by islands compared to 1.50 ML, and shapes indicating extensive coalescence. The current was 3.0 nA and the sample bias voltage was 460 mV. (d) 3.0 ML-- This 460 x 460 nm image shows mulitlayer growth terminating in smaller topmost island sizes as compared to the lower coverages. The base layer is not clearly visible at this coverage. The current was 3.0 nA and the sample bias voltage was 460 mV.

Figure 16. A 22 x 22 nm constant-height STM image of a 1.75 ML iron oxide layer on Pt(111). Oxide islands (top half of image) form on top of a superlattice of 1 ML FeO/Pt(111) with 26 Å periodicity (lower half of image). The average current was 2.22 nA and the sample bias voltage was 460 mV.

Figure 17. Full-2π XPD χ patterns in stereographic projection for the same surfaces and iron oxide coverages as Figs. 14 and 15: (a) Pt 4f, (b) Fe $2p_{3/2}$, and (c) O 1s. Al Kα (1486.7 eV) was used for excitation.

Figure 18. The atomic cluster used to model XPD from a 3.0 ML coverage of $Fe_3O_4(111)$. The surface is shown here terminated with 1/4 ML of Fe, but calculations have been performed with and without this termination. Note the vertical relaxation of one O atom compared to the remaining three O atoms within the unit cell, as well as possible relaxations in the Fe-O interlayer spacings (z_1, z_2, and z_3).

Figure 19. Theoretical Fe $2p_{3/2}$ (left panel) and O 1s (right panel) XPD χ patterns for four different structural models of FeO and Fe_2O_3 tested, in stereographic projection. (a) two bilayers of Fe and O in the FeO(111) configuration, with the bottom bilayer relaxed as for 1 ML FeO/Pt(111) (structure model 2). (b) five bilayers of FeO(111) (model 5). (c) two bilayers of $Fe_2O_3(0001)$. (d) three bilayers of $Fe_2O_3(0001)$.

Figure 20. Theoretical Fe $2p_{3/2}$ XPD χ patterns for four different structural models of $Fe_3O_4(111)$ tested, again in stereographic projection. Calculations for the fully relaxed structure determined in a recent LEED study (model 3: $z_1 = 0.83$ Å, $z_2 = 1.42$ Å, $z_3 = 1.19$ Å) are shown in (a) with a topmost 1/4 ML of Fe terminating the surface and in (b) without this terminating Fe (model 4). Calculations for our optimized structural model ($z_1 = 0.83$ Å, $z_2 = 1.07$ Å, $z_3 = 1.19$ Å) are shown in (c) with the topmost 1.4 ML of Fe (model 5), and in (d) without this terminating Fe (model 6).

Figure 21. As Fig. 20, but for O 1s emission.

Figure 22. R-factor analysis of different structures, as judged against experiment for 3.0 ML of iron oxide on Pt(111), and summed over the entire 2π data set: (a) Fe $2p_{3/2}$ emission, and (b) O 1s emission. The 8 structural models considered (see text for details) are in approximate order of decreasing R-factor.

Figure 23 (a)-(c): Full-2π XPD χ patterns for Fe $2p_{3/2}$ emission from 3.0 ML iron oxide on Pt(111), again in stereographic projection, are compared to theoretical simulations for our optimized model for $Fe_3O_4(111)$-- (a) experimental data, (b) single-domain calculation, (c) two-domain calculation involving the sum of (b) and a similar pattern rotated by 180°. (d): Illustration of the various forward scattering events possible in the single-domain cluster utilized, with circle size being inversely proportional to distance from a given emitter. The cluster used was based on the geometry of Fig. 18, but without the topmost 1/4 ML of Fe, and with $z_1 = 0.83$ Å, $z_2 = 1.07$ Å, and $z_3 = 1.19$ Å.

Figure 24. As Fig. 23, but for O 1s emission.

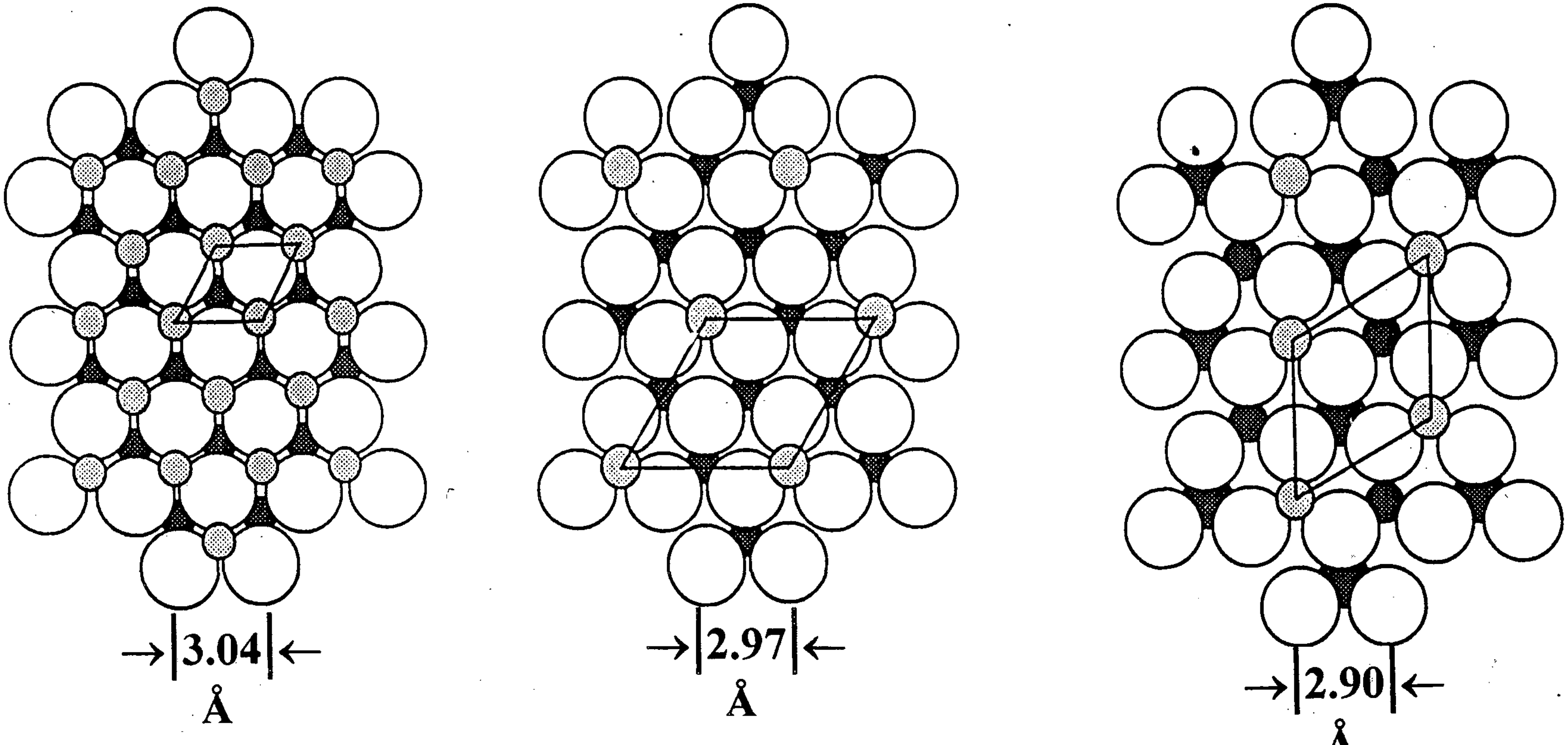

Fe O

Fe_3O_4

α-Fe_2O_3

Figure 1

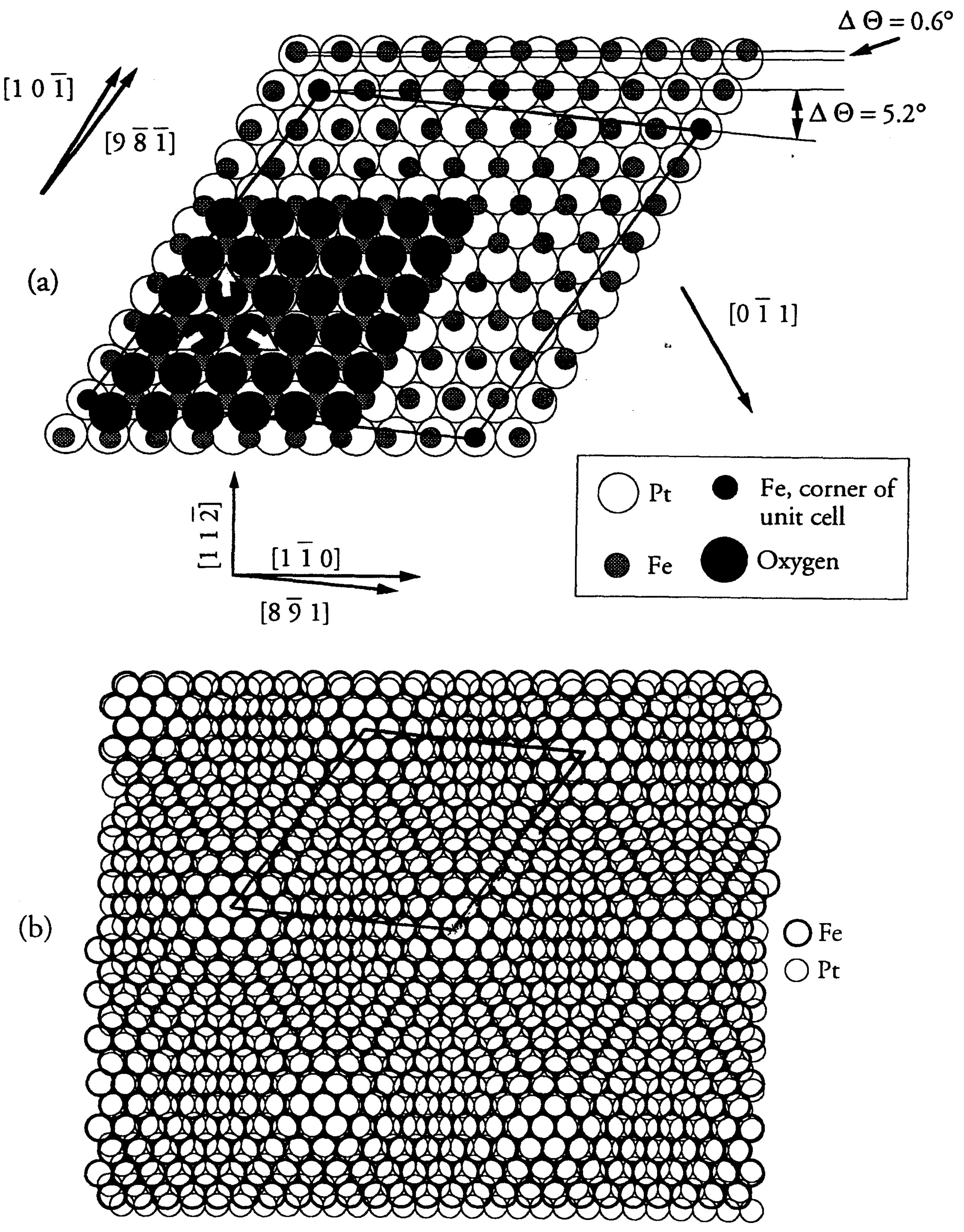

$\Delta\Theta = 0.6°$
$\Delta\Theta = 5.2°$
$[1\,0\,\bar{1}]$
$[9\,\bar{8}\,\bar{1}]$
(a)
$[0\,\bar{1}\,1]$
$[1\,1\,\bar{2}]$
$[1\,\bar{1}\,0]$
$[8\,\bar{9}\,1]$
Pt
Fe, corner of unit cell
Fe
Oxygen
(b)
Fe
Pt

Figure 2

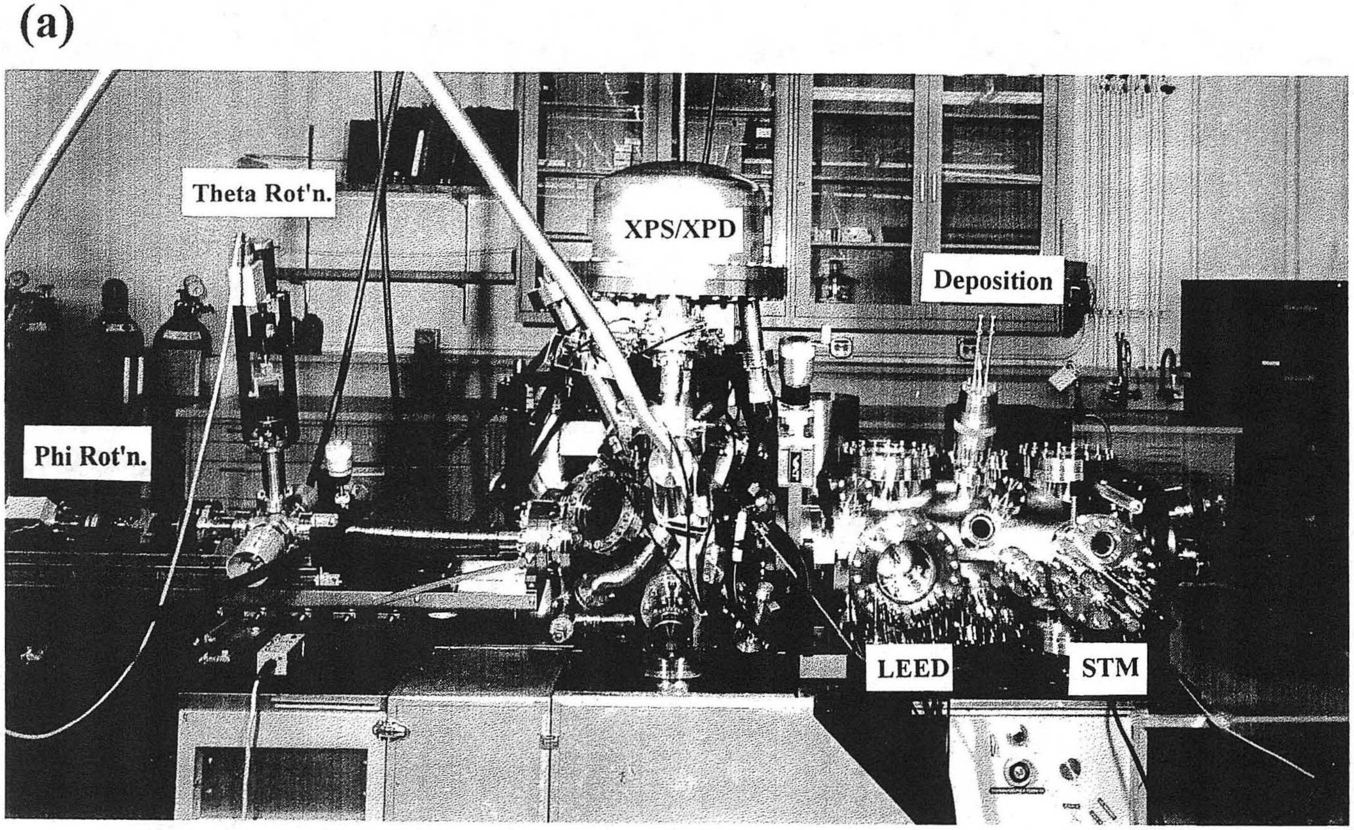

Figure 3(a)

(b)

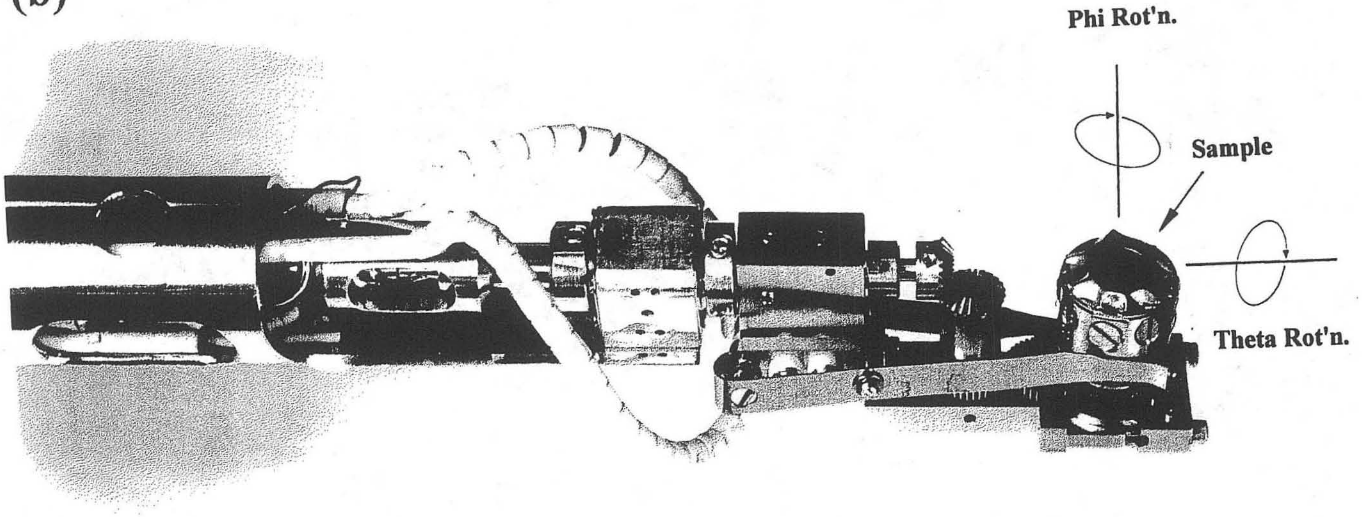

Figure 3(b)

(c)

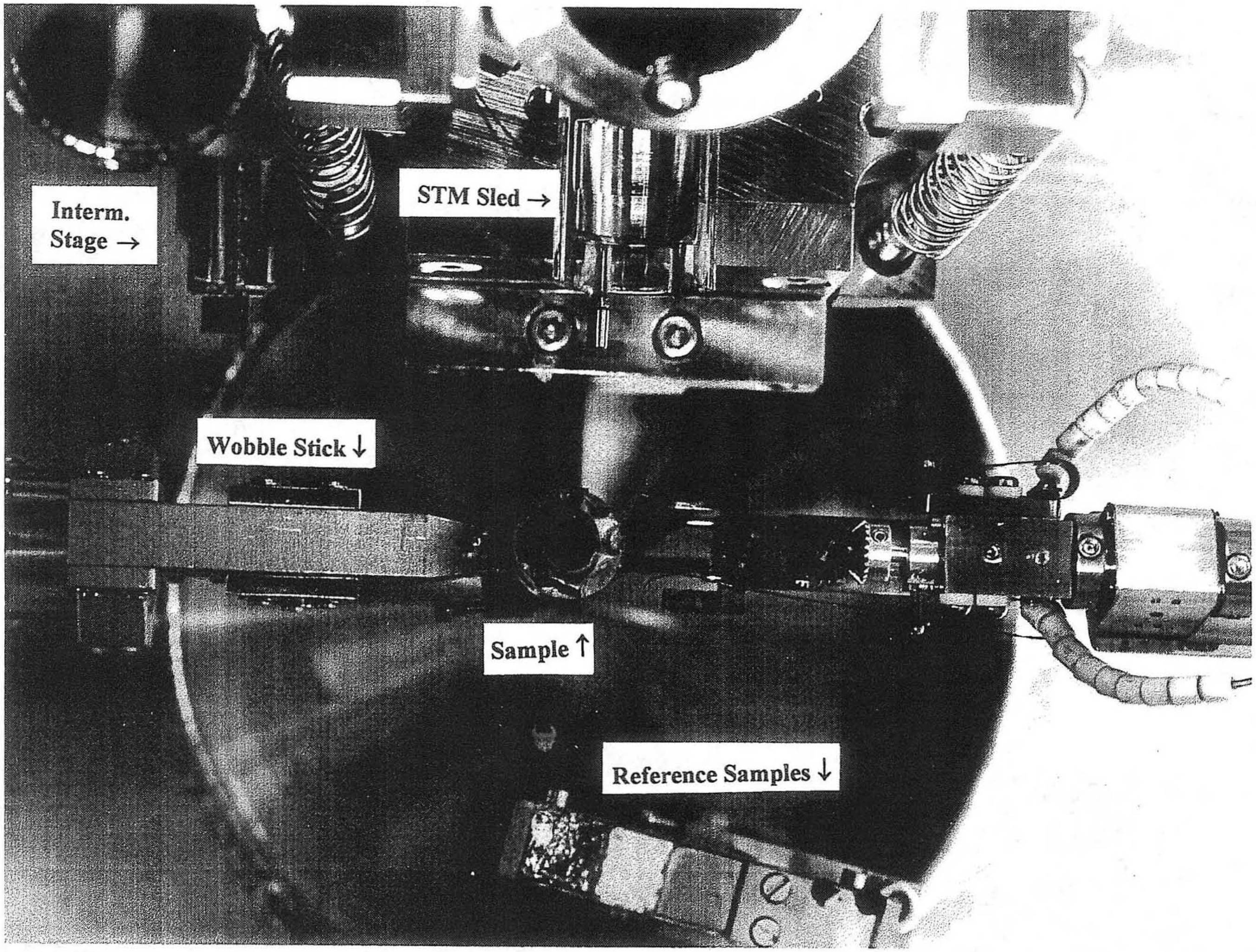
Interm. Stage →
STM Sled →
Wobble Stick ↓
Sample ↑
Reference Samples ↓

Figure 3(c)

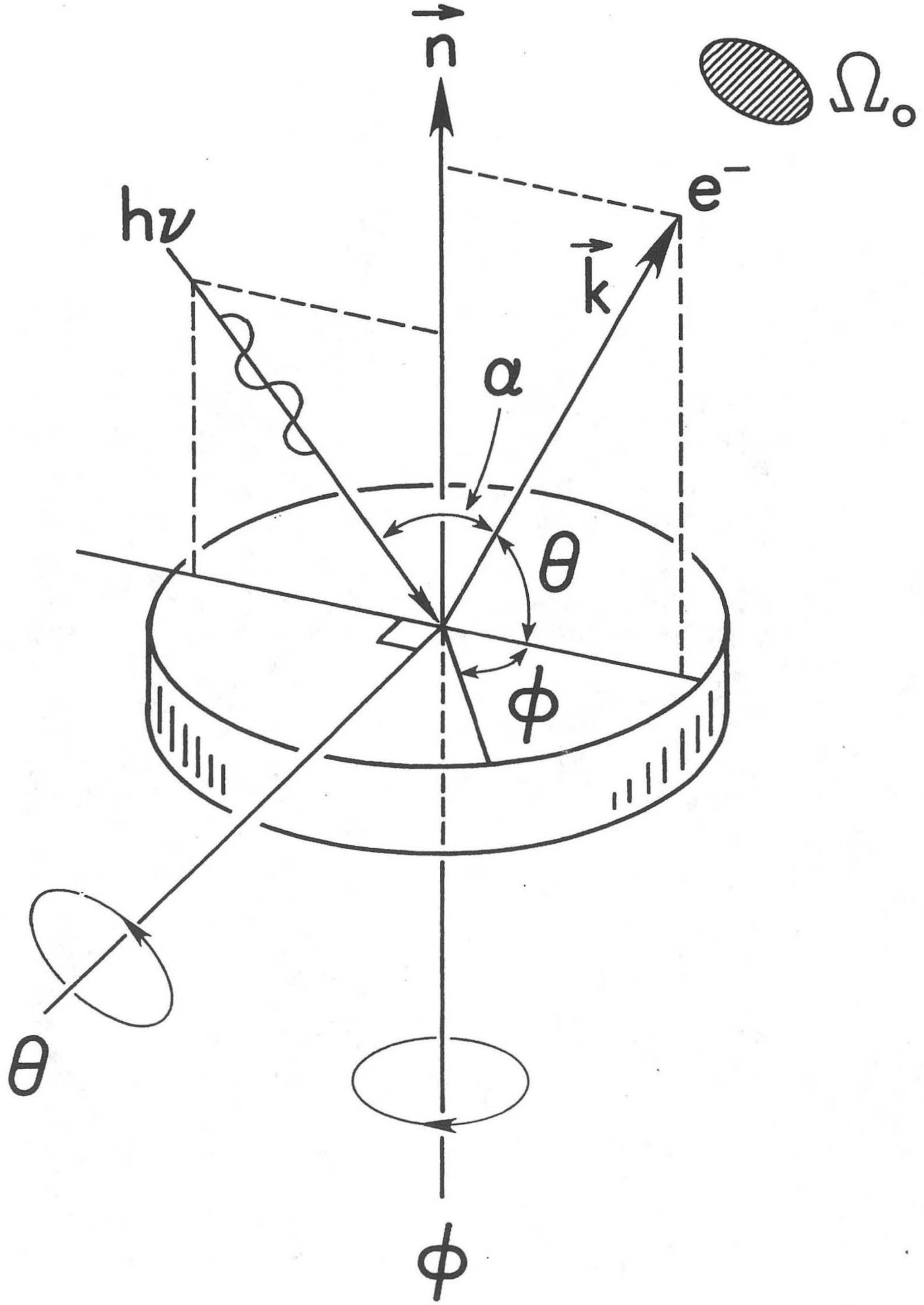

Figure 4

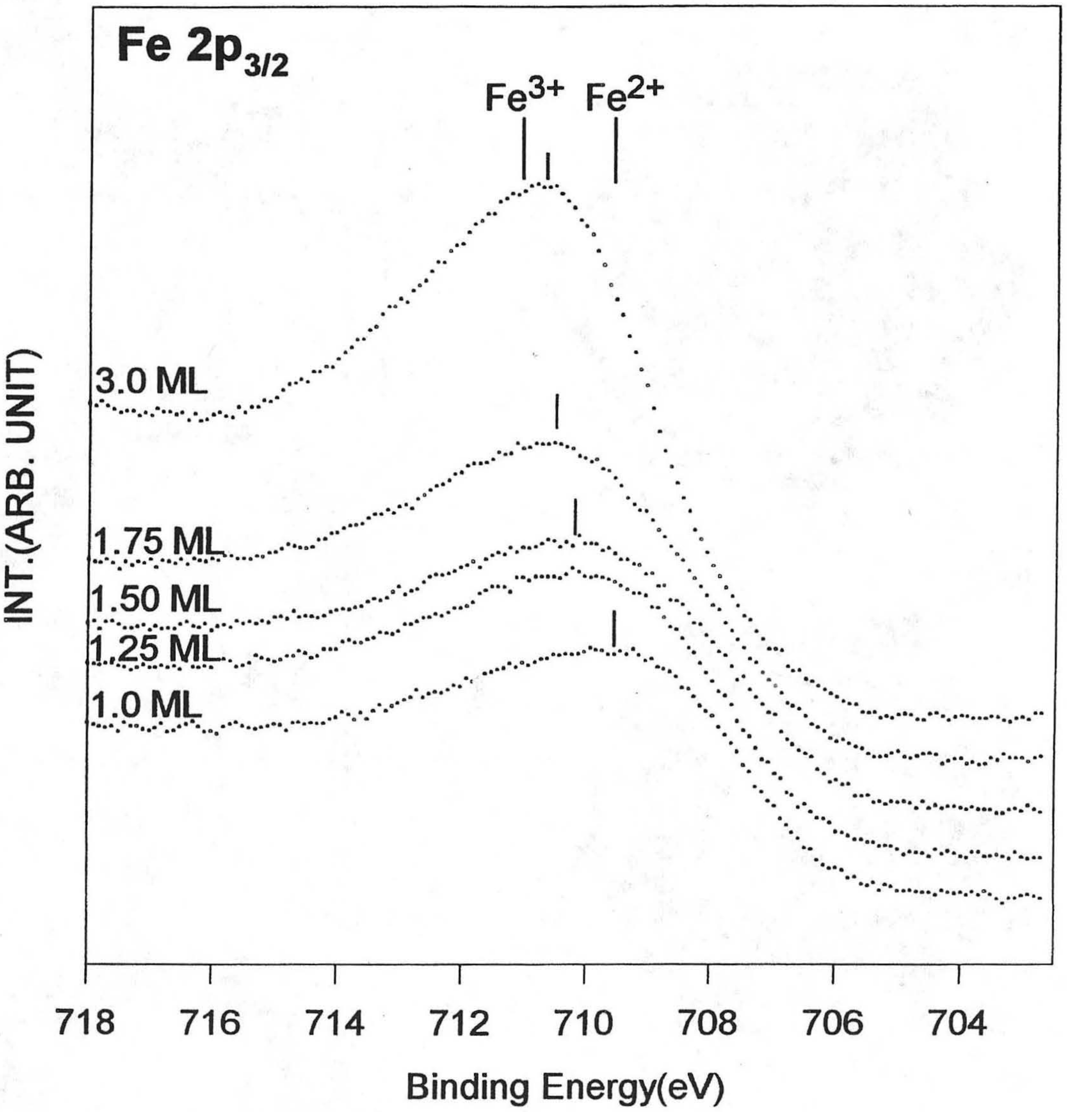

XBD9701-00022.TIF

Figure 5

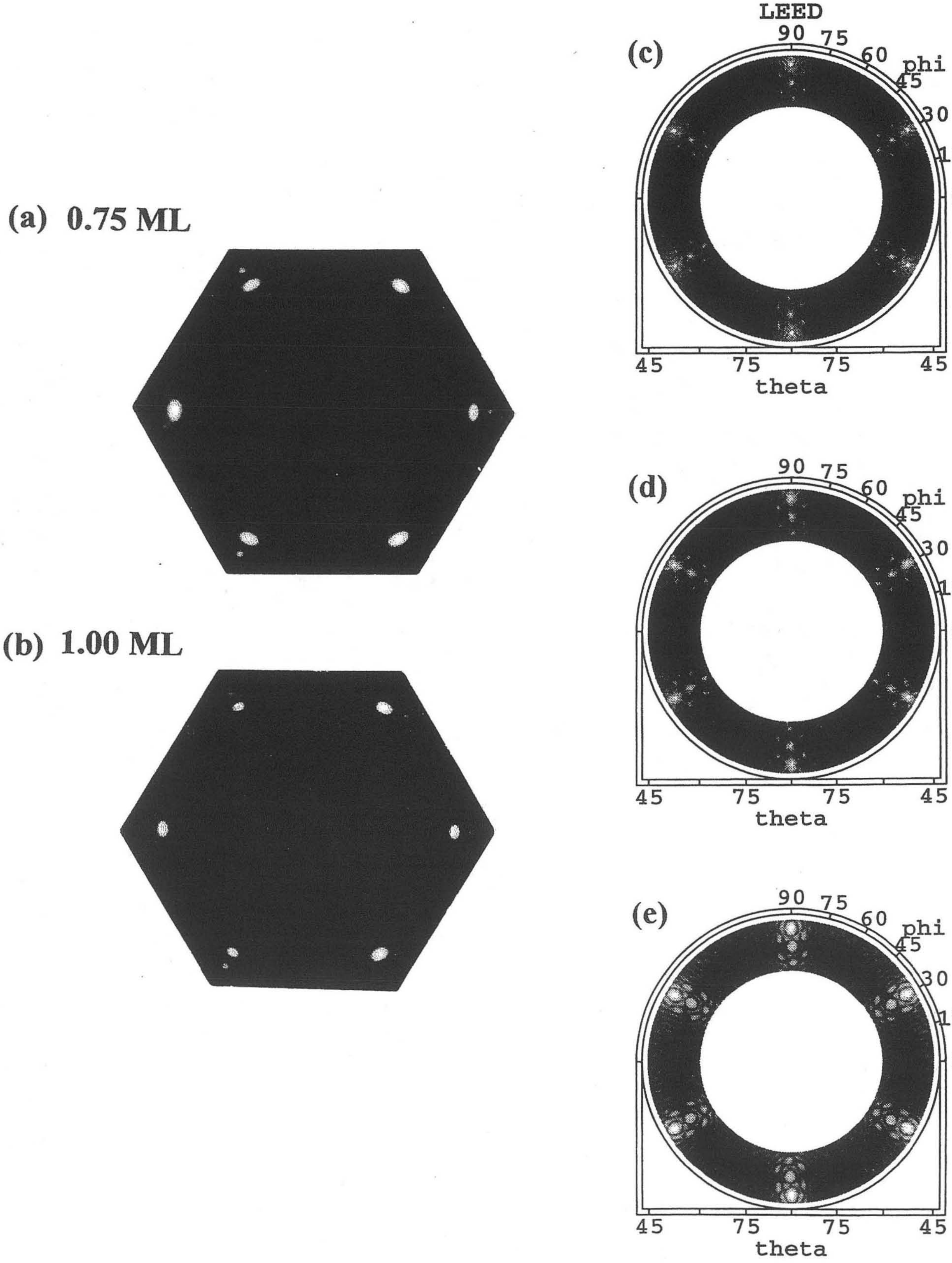

Figure 6

(a) 0.75 ML

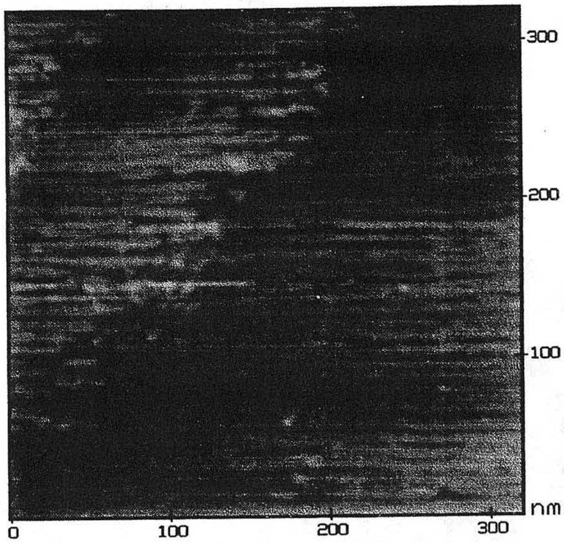

(b) 1.00 ML

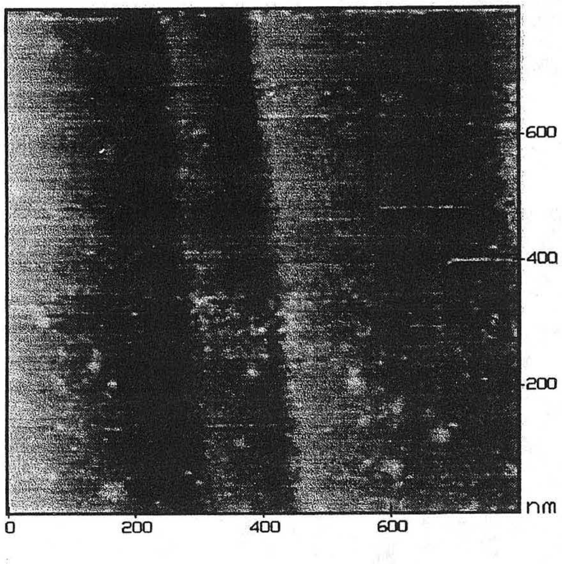

Figure 7

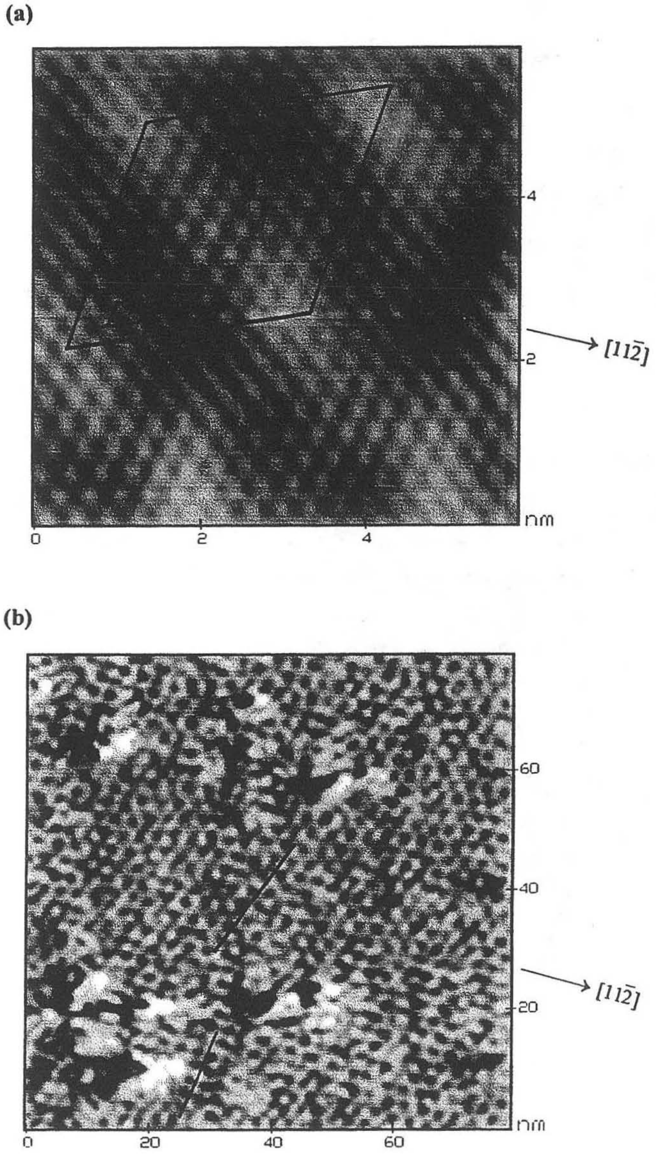

Figure 8

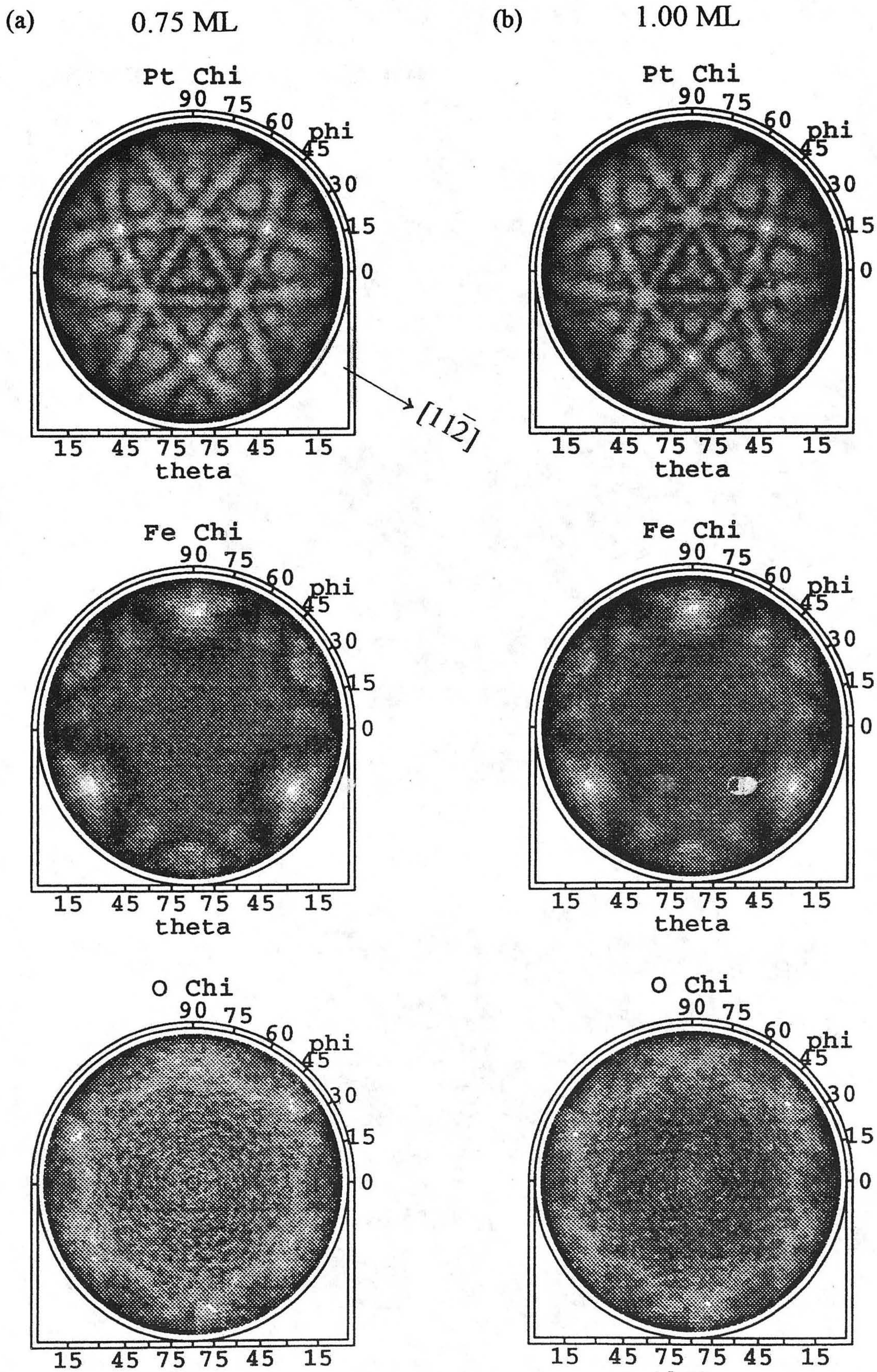
(a)
0.75 ML
(b)
1.00 ML
Pt Chi
Fe Chi
O Chi
phi
90
75
60
45
30
15
0
theta
15
45
75
75
45
15
[11$\bar{2}$]

Figure 9

FeO/Pt(111)

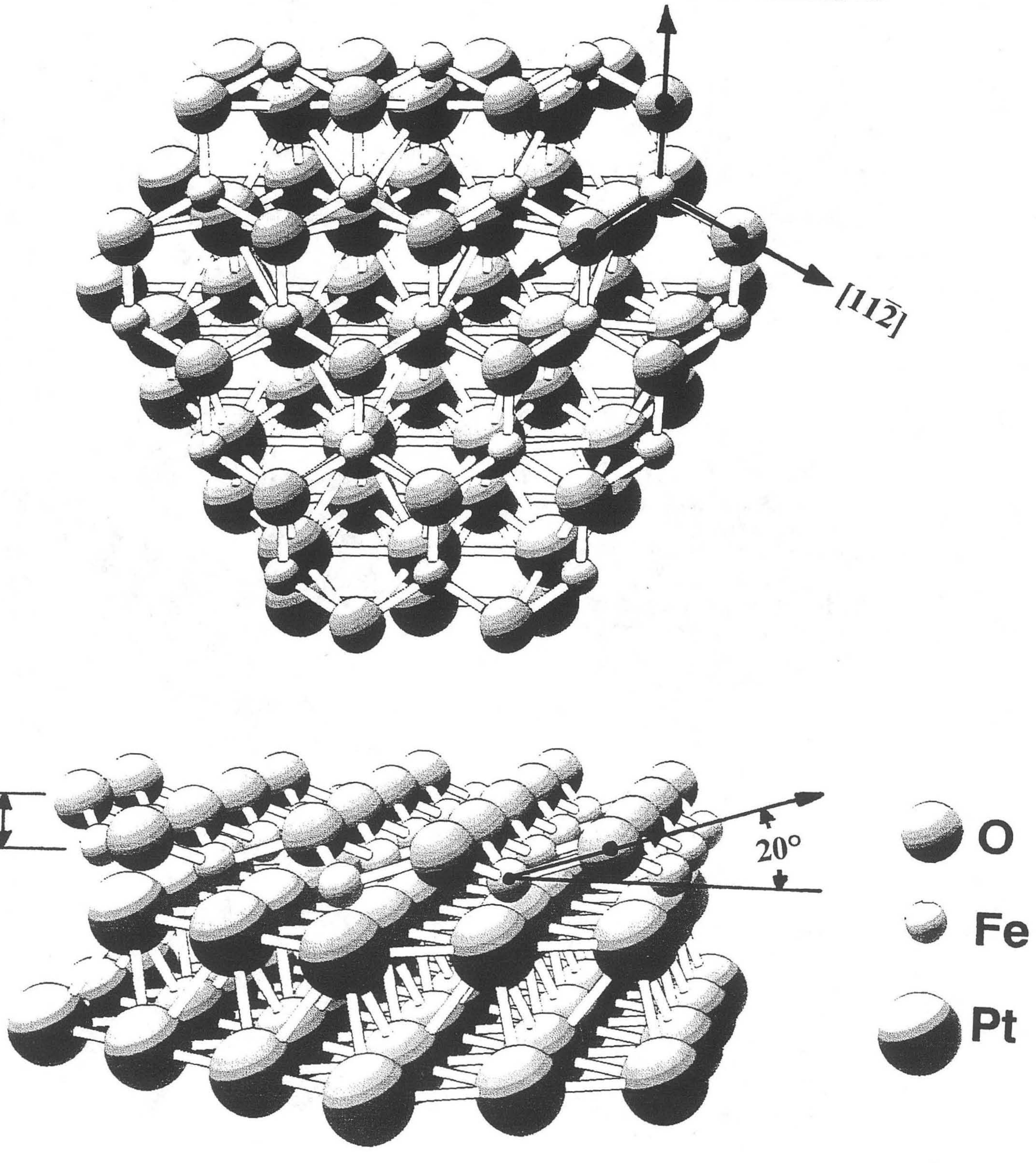

Figure 10

XBD9701-00019.TIF

(a) Fe Chi -- Expt

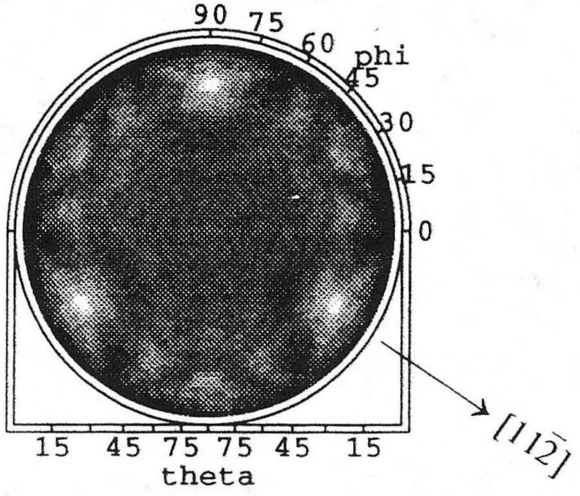

(b) Fe Chi -- Relaxed

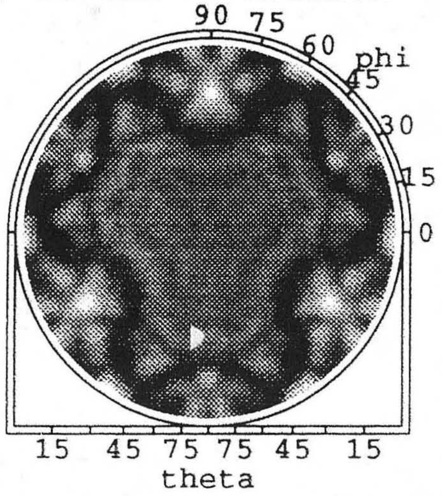

(c) Fe Chi -- Unrelaxed

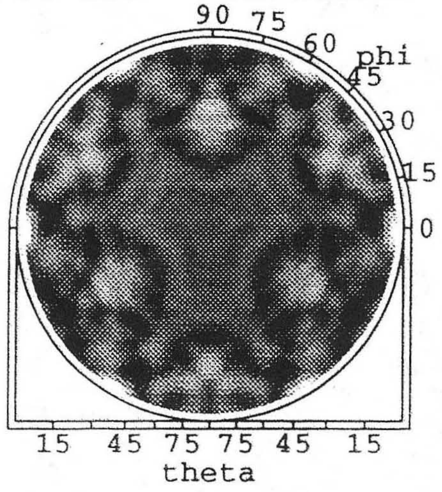

XBD9504-01547.TIF

Figures 11(a)-(c)

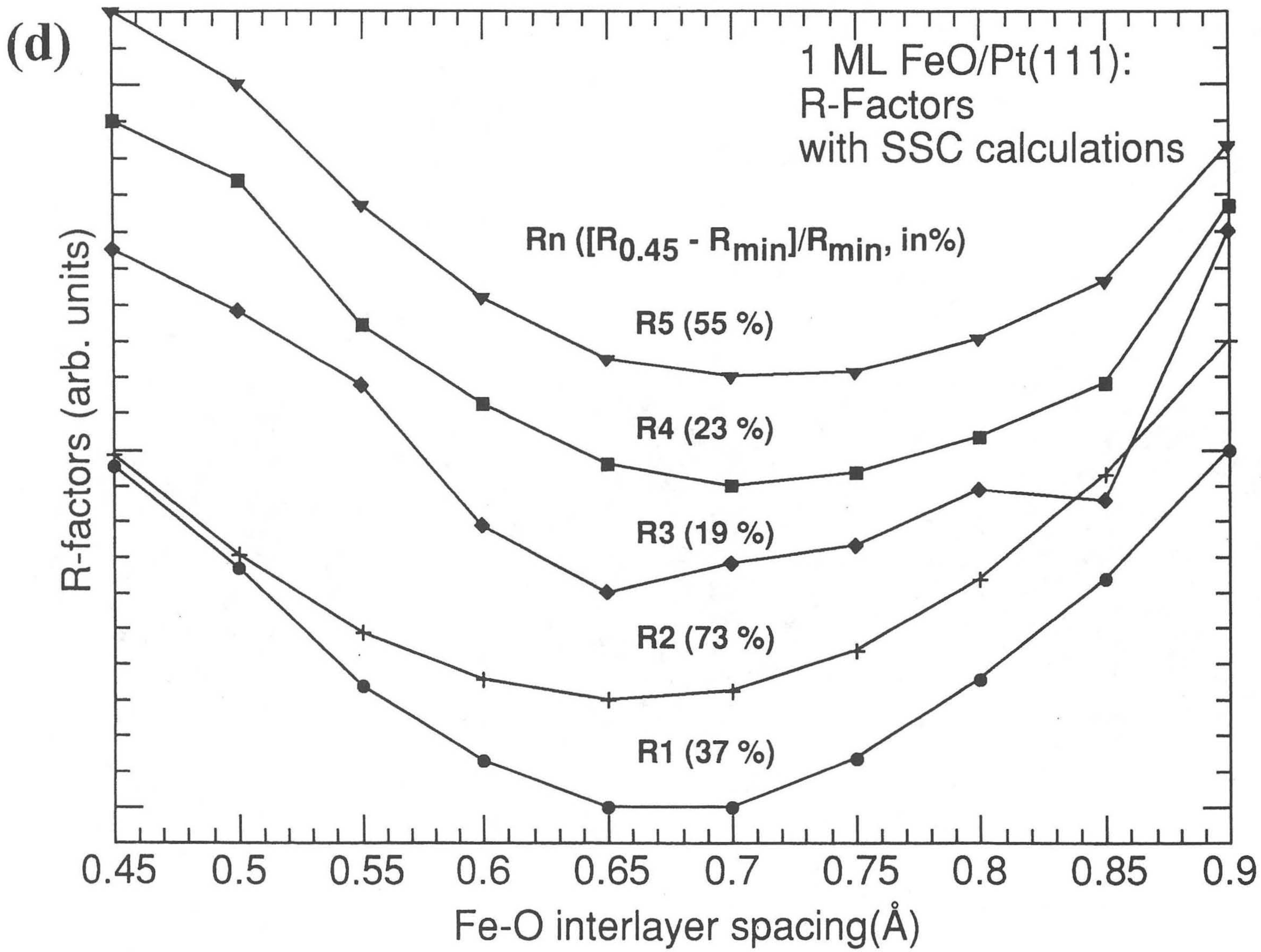

XBD9701-00053.TIF

Figure 11(d)

O Chi -- Expt

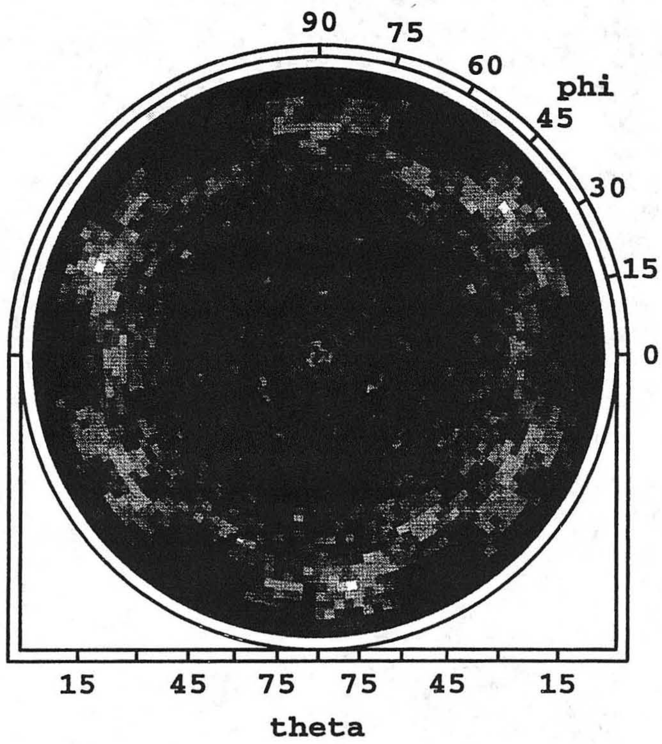

O Chi -- Theory

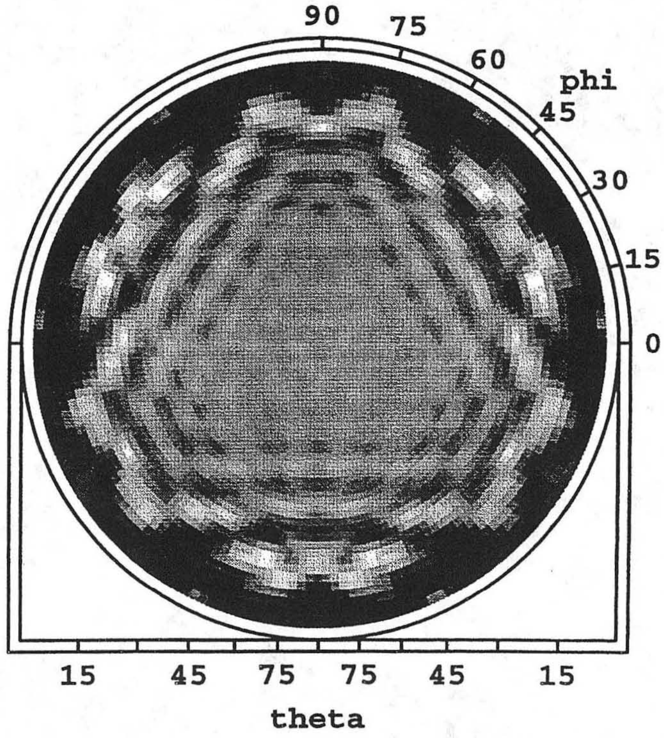

Figure 12

(a) FeO/Pt(111) - Favored

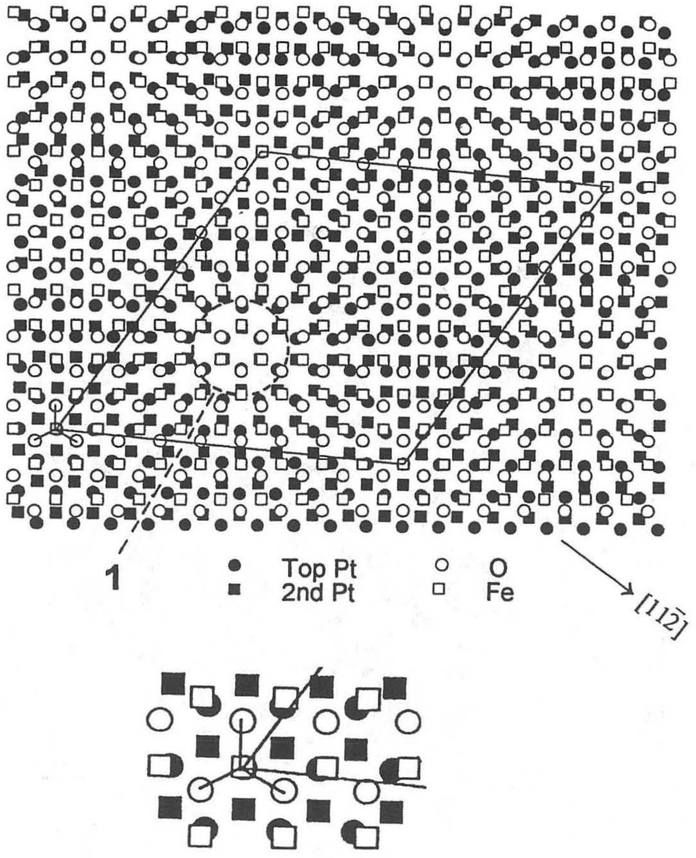

(b) FeO/Pt(111) - Unfavored

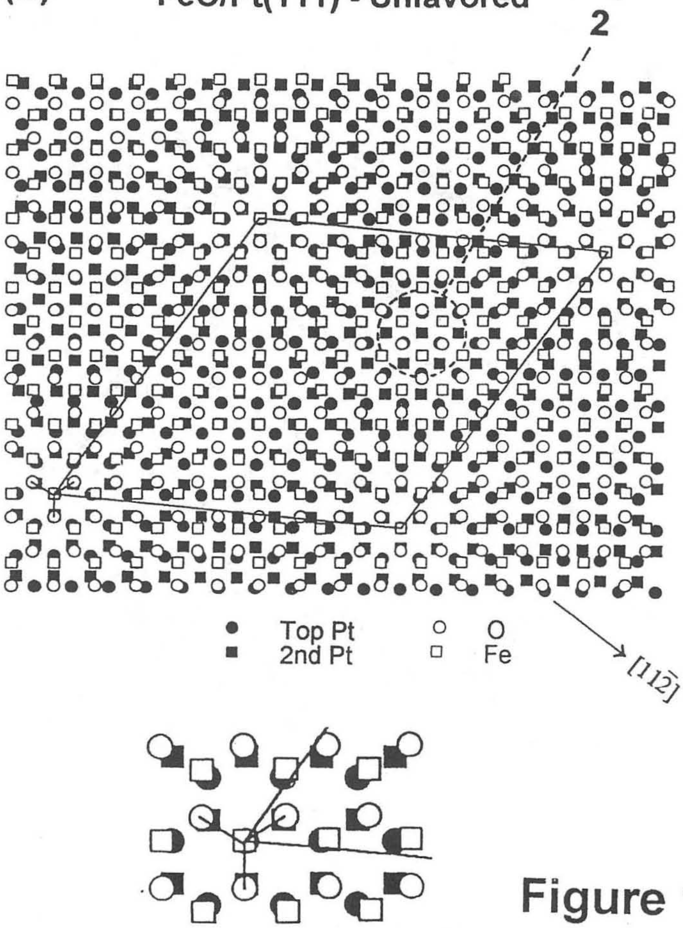

Figure 13

XBD9701-00024.TIF

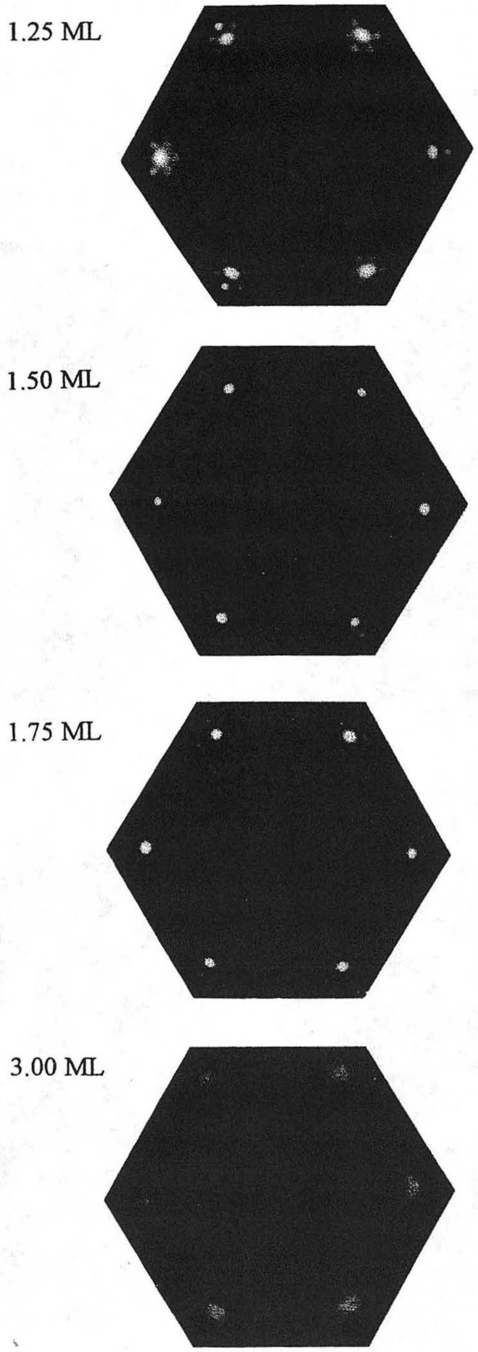

Figure 14

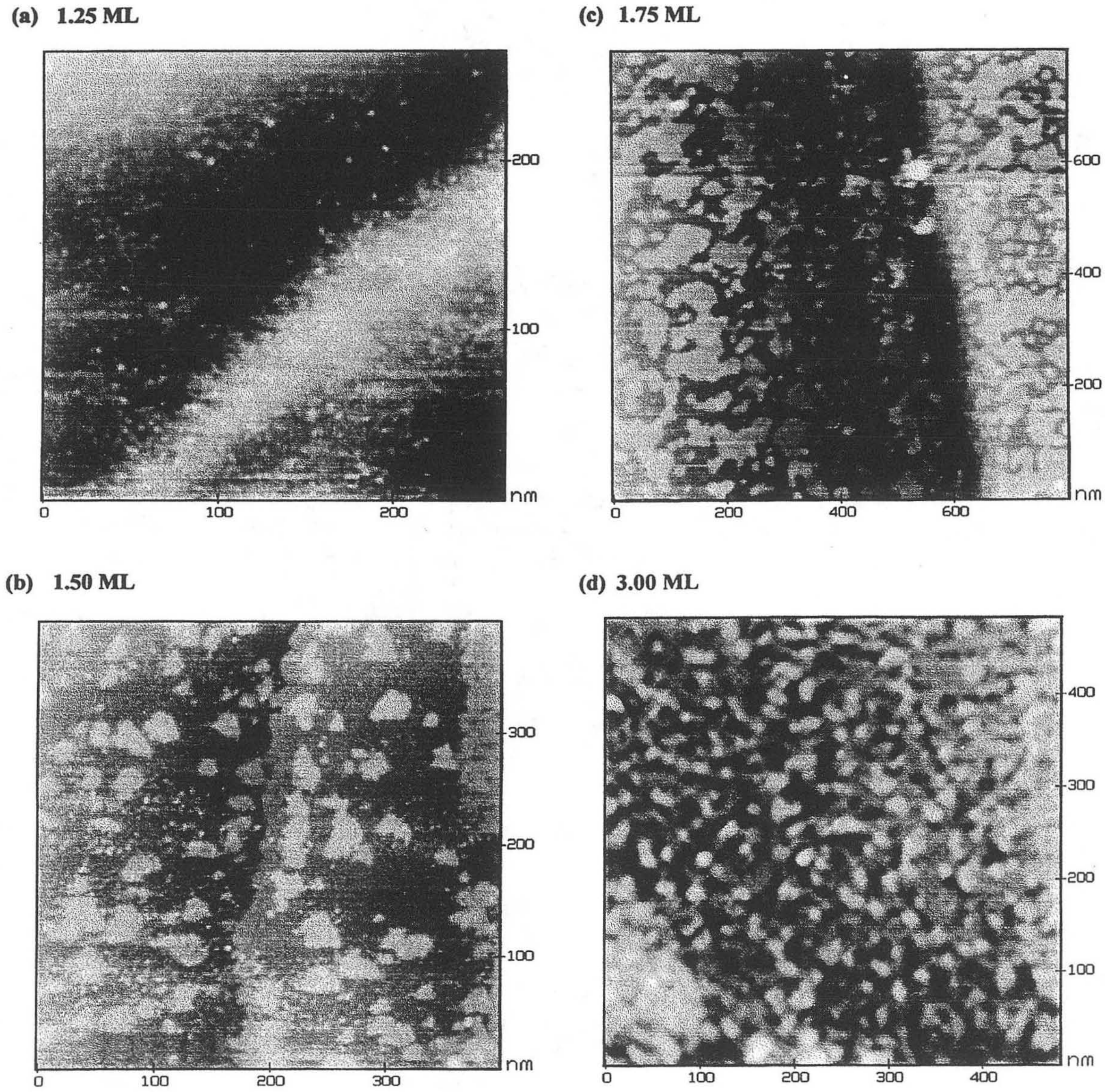
(a) 1.25 ML

(b) 1.50 ML

(c) 1.75 ML

(d) 3.00 ML

Figure 15

1.75 ML

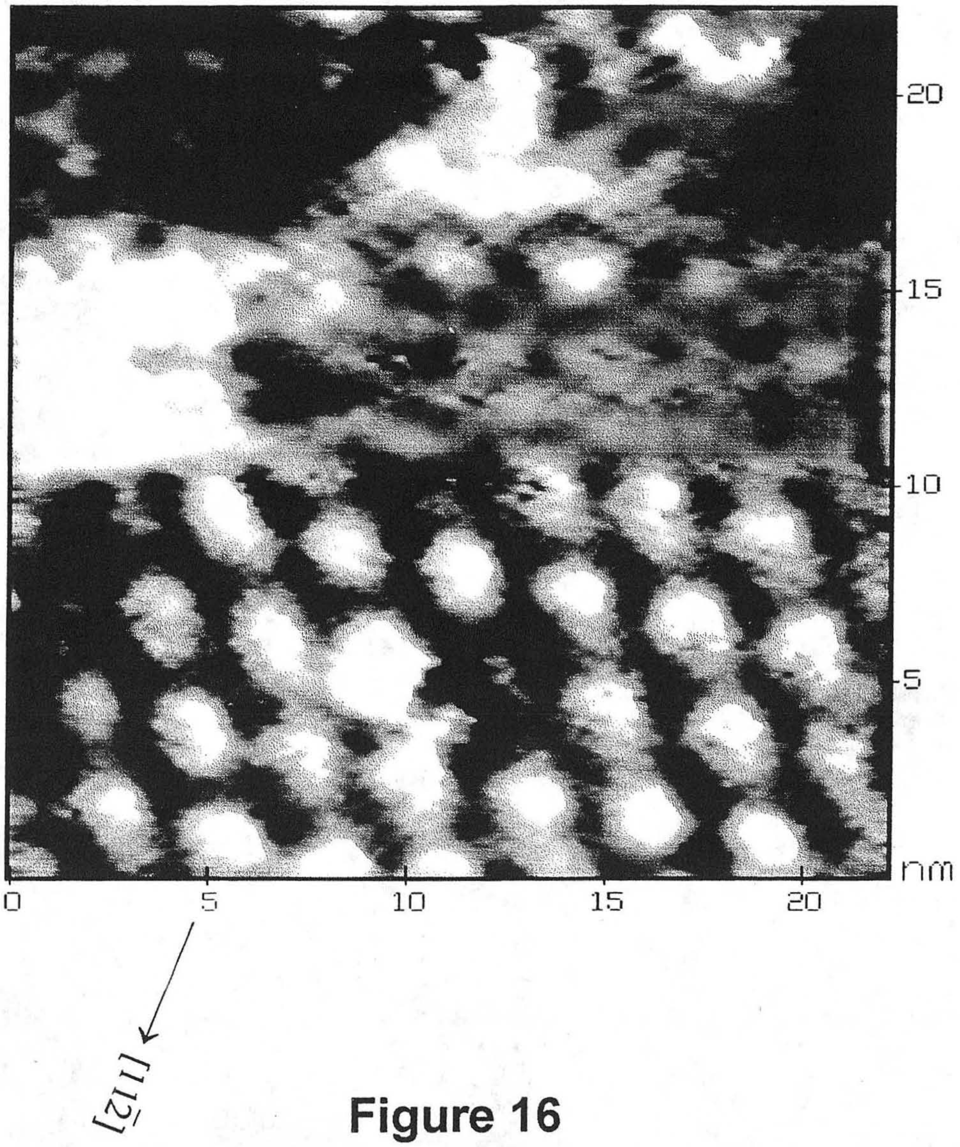

Figure 16

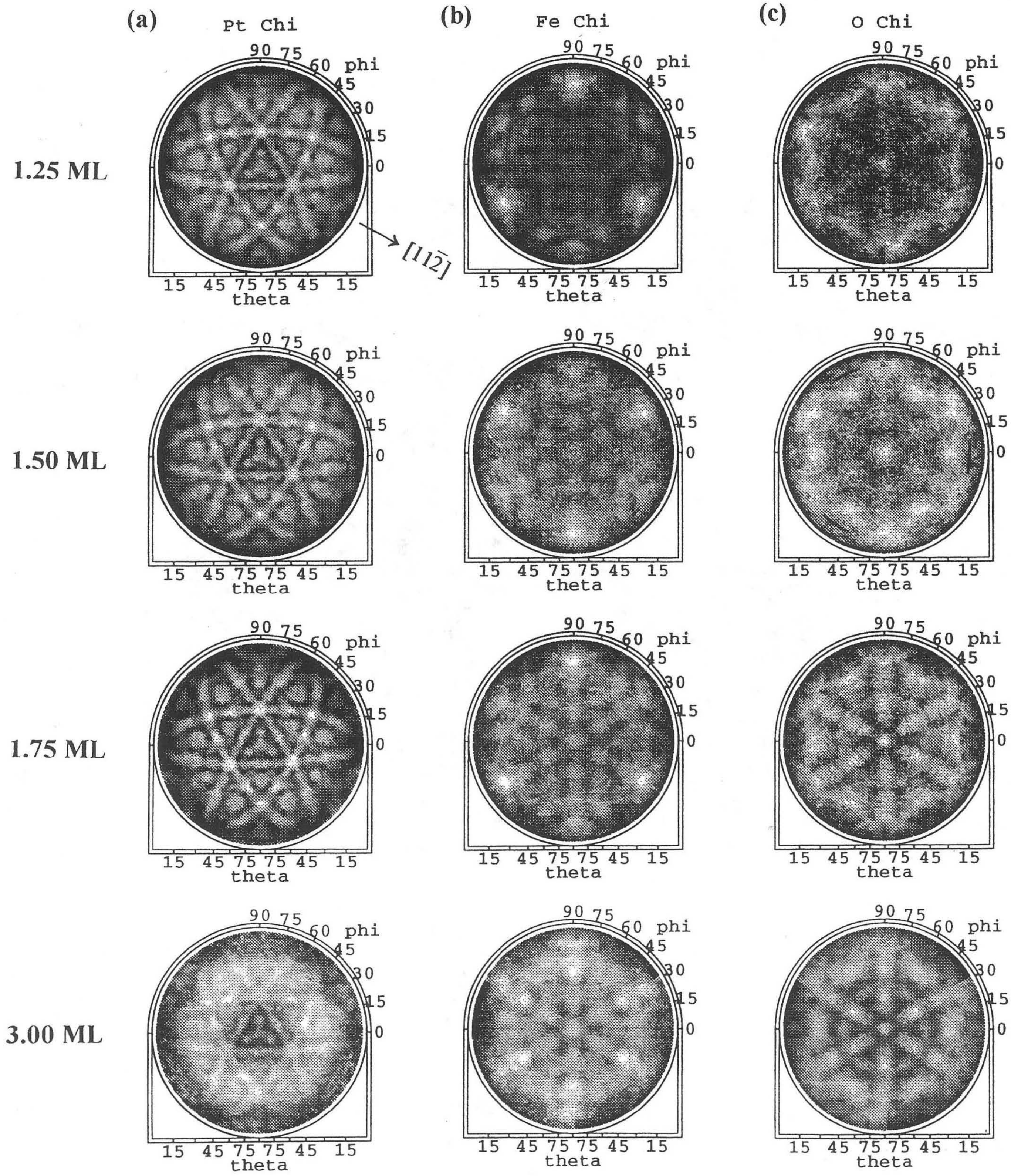
(a)
Pt Chi
(b)
Fe Chi
(c)
O Chi
1.25 ML
1.50 ML
1.75 ML
3.00 ML
90
75
60
phi
45
30
15
0
15 45 75 75 45 15
theta
$[11\bar{2}]$

Figure 17

$Fe_3O_4(111)$

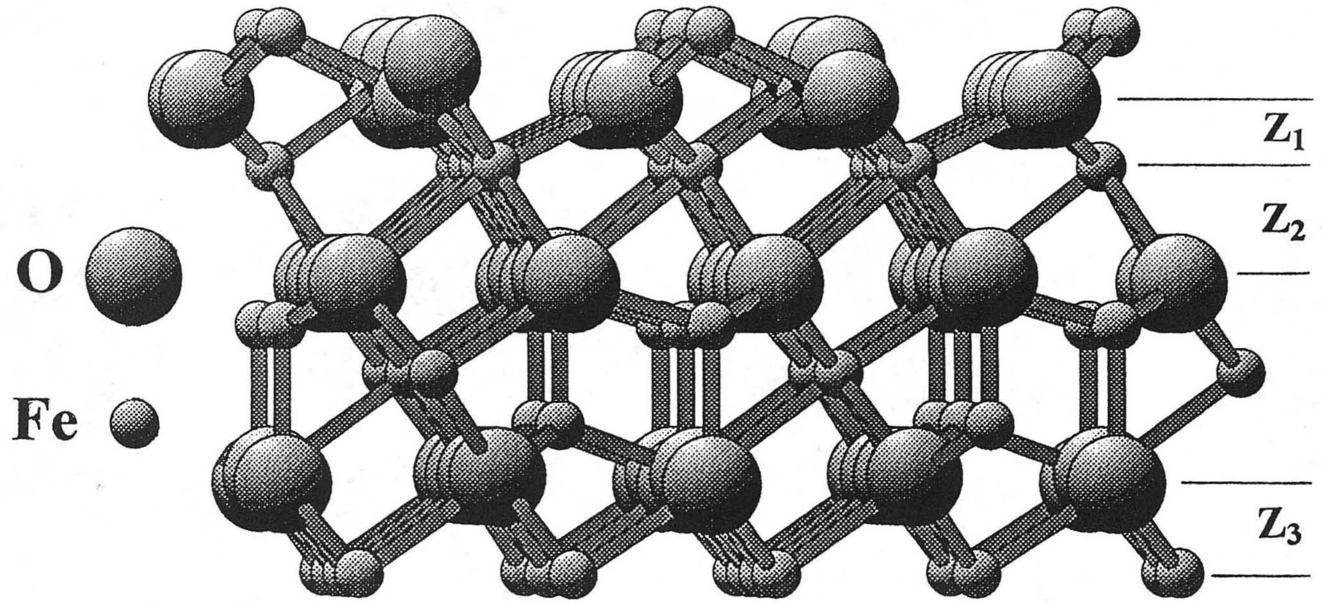

XBD9701-00052.TIF

Figure 18

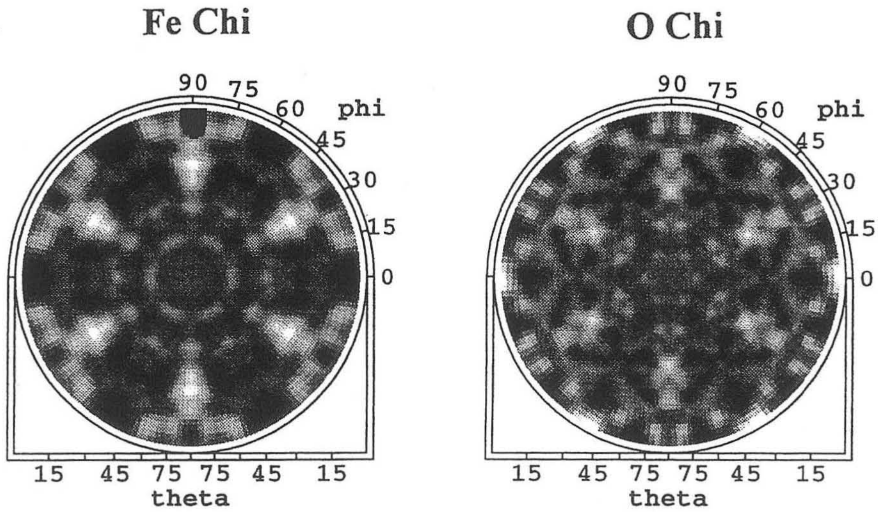

(a) 2 ML FeO(111) -Model 2

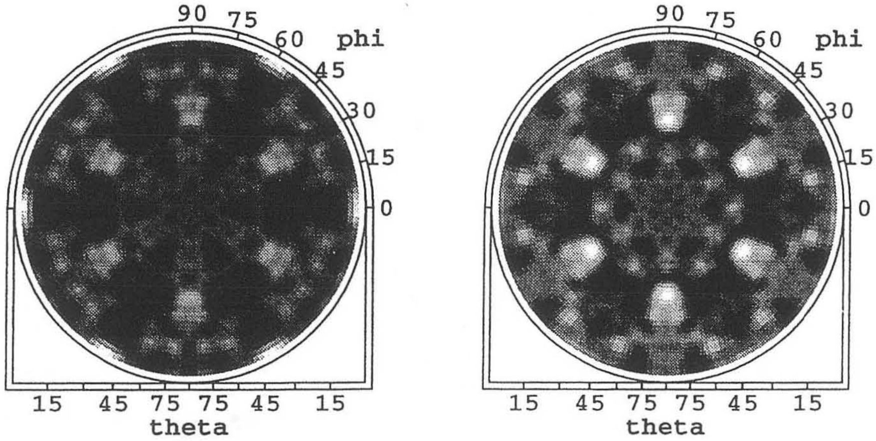

(b) 5 ML FeO(111) -Model 4

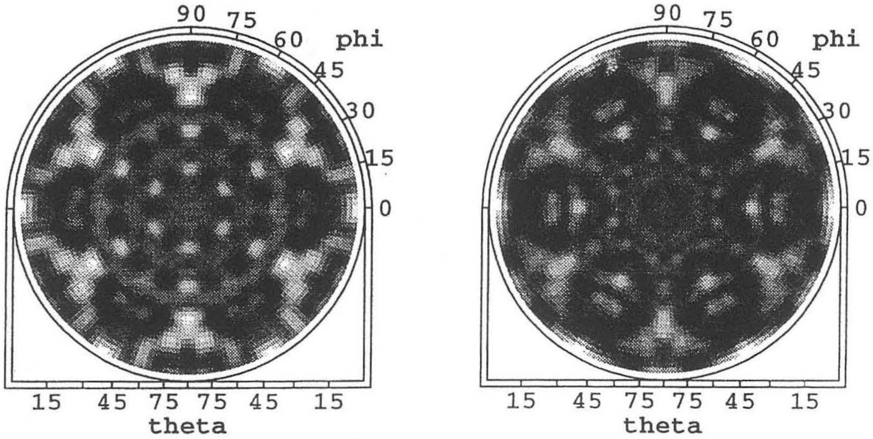

(c) 2 ML Fe_2O_3

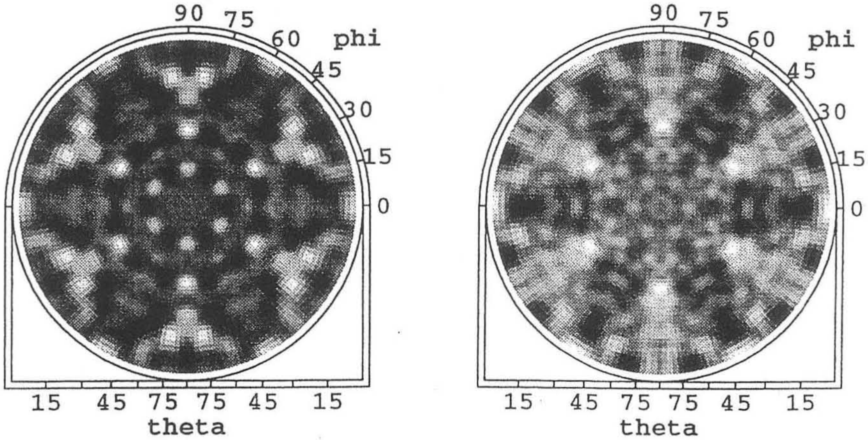

(d) 3 ML Fe_2O_3

Figure 19

(a) Fe_3O_4 - Model 3

(b) Fe_3O_4 - Model 4

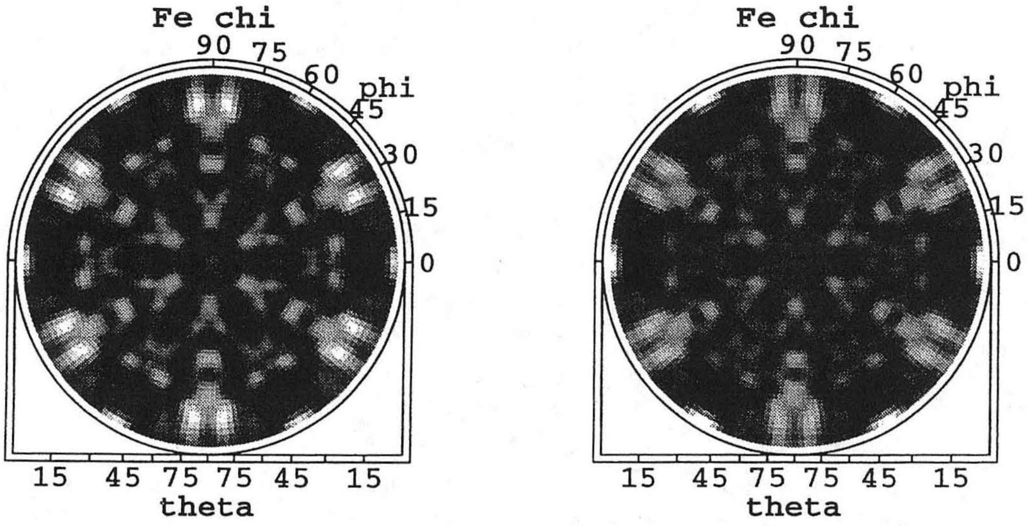

(c) Fe_3O_4 - Model 5

(d) Fe_3O_4 - Model 6

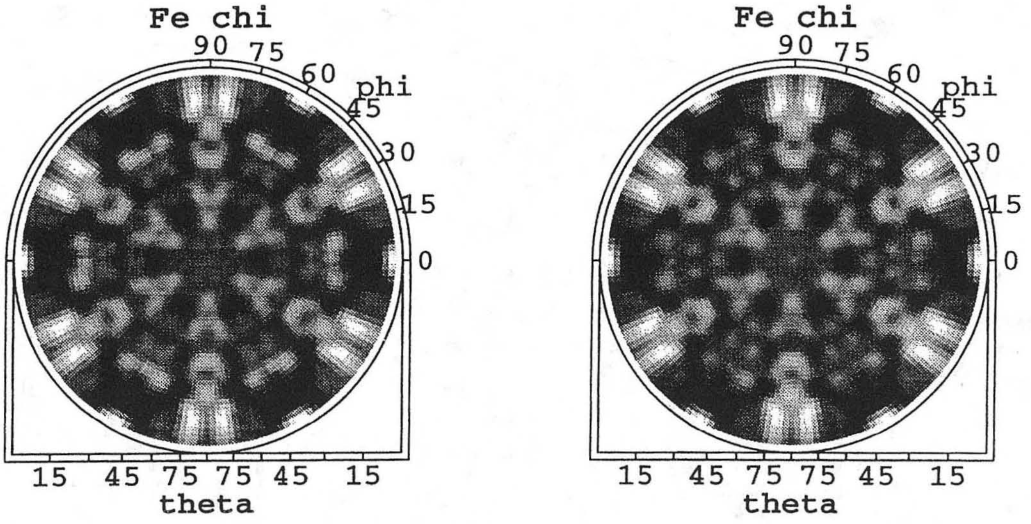

Figure 20

(a) Fe_3O_4 - Model 3

(b) Fe_3O_4 - Model 4

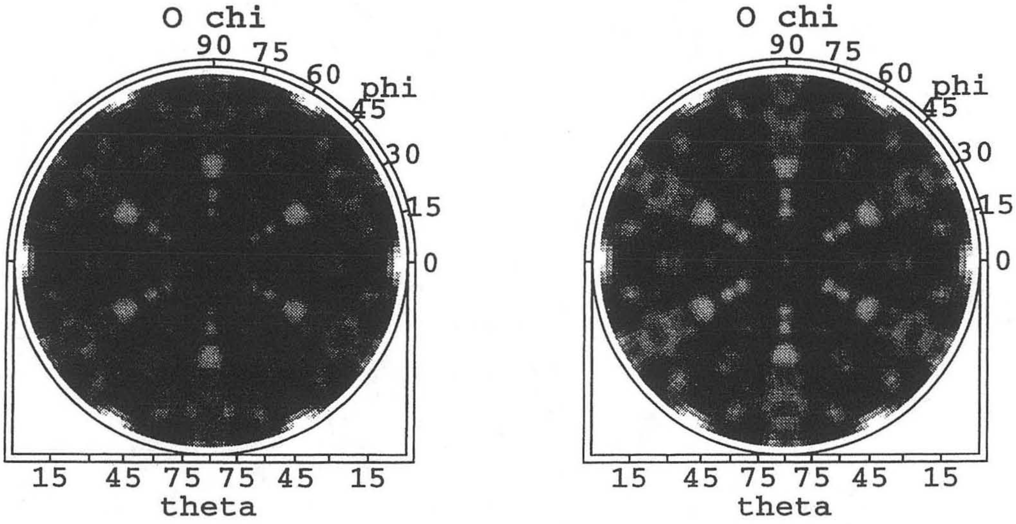

(c) Fe_3O_4 - Model 5

(d) Fe_3O_4 - Model 6

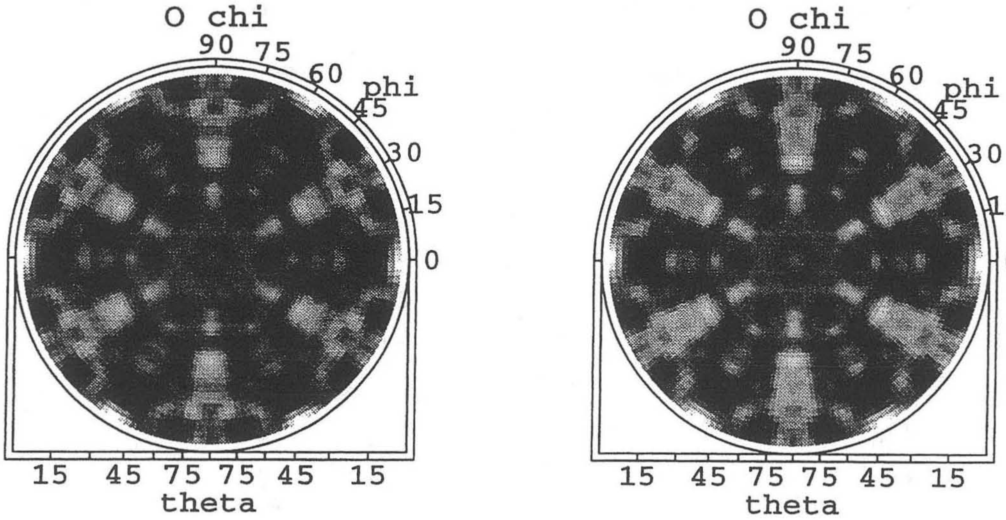

Figure 21

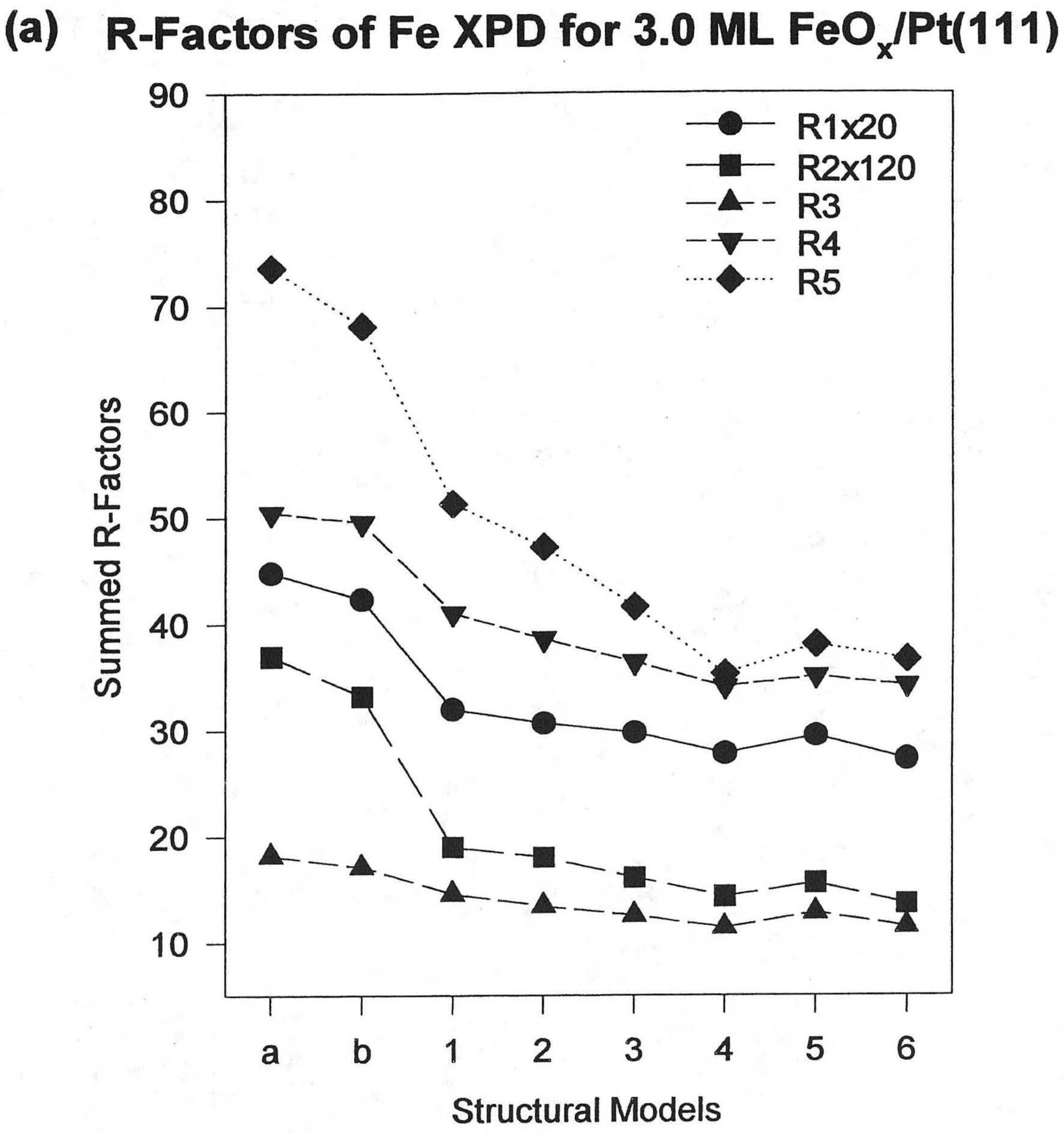

(a) R-Factors of Fe XPD for 3.0 ML $FeO_x/Pt(111)$

a-b Fe_2O_3 with 2 and 3 bilayers, respectively
1-6 Fe_3O_4 with (z_1 , z_2) as given below--
1-2:(1.19, 1.19), 3-4:(0.83, 1.42), 5-6:(0.83, 1.07)
1,3,5: w/ topmost Fe; 2,4,6: w/o topmost Fe

XBD9701-00020.TIF

Figure 22(a)

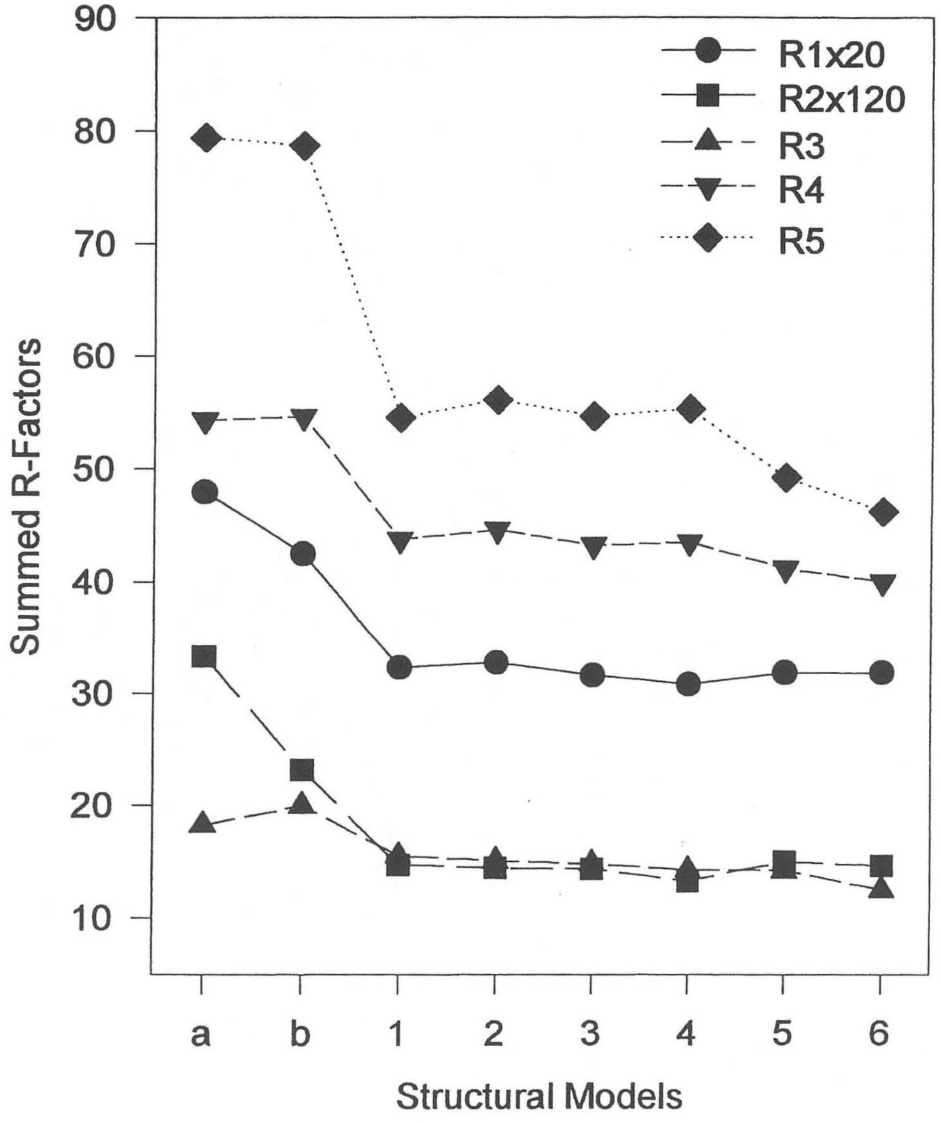

(b) R-Factors of O XPD for 3.0 ML $FeO_x/Pt(111)$

a-b Fe_2O_3 with 2 and 3 bilayers, respectively
1-6 Fe_3O_4 with (z_1 , z_2) as given below- -
1-2:(1.19, 1.19), 3-4:(0.83, 1.42), 5-6:(0.83, 1.07)
1,3,5: w/ topmost Fe; 2,4,6: w/o topmost Fe

XBD9701-00021.TIF

Figure 22(b)

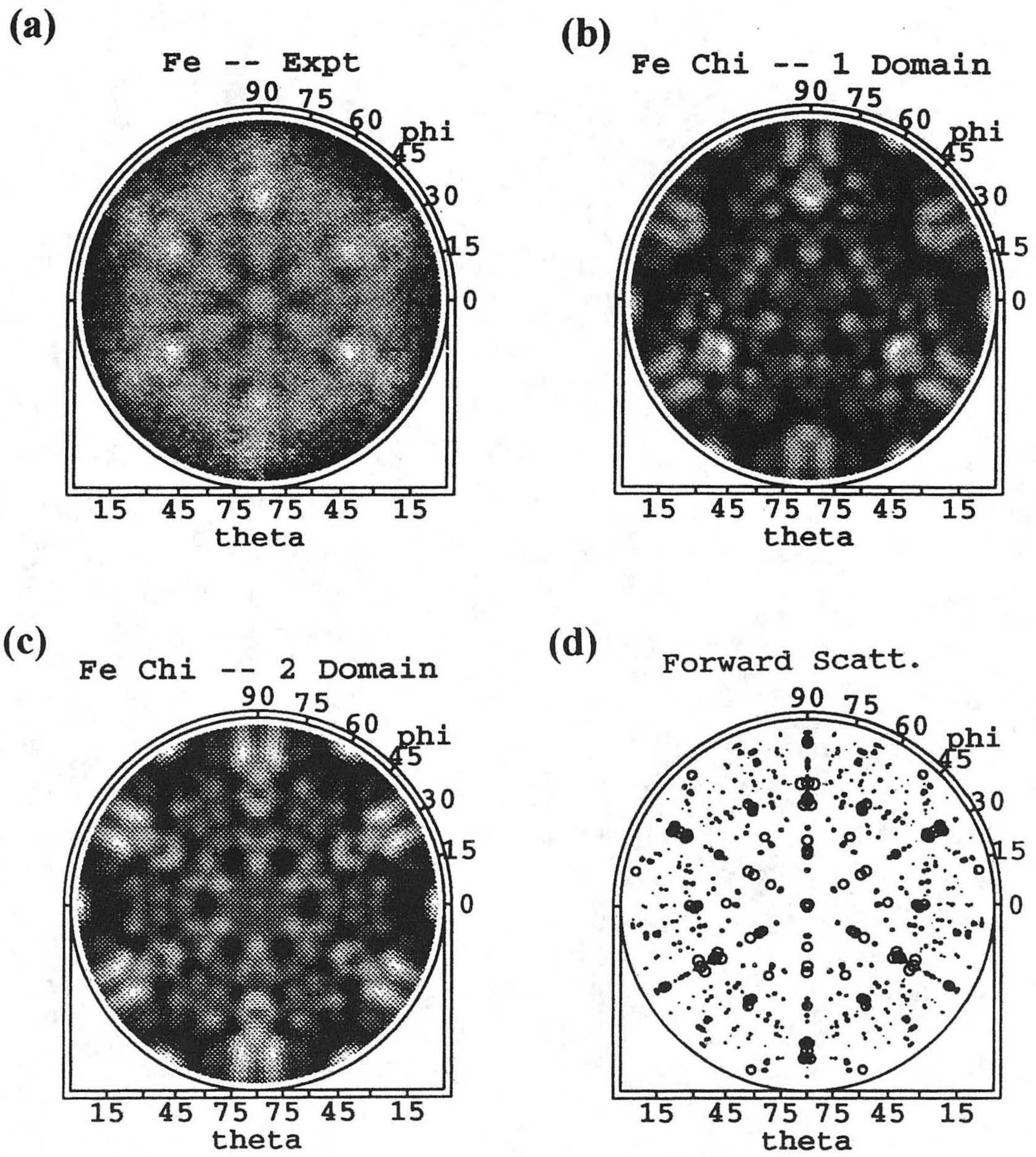
(a)
Fe -- Expt
(b)
Fe Chi -- 1 Domain
(c)
Fe Chi -- 2 Domain
(d)
Forward Scatt.
90
75
60
phi
45
30
15
0
15
45
75
75
45
15
theta

Figure 23

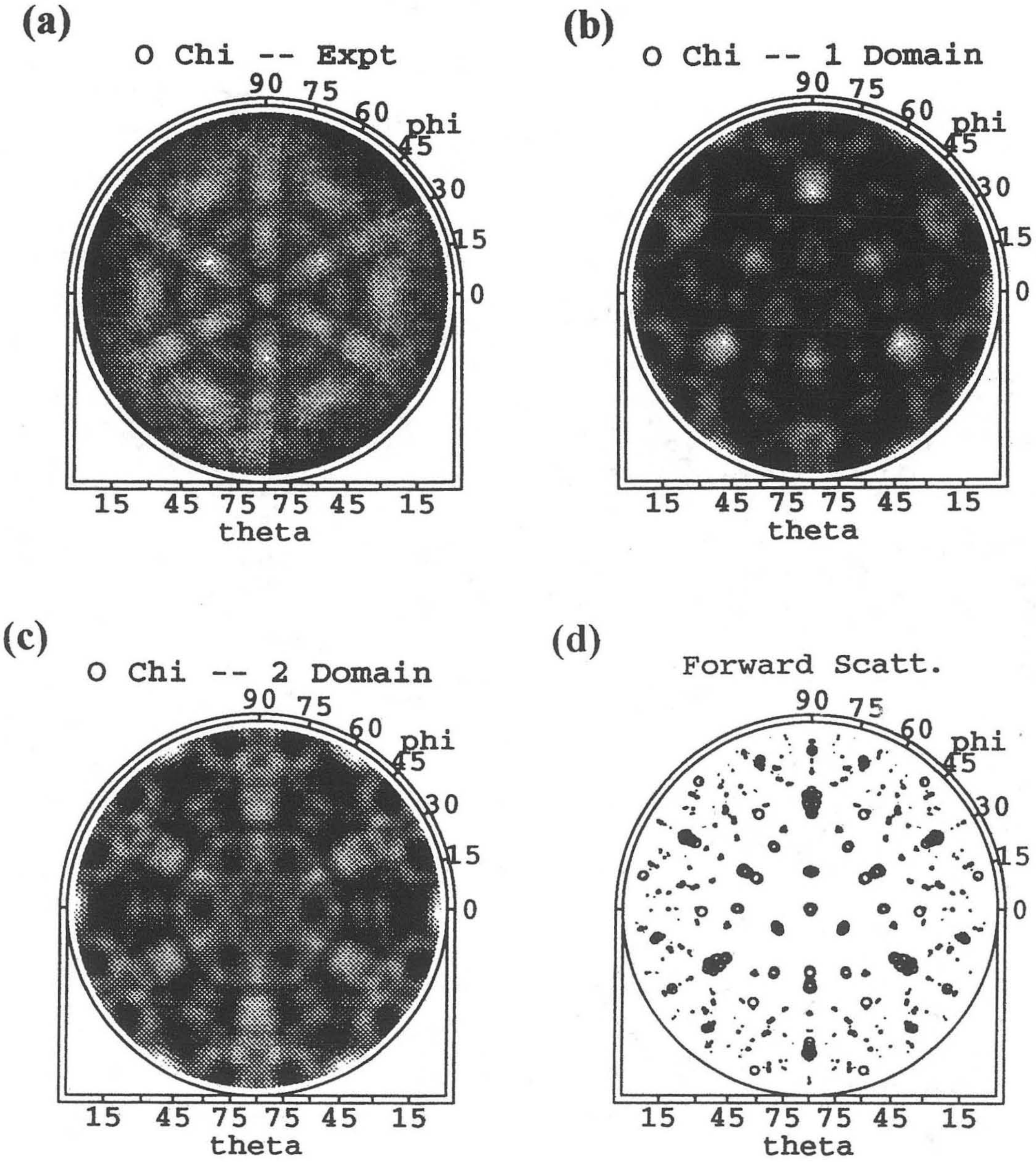
(a)
O Chi -- Expt
(b)
O Chi -- 1 Domain
(c)
O Chi -- 2 Domain
(d)
Forward Scatt.
90 75 60 phi 45 30 15 0
15 45 75 75 45 15
theta

Figure 24

ERNEST ORLANDO LAWRENCE BERKELEY NATIONAL LABORATORY
ONE CYCLOTRON ROAD | BERKELEY, CALIFORNIA 94720

Prepared for the U.S. Department of Energy under Contract No. DE-AC03-76SF00098